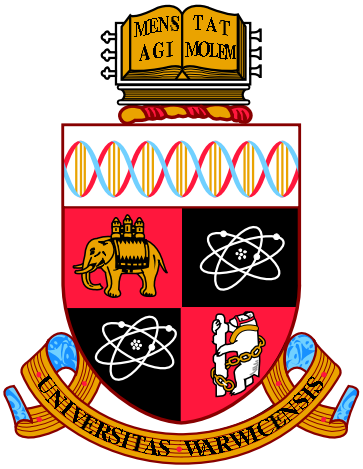

Uniform-momentum zones and coherent structures in Newtonian and non-Newtonian pipe flows

by

Xue Chen

Thesis

Submitted for the degree of

Doctor of Philosophy in Engineering

University of Warwick, School of Engineering

August 2021

THE UNIVERSITY OF
WARWICK

Contents

List of Tables iii

List of Figures iv

Acknowledgments viii

Declarations ix

Abstract x

Nomenclature xii

Chapter 1 Introduction 1

1.1 Motivation . . . 3

1.2 Thesis outline . . . 4

Chapter 2 Background and literature review 6

2.1 Coherent structures in wall turbulence . . . 6

2.1.1 Uniform-momentum zones and internal shear layers . . . 10

2.2 Non-Newtonian pipe flow . . . 16

2.3 Invariants of the velocity-gradient tensors . . . 23

Chapter 3 Methodology 27

3.1 Direct numerical simulation . . . 27

3.2 Vector and tensor transformation . . . 29

3.3 Proper orthogonal decomposition . . . 31

Chapter 4 DNS of turbulent pipe flow 33

4.1 Instantaneous fields of velocity and vorticity . . . 33

4.2 Mean flow statistics . . . 37

4.3 The quiescent core of the pipe . . . 41

4.3.1 Identification of the quiescent core . . . 41
4.3.2 Meandering and intermittency of the core . . . 44
4.3.3 Conditional average properties across the core boundary . . . 45
4.4 Uniform-momentum zones . . . 49
4.4.1 Identification of multiple UMZs . . . 49
4.4.2 The grouping of UMZs . . . 51
4.4.3 The statistical characteristics of UMZ and UMZ interface . . . 52
4.4.4 The vortex clusters on UMZ interfaces . . . 61
4.4.5 The contortion of UMZ interface . . . 64
4.4.6 UMZ interface asymmetry . . . 69
4.4.7 Statistics of UMZs detected from KDE . . . 72
4.5 Internal shear layer . . . 75
4.5.1 Identification of ISL . . . 75
4.5.2 ISL properties as functions of shear strength . . . 79
4.5.3 ISL properties as functions of wall-distance . . . 84
4.5.4 Three-dimensional structural organisation of ISL . . . 87
4.6 Summary . . . 93

Chapter 5 DNS of non-Newtonian turbulent pipe flow 95
5.1 Modelling of shear-thinning fluids . . . 95
5.2 Turbulent statistics and flow structure . . . 96
5.2.1 The mean flow statistics . . . 96
5.2.2 Hairpin vortices in non-Newtonian fluids . . . 106
5.2.3 Streamwise streaks spacing . . . 107
5.3 Topology of non-Newtonian pipe flow . . . 107
5.4 Turbulent spots . . . 115
5.5 Large-scale motions . . . 119
5.6 Summary . . . 123

Chapter 6 Conclusions 124

List of Tables

1.1 DNS studies of turbulent channel and pipe flows 2

2.1 List of studies detected the ISLs directly 13
2.2 List of studies detected the UMZs from PDF of the streamwise velocity 13
2.3 Rheology models for non-Newtonian fluids 17
2.4 Experimental studies of shear-thinning non-Newtonian fluids flow in straight pipes. 21
2.5 DNS studies of non-Newtonian fluids flow in straight pipes. 22

3.1 DNS parameters and spatial resolution of the present turbulent pipe flow at different Reynolds numbers. 29

4.1 Parameters of DNS compared with the present study in the literature for turbulent pipe flow from Re_τ = 180 to 1000. 40
4.2 The grouping of local UMZs by ranges of modal velocities 52
4.3 Estimated wall-normal location of balanced ejection and sweep 86

5.1 DNS parameters of present non-Newtonian pipe flow using the power-law rheology model. 96

List of Figures

2.1 Schematic illustration of Townsend's attached eddy hypothesis 7
2.2 Schematic illustration of organised near-wall vortical structures 8
2.3 Contour of the streamwise velocity and velocity profile showing the uniform-momentum zones in the pipe 10
2.4 Schematic illustration of ISL (UMZ interface) contortion associated to LSMs. 12
2.5 Illustration of (a) PDF-based and (c) ISL-based identification method for UMZs and ISLs. The velocity profile in (b) is the same as in figure 2.3(b). 13
2.6 Relationship between the shear rate and shear stress for different types of time-independent non-Newtonian fluids. 17
2.7 Physical interpretations of the invariants of VGT 25

3.1 Cross-stream view of the computational mesh 30
3.2 $3D$ view of the computational mesh 31

4.1 Contours of the streamwise velocity U and streamwise fluctuation u at Re_τ = 180, 360, 500 and 1000. 34
4.2 Cross-stream contours of the instantaneous streamwise vorticity ω_x at Re_τ = 180, 360, 500 and 1000. 35
4.3 Iso-surfaces of Q at Re_τ = 180, 360, 500 and 1000. 36
4.4 Profiles of mean streamwise velocity $\overline{U}$; root-mean-square velocities u_{rms}, v_{rms} and w_{rms}; and Reynolds shear stress $-\overline{uv}$. 38
4.5 Identification of the quiescent core in the pipe using the *double-PDF* method 42
4.6 The quiescent core in $3D$ 43
4.7 Elimination of the islands outside the main core region 43
4.8 The quiescent core intermittency, γ as a function of the wall-distance 45
4.9 Illustration of conditional averaging around a contorted interface . . . 46

4.10 Coordinates transformation from $x-y$ axes to non-orthogonal $\chi-\xi$ axes . . . 46
4.11 Coordinates transformation from $x-y$ axes to orthogonal $\chi-\xi$ axes . 47
4.12 Conditional averaged U and Ω_θ across the quiescent core interface as functions of the distance from the interface, ξ . . . 47
4.13 Identification of the quiescent core in the pipe using the constrained PDF method . . . 50
4.14 PDF of the number of UMZs in the pipe . . . 51
4.15 PDF of the number of UMZs categorised in each modal velocity group 52
4.16 $3D$ UMZ interfaces at different wall-normal locations . . . 53
4.17 Average wall-normal location of the UMZ in each modal velocity group 53
4.18 Profiles of zonal average U and u^2 for UMZs in different modal velocity groups . . . 55
4.19 Conditional average U, u^2, ΔU, and UMZ interface thickness δ_ω across the interface . . . 57
4.20 Conditionally averaged azimuthal vorticity Ω_θ across the UMZ interface 59
4.21 The UMZ interface-azimuthal vortex attachment on a $x-y$ plane . . 60
4.22 Evolution of the UMZ interface-azimuthal vortex attachment in a streamwise moving frame . . . 60
4.23 The UMZ interface-azimuthal vortex attachment on a $r-\theta$ plane . . . 62
4.24 UMZ interfaces at different wall-normal location, coloured by ω_θ on the interface . . . 63
4.25 PDF of Ω_θ on the UMZ interface . . . 63
4.26 Conditionally averaged prograde vorticity and retrograde vorticity as functions of the distance from the UMZ interface . . . 64
4.27 $3D$ UMZ interface coloured by radial elevation with $2D$ projections on the $x-y$ and $r-\theta$ planes . . . 65
4.28 Illustration of the definition of UMZ interface tortuosity . . . 66
4.29 Tortuosity of the UMZ interface contortion in $2D$ and $3D$ . . . 68
4.30 Illustration of measuring the UMZ interface contortion level in $3D$ . . 68
4.31 $3D$ UMZ interfaces at different wall-distance and interface wall-normal location fluctuation y'_κ . . . 70
4.32 The skewness ζ and kurtosis $\mathcal{K}$ of $3D$ UMZ interfaces . . . 71
4.33 A schematic drawing of the reversed structure of ejections and sweeps 72
4.34 Statistical results of UMZs detected from using the KDE method. . . 74
4.35 Profiles of U and $\partial u/\partial y$ at equally spaced streamwise locations at $Re_\tau = 1000$ . . . 76

4.36 Profiles of $\partial u/\partial y$ at $Re_\tau = 180$, 360, 500 and 1000 with the definition of the shear strength $\mathcal{U}_y$ and ISL location y_κ . . . 77
4.37 ISL filament in a $r-\theta$ plane on the contour of $\partial u/\partial y$ at $Re_\tau = 180$ . . 78
4.38 The average number of ISLs with fitting function . . . 78
4.39 Group averaged properties of the ISLs grouped by their shear strength 80
4.40 Zonal mean velocity profiles of U on each side of the ISLs grouped by their shear strength . . . 81
4.41 Conditional averaged velocity profiles as functions of the distance from the ISLs grouped by their shear strength . . . 83
4.42 Group averaged properties of the ISLs grouped by their wall-normal locations . . . 85
4.43 Iso-surfaces and contours of u, v, ω_x and ω_θ in the $3D$ conditional average field around the positive ISLs at $Re_\tau = 180$ . . . 88
4.44 Contours of u, v, ω_x and ω_θ in the $3D$ conditional average field around the positive ISLs at $Re_\tau = 1000$ . . . 89
4.45 Iso-surfaces and contours of u, v, ω_x and ω_θ in the $3D$ conditional average field around the negative ISLs . . . 90
4.46 Schematic drawing of the cross-stream structure organisation around a positive and a negative internal shear layer. . . . 91
4.47 The average thickness of ISLs estimated from the width of the $\partial u/\partial y$ peaks. . . . 91

5.1 DNS iteration procedure for non-Newtonian fluids . . . 97
5.2 Mean velocity profile $\overline{U}$ for non-Newtonian pipe flow . . . 97
5.3 Profiles of root-mean-square velocities and Reynolds shear stress . . . 98
5.4 Joint PDF of u and v for quadrant analysis of $Q2$ and $Q4$ events . . . 98
5.5 Wall-parallel contours of the streamwise fluctuation u . . . 100
5.6 Wall-parallel contours of the wall-normal fluctuation v . . . 101
5.7 Wall-parallel contours of the azimuthal fluctuation w . . . 102
5.8 Cross-stream contours of U and Q for non-Newtonian case $n = 0.5$ . . 104
5.9 Iso-surfaces of Q . . . 105
5.10 Spanwise two-point correlation of u for streak spacing . . . 108
5.11 Profiles of mean Q_ω . . . 108
5.12 Joint PDFs of invariants $Q-R$ . . . 109
5.13 Joint PDFs of invariants $Q_\omega - Q_s$ . . . 112
5.14 Joint PDFs of invariants of strain-rate tensor, $Q_s - R_s$ . . . 113
5.15 Joint PDFs of invariants of rotation tensor, $Q_\omega - R_\omega$ . . . 114

5.16 Contours of wall-normal fluctuation v: turbulent spots extraction . . . 116
5.17 Volume fraction of turbulent spots in the pipe . . . 117
5.18 Joint PDFs of $Q - R$ in the turbulent spots . . . 118
5.19 Iso-surface of w in the $3D$ conditional averaged field . . . 119
5.20 Contours of w in the conditional averaged field around the turbulent spots . . . 120
5.21 Relative energy content of POD modes . . . 121
5.22 POD mode ϕ_1 of the azimuthal velocity w . . . 122
5.23 Reconstructed field of the azimuthal velocity w using POD modes . . . 122

Acknowledgments

My sincere gratitude goes to my supervisors, Dr. Yongmann Chung and Prof. Minping Wan, who continuously guided me with patience, and inspired me with wisdom. They supported me with encouragement and enthusiasm, and were always there to guide me through obstructions and doubts during my research. I am grateful for their invaluable advice on my research, career, and life. I greatly appreciate the support from my colleagues, I would not have achieved many things without their help. A special mention to Dr. Zhixin Wang for his kind help at the beginning of my research.

A special acknowledgement goes to Mrs. Kemp and Dr. Oliver Buxton who inspired and encouraged me into the world of physics and turbulence. They taught me with enthusiasm and I would not have begun this journey without seeing their stimulating passions in the field.

I am deeply grateful to my parents, Yaojun Chen and Yan Wang who have been unconditionally supporting me for my education and through life; to my grandparents and Huhu who have given me great mental strength. Many thanks to my friends who endured this journey with me. Heartfelt thanks to Dr. Huang for his unfailing support and cheerful companionship.

I am grateful to Southern University of Science and Technology China (SUSTech) for the generous scholarship of the joint PhD programme between SUSTech and the University of Warwick. I would like to thank the UK national high performance computing service, ARCHER via the UK Turbulence Consortium, and the center for computational science and engineering of SUSTech for the access of HPC facilities.

Declarations

This thesis is a presentation of my original research work. The work has not been submitted for any other degree or professional qualification. Appropriate credit has been given within this thesis where reference has been made to the work of others. The work presented has been previously published in the following journals and conferences:

X. Chen, Y. M. Chung, and M. Wan. The quiescent core of turbulent pipe flow. In *UK Turbulence Consortium*, 2018

X. Chen, Y. M. Chung, and M. Wan. Uniform momentum zones in a turbulent pipe flow. In *UK Turbulence Consortium*, 2019a

X. Chen, Y. M. Chung, and M. Wan. The quiescent core of turbulent pipe flow. In *Proceedings of the Eleventh International Symposium on Turbulent and Shear Flow Phenomena*, 2019b. URL "http://www.tsfp-conference.org/proceedings/2019/127.pdf"

X. Chen, Y. M. Chung, and M. Wan. Uniform-momentum zones in a turbulent pipe flow. *Journal of Fluid Mechanics*, 884:A25, 2020

X. Chen, Y. M. Chung, and M. Wan. The uniform-momentum zones and internal shear layers in turbulent pipe flows at Reynolds numbers up to $Re_\tau = 1000$. *International Journal of Heat and Fluid Flow*, 90:108817, 2021

Abstract

The coherent structures in turbulent pipe flows of Newtonian and non-Newtonian fluids are investigated using direct numerical simulation data for the coherent structure organisation, statistical characteristics, evolution and interplay.

The uniform-momentum zones (UMZ) and UMZ interfaces, namely the internal shear layers (ISL) are investigated. The UMZs are large separate regions travelling at relatively constant streamwise velocities, and are demarcated by the thin high-shear layers clustered with spanwise vortices. The UMZs and ISLs are identified by using four different identification methods, three from the literature and a new method which has no ad-hoc parameters applied for UMZ selection. The UMZs identified from using different methods show qualitatively consistent characteristics. The UMZ characteristics observed in the literature have been successfully captured without the use of ad-hoc parameters. The characteristics and dynamics of the UMZs show similarities to both turbulent boundary layer and channel flows. The hierarchical structural distribution of UMZs matches the hierarchy of multi-scaled eddies in Townsend's attached eddy hypothesis. Conditional average quantities revealed the abrupt jump of the streamwise velocity when passing the UMZ interfaces, accompanied with rapid decrease in turbulent intensity. The velocity jump across the ISLs is more abrupt across ISLs residing closer to the wall. The level of contortion of the ISLs intensifies when moving away from the wall, and is always more tortuous in the azimuthal direction than the streamwise direction. The local imbalance between sweep and ejection events are quantified by the skewness of the wall-normal location fluctuation of the contorted UMZ interfaces. The UMZ interfaces in the near-wall region show asymmetric modulation on ejections over sweeps, i.e., the ejections are predominantly stronger than sweeps near the wall with frequently observed bursting. In the pipe centre, the flow has local predominantly stronger sweeps than ejections. The location of locally balanced ejections and sweeps is found approximately at half of the pipe radius.

The DNS data of shear-thinning non-Newtonian pipe flows are examined with the power-law rheology model using three power-law indices. The flow starts to show regions of local laminarisation as the flow becomes more shear-thinning. In the shear-thinning fluids, the off-axis fluctuations are critically lowered, particularly in the wall-normal direction. At the highest level of shear-thinning examined, the flow is already transitional, showing turbulent spots and large regions of pre-transition laminar fluctuations. These laminar fluctuations are revealed by proper orthogonal

decomposition as very-large-scale cross-flow instabilities. While the off-axis fluctuations are significantly weakened, the root-mean-square streamwise fluctuation is marginally higher than the Newtonian flow due to the streamwise acceleration in the upstream and downstream of the turbulent spots. The vortical structures are much more organised in the shear-thinning fluids compared with the Newtonian flow. The near-wall streaks are wider in the shear-thinning fluids, and the spanwise streak spacing increases as the flow becomes more shear-thinning. The fine-scale flow topology is interpreted from the joint PDFs of the velocity-gradient tensor invariants. The universal 'tear drop' shape of the $Q-R$ distribution is obtained in the most inhomogeneous shear-thinning fluid, even in the pseudo-laminar regions. Hence, the universality of the classical 'tear drop'-shaped $Q-R$ distribution is not limited to fully-developed inhomogeneous turbulence.

Nomenclature

The notation used in this thesis is presented in the following order: Greek, Roman, symbols, and abbreviations, each alphabetically ordered.

Greek

γ intermittency factor

$\dot{\gamma}$ shear rate, $\dot{\gamma} = \sqrt{2S_{ij}S_{ij}}$

δ boundary layer thickness, half-height of channel ($\delta = h$) and radius of pipe ($\delta = R$)

δ_ω UMZ interface thickness

Δ change in variable, e.g., grid spacing Δx_i, change in velocity magnitude ΔU

∇ vector differential operator, $\nabla = \frac{\partial}{\partial x}\mathbf{i} + \frac{\partial}{\partial y}\mathbf{j} + \frac{\partial}{\partial z}\mathbf{k}$

∇^2 Laplacian operator, $\nabla^2 = \nabla \cdot \nabla = \frac{\partial^2}{\partial x^2} + \frac{\partial^2}{\partial y^2} + \frac{\partial^2}{\partial z^2}$

ε energy dissipation

ζ skewness

θ azimuthal/spanwise direction of the cylindrical coordinates

λ_θ Streak spacing in the $\theta-$direction

μ dynamic viscosity

μ_w mean wall viscosity

μ_0 viscosity at zero shear rate

μ_∞ viscosity at infinite shear rate

ν kinematic viscosity, $\nu = \mu/\rho$

ξ distance to shear layer

ρ fluid density

σ standard deviation

τ shear stress

τ_w wall shear stress

τ_y yield stress

$\boldsymbol{\tau}$, τ_{ij} viscous stress tensor

Φ POD modes

χ tangential direction along contorted UMZ interface

Ω_{ij} rate-of-rotation tensor, $\Omega_{ij} = \frac{1}{2}(\nabla \mathbf{U} - \nabla \mathbf{U}^T)$

ω vorticity, $\omega = \nabla \times \mathbf{U}$

Roman

A_{ij} velocity-gradient tensor, $A_{ij} = \partial U_i / \partial x_j$

$\mathcal{B}$ histogram bin width

D pipe diameter

$\frac{dp}{dx}$ axial pressure gradient

$\mathbf{f}$ external body force

h channel half height, bandwidth of KDE functions

K fluid consistency coefficient

$\mathcal{K}$ kurtosis

L_x pipe length, streamwise length of the computational domain

$\mathcal{L}_x$ streamwise window size

l_x length of 2-D interface on streamwise-wall-normal $(x-y)$ planes

l_θ length of 2-D interface on cross-stream $(r-\theta)$ planes

M_i UMZ groups based on modal velocity U_m

N sampling size

N_κ number of ISL

N_{UMZ} number of UMZ

n flow index/power-law index

p pressure

Q the second invariants of the velocity-gradient tensor

R pipe radius, or the third invariant of velocity-gradient tensor

Re Reynolds number based on the pipe radius, $Re = \rho U_b R/\mu = U_b R/\nu$

Re_D Reynolds number based on the pipe diameter, $Re_D = \rho U_b D/\mu = U_b D/\nu$

Re_τ Reynolds number based on friction velocity, $Re_\tau = u_\tau \delta/\nu$

Re_g generalised Reynolds number of non-Newtonian fluids, $Re_g = \rho U_b D/\mu_w$

Re_{cr} critical Reynolds number for turbulence transition

R^s ISL groups based on the ISL shear strength $\partial u/\partial y$

R^y ISL groups based on the ISL wall-normal location y_κ

r, θ, x radial, azimuthal and axial directions in the cylindrical coordinates

r_κ radial location of ISL, $r_\kappa = 1 - y_\kappa$

S_{ij} rate-of-strain tensor, $S_{ij} = \frac{1}{2}(\nabla \mathbf{U} + \nabla \mathbf{U}^T) = \frac{1}{2}(\partial U_i/\partial x_j + \partial U_j/\partial x_i)$

S_κ surface area of an interface

t time

$\mathbf{U}(\mathbf{x}, t)$ Eulerian velocity

$\mathbf{u}(\mathbf{x}, t)$ velocity fluctuations

$\mathbf{u}_{rms}$ root-mean-square velocity fluctuations

U, U_x, U_y velocity in the axial (streamwise), horizontal and vertical directions of the Cartesian coordinates

U, V_r, W streamwise, radial and azimuthal velocity in the axial, radial and azimuthal directions of the cylindrical coordinates

U_{CL} centreline velocity of channel and pipe

U_b a constant bulk mean velocity in channel and pipe

$\overline{U}$ mean streamwise velocity in the wall-normal direction

U^+ streamwise velocity in wall units, $U^+ = U/u_\tau$

U_m UMZ modal velocity at the peaks on the PDF of U

U_z the average streamwise velocity in a UMZ

U_κ threshold velocity of UMZ interface and ISL

$\mathcal{U}_y$ peaks on the profiles of velocity gradient $\partial u/\partial y$

u, v, w streamwise, wall-normal and azimuthal/spanwise velocity fluctuations

$-\overline{uv}$ Reynolds shear stress

u_τ friction velocity, $u_\tau = \sqrt{\tau_w/\rho}$

V wall-normal velocity, defined positive away from the wall

V_r radial velocity, $V_r = -V$

$\mathcal{V}$ volume of the pipe, $\mathcal{V} = \pi R^2 L_x$

$\mathcal{V}_L$ volume of laminar flow

$\mathcal{V}_T$ volume of turbulent flow

$\mathbf{x}$ location

x_c, y_c, x horizontal, vertical and axial directions in the Cartesian coordinates

$x_\kappa, y_\kappa, \theta_\kappa$ axial, wall-normal and azimuthal location of ISL

x^*, y^*, θ^* axial, wall-normal and azimuthal location of turbulent spots

y wall-normal distance, $y = R - r$

y^+ wall-normal distance y in wall units, $y^+ = yu_\tau/\nu$

y_κ wall-normal location of ISL, $y_\kappa = 1 - r_\kappa$

y'_κ fluctuation of the wall-normal location of ISL, $y'_\kappa = y_\kappa - \langle y_\kappa \rangle$

Abbreviations

CFD computational fluid dynamics

CFL Courant-Friedrichs-Lewy

DNS direct numerical simulation

EMD empirical mode decomposition

FDM finite difference method

FEM finite element method

FVM	finite volume method
GLL	Gauss-Lobatto-Legendre
HPC	high performance computing
ISL	internal shear layer
KDE	kernel density estimation
LES	large-eddy simulation
LSM	large-scale motion
MHD	magneto-hydrodynamics
MPI	message passing interface
PDF	probability density function
PIV	particle image velocimetry
POD	proper orthogonal decomposition
$Q2$	quadrant-two
$Q4$	quadrant-four
RMS	root-mean-square
SEM	spectral element method
SGS	sub-grid-scale
SEM	spectral element method
TNTI	turbulent/non-turbulent interface
UMZ	uniform-momentum zone
VLSM	very-large-scale motions

$2D$ two dimensions, two-dimensional

$3D$ three dimensions, three-dimensional

Chapter 1

Introduction

Turbulence is perhaps the most curious subject in fluid mechanics. Within many different types of turbulent flows (e.g., homogeneous turbulence, magnetohydrodynamic turbulence (MHD), free shear flows, wakes), the topic of wall-bounded turbulent flows is of great interest because of their common appearance in nature and widely-ranged applications in engineering. Fundamental research on wall turbulence has been focused on the Reynolds number dependence, the scaling of the turbulence statistics, the self sustainment of near-wall cycles, the evolution of energy spectra, and the organised coherent motions at various scales. Progress in these areas were reviewed by Cantwell (1981), Robinson (1991), Panton (2001), Klewicki et al. (2010) and Smits et al. (2011).

The development in HPC facilities and numerical methods enabled the direct numerical simulation (DNS) to be a powerful tool in turbulence research (Moin and Mahesh (1998)). The current computational power limits the DNS of wall-bounded flows at friction Reynolds numbers Re_τ below $\mathcal{O}(10^4)$ whereas experiments can achieve up to $\mathcal{O}(10^6)$. However, DNS has advantages in capturing the very-fine-scale physics of the flow by gaining full $3D$ high-resolution data which is difficult to be obtained in experiments. DNS of wall-bounded flows has been performed at increasingly higher Reynolds numbers with advances in computational power. Table 1.1 lists the DNS of turbulent boundary layers (TBL), channel and pipe flows. The highest-Reynolds-number data is available up to $Re_\tau = 5200$ (Lee and Moser (2015)) and 8000 (Yamamoto and Tsuji (2018)) for the channel, and up to $Re_\tau \approx 3000$ for the pipe (Ahn et al. (2015)).

Geometry		Highest Re_τ	L_x/δ
Boundary layer	Spalart (1988)		
	Jiménez et al. (2010)	692	20π
	Schlatter et al. (2009)	900	21π
	Schlatter et al. (2010)	1370	21π
	Lee and Sung (2011)	1000	5π
	Sillero et al. (2013)	2000	21π
Channel	Kim et al. (1987)	180	4π
	Antonia et al. (1992)	300	4π
	Moser et al. (1999)	590	2.8π
	Abe et al. (2001)	640	2π
	Iwamoto et al. (2002)	650	2.5π
	del Álamo and Jiménez (2003)	550	8π
	del Álamo et al. (2004)	934	8π
	Hoyas and Jiménez (2006)	2003	8π
	Bernardini et al. (2014)	4000	6π
	Lozano-Durán and Jiménez (2014)	4200	5π
	Lee and Moser (2015)	5200	10π
	Yamamoto and Tsuji (2018)	8000	16
Pipe	Eggels et al. (1994)	180	10
	Akselvoll and Moin (1996)	180	30
	Loulou et al. (1997)	190	10
	Wagner et al. (2001)	320	10
	Wu and Moin (2008)	1142	15
	Chin et al. (2010)	500	20π
	Wu et al. (2012)	685	30
	Ahn et al. (2013)	934	30
	El Khoury et al. (2013)	1000	25
	Chin et al. (2014)	2003	3π
	Ahn et al. (2015)	3008	30
	Chen et al. (2021)	1000	30

Table 1.1: DNS studies of turbulent channel and pipe flows. L_x indicates the streamwise computational domain in terms of the boundary layer thickness δ. δ is equivalent to the pipe radius R and channel half height h.

1.1 Motivation

Our understanding in wall turbulence fuels the development of turbulence models which greatly relies on accurate characterisation of turbulence structures. The high resolution of DNS enables us to resolve the fine-scale turbulent motions and coherent structures which are crucial for turbulence modelling because they are self-similar and less flow dependent. Self-similar small-scale structures were found in flows including a variety of free shear flows (mixing layers, wakes and jets) and wall-bounded flows (turbulent boundary layers, channels and pipes). The small-scale universality serves as the foundation of many sub-grid-scale (SGS) models. As the smallest scales decrease with increasing Reynolds numbers, these structures are very difficult to obtain in laboratories at very fine scales, and is especially difficult for opaque non-Newtonian fluids. Self-similar coherent structures were observed at varying scales in all types of wall-bounded flows, for instance, the large- and very large-scale motions, superstructures, organised quasi-streamwise vortex loops travelling in packets, and uniform-momentum zones (UMZ) and the internal shear layers (ISL) bounding the zones.

The first part of this work investigates the UMZs in Newtonian fluid flows in the pipe. Since the first report on the existence of the UMZs in a turbulent boundary layer (Meinhart and Adrian (1995)), numerous studies on their structural organisation have been documented in the recent decades. The UMZs are large regions of relatively uniform streamwise velocities in the flow, while most of the velocity changes from the wall to the centreline take place over very thin internal shear layers between the UMZs. The concept of multiple UMZs is similar to the hierarchical distribution of eddies of growing size in the attached eddy model (Townsend (1976); Perry and Chong (1982)). The characteristics of multiple UMZs and their interfaces have been studied only in turbulent boundary layers (de Silva et al. (2016, 2017); Laskari et al. (2018)) and channels (Kwon et al. (2014); Yang et al. (2016)). In the present study, the characteristics of multiple UMZs at multiple Reynolds numbers are investigated. This study first confirms their statistical behaviours found in the channel and TBL in the present pipe flow, and then extend to new unknown characteristics of the UMZ and their interfaces. Different methods and parameters were used in the identification of UMZs, and the identified UMZs are well-known to be sensitive to the user-defined parameters (Fan et al. (2019); Chen et al. (2021)). Therefore, this study aims to compare and validate the UMZ characteristics reported from using different methods. Four identification methods including a new method which requires no ad-hoc filters on the UMZ identification are used to reproduce

qualitatively consistent statistics to studies using varying methods and parameters.

The second part of this work investigates the turbulence structures in non-Newtonian fluid flows in the pipe. Applications of non-Newtonian fluids, particularly in pipes are ranged widely, from oil pipeline design to blood flow modelling and turbulent drag reduction. There is only a handful of DNS studies on shear-thinning fluids, and in-depth analyses of the flow structures are very limited. There is no study on the fine-scale topology of shear-thinning fluids. The present work aims to explore the fine-scale topology of an increasingly shear-thinning turbulent pipe flow of power-law fluids. Visualization of the velocity fluctuation fields and $Q-$criterion are used to show the change in the flow structures when the power-law index decreases. The PDF distribution of the invariants of the velocity gradient, strain-rate, and rotation tensors are examined. To the author's best of knowledge, this is the first DNS study on the velocity-gradient tensor invariants for pipe flows of non-Newtonian fluids.

1.2 Thesis outline

This thesis is composed of 6 chapters. The introduction in Chapter 1 establishes the importance of studying wall turbulence, and the impact of DNS performed at increasingly higher Reynolds numbers. The motivation of the present study followed.

Chapter 2 gives a theoretical background of this research including a comprehensive literature review. The first part of the literature review revises the historical findings and models for the small-scale and large-scale coherent structures in wall turbulence. The second part focuses on the large-scale coherent structures, namely the uniform-momentum zones and the internal shear layers. The third part focuses on the progress on the understanding of pipe flow of non-Newtonian fluids. The last part explains the physical meaning of the velocity-gradient, strain-rate and rotation tensors and their invariants which are investigated for the non-Newtonian pipe flow in chapter 5.

The methodology section in Chapter 3 starts with the numerical method, i.e., the DNS configuration of the present pipe flow. The computational approaches, set-ups and spatial discretisation are presented. In this chapter, the coordinate transformation applied to the data in post-processing and the proper orthogonal decomposition used in data analysis are documented.

The results and discussion are divided in Chapters 4 and 5 for Newtonian and non-Newtonian fluids flow in the pipe, respectively. Both chapters begin with the mean flow statistics which are carefully validated with DNS results in the literature.

In Chapter 4, the DNS data of Newtonian pipe flow at four Reynolds numbers are investigated for the coherent structures, UMZs and ISLs. Four different methods in the two general approaches adopted in the literature are used for the identification of UMZs and ISLs. Extensive statistical analyses are performed to investigate the characteristics of the UMZs and ISLs, which are compared to the results of the channels and turbulent boundary layers.

In Chapter 5, the non-Newtonian fluid flows in the pipe are examined for three shear-thinning fluids at $Re_\tau \approx 180$. Visualisations, mean flow statistics and correlations of the streamwise velocity reveal the intermittent turbulence transition and the change in turbulence structures as the flow become more shear-thinning. The flow topology is investigated by the evolution of the invariants of the velocity-gradient, strain-rate, and rotation tensors as the flow become shear-thinning. These joint PDFs of the invariants for both the Newtonian and non-Newtonian fluids for the DNS data of pipe are presented. The turbulent spots are separated from the pseudo-laminar regions in the pipe. The universality of the famous 'Vieillefosse' tail of the $Q-R$ map is discussed for the transitional flow regime. In the most shear-thinning case, the instability wave a prior to the turbulence transition is extracted by means of volumetric conditional averaging and proper orthogonal decomposition (POD).

The results and discussion in Chapters 4 and 5 are each followed by a summary of the key findings. An overall conclusion of the present work is last placed in Chapter 6 where the contribution of this work in the understanding of wall turbulence is summarised.

Chapter 2

Background and literature review

2.1 Coherent structures in wall turbulence

The essential feature of turbulence is the chaotic three-dimensional energy-containing motions, i.e., eddies. Wall-bounded flows are particularly complex due to the presence of the wall which induces turbulent motions in multi-scales with scale interaction. The multi-scale interaction was described as a hierarchy of eddies with size growth from the wall towards the outer region in the attached eddy model (AEM) developed from Townsend's attached eddy hypothesis (Townsend (1976)). The coherence of such organised eddy structures was reviewed by Robinson (1991), Adrian (2007), Jiménez (2012) and Marusic and Monty (2019). The hierarchical scaling of eddies was conceptually illustrated by Perry and Chong (1982), Hwang (2015) and Marusic and Monty (2019), as reproduced in figure 2.1. In the diagram, small self-similar inner-scaled eddies populated near the wall are attached to the wall. These eddy structures grow in size towards the outer region and eventually become detached away from the wall. The attached and detached eddies correspond to the small-scale near-wall structures and the large-scale coherent structures namely the large- and very-large-scale motions (LSM/VLSM), respectively.

The coherent structures near the wall are well-known to be associated to quasi-streamwise vortices. In the near-wall region of wall turbulence, counter-rotating streamwise vortex pairs have been observed by Kline et al. (1967), Bakewell and Lumley (1967), Blackwelder and Eckelmann (1979), Head and Bandyopadhyay (1981), Smith and Metzler (1983), Kim et al. (1987). As in figure 2.2, these vortex pairs sweep and eject high- and low-speed fluid up and down, forming near-wall

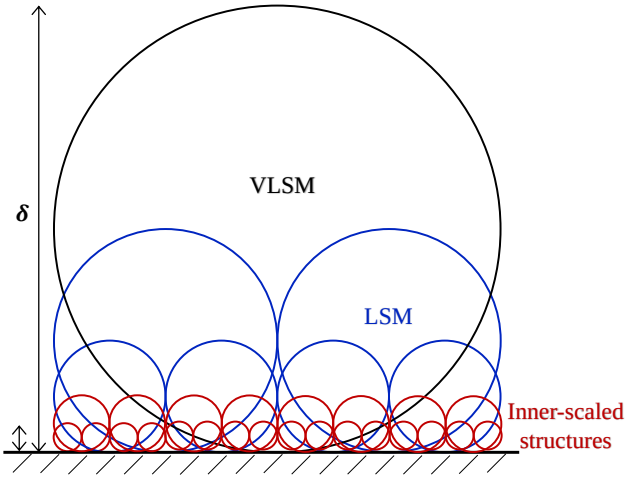

Figure 2.1: Schematic representation of Townsend's attached eddy hypothesis on the spanwise-wall-normal plane for a hierarchical distribution of eddies with size growth proportional to the distance from the wall. The drawing is the same as in Hwang (2015), similar to the hierarchy in Perry and Chong (1982).

steaks of high- and low-momentum pathways. The non-dimensional spanwise spacing of these streaks was found to be an invariant of the Reynolds number, approximately 100 wall units from both experiments (Kline et al. (1967); Nakagawa and Nezu (1981); Smith and Metzler (1983); Metzger and Klewicki (2001)) and DNS (Kim et al. (1987); Ahn et al. (2013)). The streak spacing increases when departing away from the wall. Smith and Metzler (1983) suggested that this is due to a merging (coalescence) process in the buffer layer. Above the buffer layer, the coalescence becomes highly $3D$ so that the flow pattern becomes too complex for deterministic streak identification. The vortex pairs are elongated from the wall, reinforcing the near-wall streaks to be streamwise elongated structures (Hinze (1975)) which can be up to several times longer than the boundary layer thickness δ (Hunt and Morrison (2000)) where δ is the TBL thickness, channel half height, and pipe radius. The near-wall streaks in turn, lift the vortices up to be inclined (Jiménez and Pinelli (1999)). The inclined vortices, originating from the wall and extending beyond the log-law region, correspond to the hierarchy of eddies of Townsend's attached eddy hypothesis. Adrian et al. (2000) described these streamwise vortex pairs as legs of hairpin/horse-shoe vortices.

The breakdown of the near-wall streaks was believed to be caused by outer-scale flow structures, i.e., LSMs (Smith and Metzler (1983)). The existence of LSM and VLSM was first found in the wall-bounded flows by Townsend (1951, 1976).

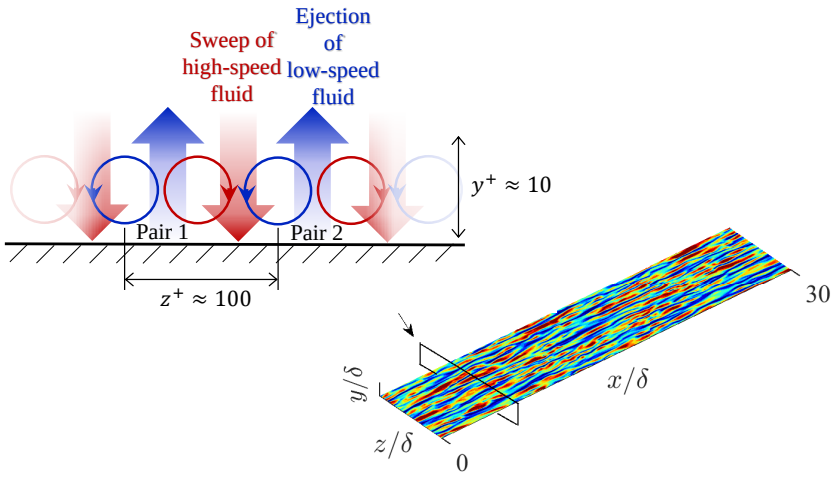

Figure 2.2: Conceptual illustration of the organised vortical structures near the wall: the counter-rotating streamwise vortex pairs and low- and high-momentum pathways induced by the ejections and sweeps between these structures. The contour of the streamwise velocity fluctuation shows the low- and high-speed streaks elongated in the streamwise direction in the pipe at $Re_\tau = 180$.

Correlations of the streamwise velocity revealed long coherent structures existing from the buffer layer to the lower outer region of the TBL (Kline et al. (1967); Falco (1977)). Kim and Adrian (1999) observed LSMs in a turbulent pipe flow over a wide range of Reynolds numbers. The LSMs are very energetic, carrying substantial portions of the streamwise turbulent kinetic energy (TKE) and Reynold shear stress (RSS) (Jiménez (1998); Marusic (2001)). The LSMs were found to be contributing nearly half of the total TKE and RSS in the channel (Liu et al. (2001)), pipe (Guala et al. (2006); Hellström and Smits (2014)), TBL (Lee and Sung (2011)) and Couette flows (Lee and Moser (2018)).

The role of LSMs in wall-bounded flows has drawn great attention; majority agreed on that the origin of LSM and VLSM is associated with the near-wall region (Kim and Adrian (1999); Hutchins and Marusic (2007b); Wu et al. (2012); Lee and Moser (2015)), as a bottom-up mechanism. Ganapathisubramani et al. (2003) suggested that the LSM originates from the attached eddies near the wall which convect into the log region and become detached in the outer region with coherent alignment. Recent studies believed that the LSM and VLSMs also modulate the near-wall small-scale turbulent activities as a top-down mechanism, known as large-scale modulation. LSMs and VLSMs can penetrate to the very-near-vicinity of the wall, leaving large-scale and low-frequency footprint in the near-wall region and

influence the small-scale turbulence (Rao et al. (1971); Metzger and Klewicki (2001); Jiménez et al. (2004)). The LSMs excite the near-wall ejections and sweeps (Falco (1977)). The strong near-wall $Q2$ ejection events known as bursting is linked with the outer-scale flow (Wark and Nagib (1991)). In Wang et al. (2017), the low-speed VLSMs suppressed near-wall ejections while the high-speed VLSMs enhanced the near-wall ejections with acceleration of the near-wall flow. Wu et al. (2012) reported that the VLSMs convect at approximately the bulk velocity even in the near-wall region and accelerate the near-wall flow while the small-scale structures near the wall decelerate the flow. Ahn et al. (2017) reported that this acceleration force of the VLSMs is balanced by the deceleration force of the near-wall structures.

Numerous studies focused on the interaction mechanism between the inner structures and outer LSMs. Results from filtering by Metzger and Klewicki (2001) showed that the influence of LSM on the near-wall structures is not simple superpositioning. Hutchins and Marusic (2007a,b) reported that the interaction between the LSMs and the near-wall flow is an amplitude modulation effect in which the LSMs modulate the small-scale activities near the wall (Marusic and Hutchins (2008)). Mathis et al. (2009a,b) applied Hilbert transformation on the streamwise velocity fluctuation to show the high-degree amplitude modulation of LSMs on the near-wall flow. The superimposition of large-scale energy on the near-wall cycle found in the experimental results by Marusic et al. (2010) was explained by the amplitude modulation effect. This amplitude modulation effect from LSM to the near-wall flow is well agreed by McKeon and Sharma (2010); Chung and McKeon (2010); Ahn et al. (2013) and Baars et al. (2017). Agostini and Leschziner (2014) reported that the modulation on near-wall streaks by LSM is asymmetric, which corresponds to the observations by Nakagawa and Nezu (1981) and Wark and Nagib (1991) where the near-wall streaks were found asymmetric. The modulation from the negative and positive streaks of low-frequency LSM on the near-wall high-frequency streaks is different and cause asymmetric response. This may explain the finding by Metzger and Klewicki (2001) who found that sweeps are larger than ejections near the wall. Yoon et al. (2016) found the streamwise vorticities around the low-speed near-wall streaks being attenuated more than the high-speed streaks. Agostini and Leschziner (2014, 2016) used the empirical mode decomposition (EMD) rather than Hilbert transformation without arbitrary cut-off wavelength to separate the LSM and near-wall structures. The EMD removed the LSM effect on the near-wall small-scale structures by removing large-scale footprints such as the convective displacement due to the large-scale acceleration, amplitude modulation and distortion caused by sweep-induced splatting.

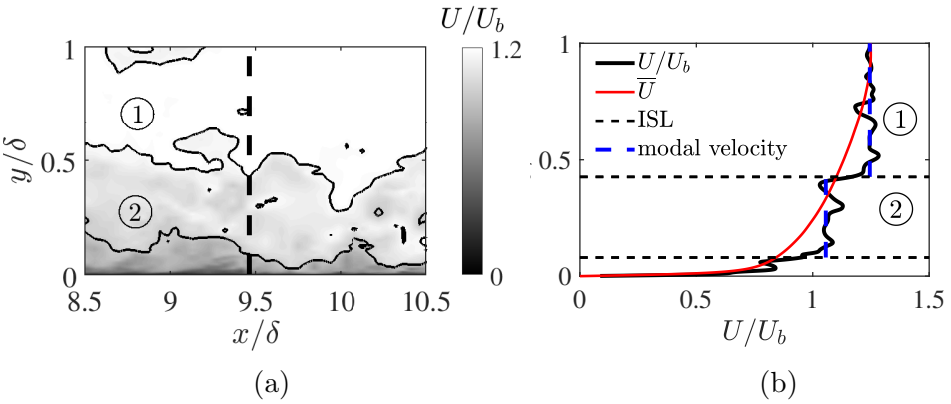

Figure 2.3: (a) Contour of the instantaneous streamwise velocity U of the present pipe DNS at $Re_\tau = 1000$. (b) Profiles of U at the streamwise location of the dashed line in (a). The uniform-momentum zones in this particular snapshot are shown: the horizontal dashed lines represent the internal shear layers demarcating the uniform-momentum zones 1 and 2; the vertical dashed lines mark the average U in each zone, namely the UMZ modal velocity.

2.1.1 Uniform-momentum zones and internal shear layers

Recent attentions on the coherent structures in wall turbulence have been focused on the uniform-momentum zones (UMZ), an instantaneous phenomenon first found in the experiment of a TBL by Meinhart and Adrian (1995). They observed separate large irregularly-shaped regions convecting at relatively uniform streamwise velocities. These regions, namely the UMZs were demarcated by thin high-shear regions with clustered spanwise vortices. Adrian et al. (2000) reported that the TBL was densely populated by thin structures with high vortical density which enveloped the UMZs. The streamwise velocity jumps abruptly across these thin regions. These thin high-shear structures have been referred as the internal shear layer (ISL), UMZ interface and the internal interfacial layer (IIL) in different studies (Priyadarshana et al. (2007); de Silva et al. (2017); Fan et al. (2019)) and are responsible for the internal transport of mass, momentum and heat in shear flows. The UMZs bounded between the ISLs are large-scale coherent structures, carrying a substantial amount of energy extracted from the mean flow by the ISL. Such zonal structural organisation is illustrated in figure 2.3. The contour of the streamwise velocity U from a random snapshot of the DNS of the present pipe flow is shown in figure 2.3(a), and the instantaneous velocity profile U at the streamwise location marked by the dashed line is plotted in figure 2.3(b). It can be clearly seen that the velocities are relatively uniform inside each zone where U fluctuates mildly around the average

velocity of each zone: the zone modal velocity. U exhibits a step-like profile, in which the velocity changes sharply when entering from one to another UMZ across the ISLs marked by dashed lines in figure 2.3(b).

The UMZs and ISLs were found in presence in all canonical wall-bounded flows. Kwon et al. (2014); Eisma et al. (2015); Yang et al. (2016); de Silva et al. (2016) and Chen et al. (2020) have shown that the TBL, channel and pipe flows exhibit a similar UMZ structural organisation. Across the ISL, step-like abrupt jumps in the streamwise velocity U, locally peaked spanwise vorticity, and local minimum of turbulent intensity were observed in the channel (Kwon et al. (2014); Yang et al. (2016)), pipe (Kwon (2016); Yang et al. (2017); Chen et al. (2020, 2021)) and TBL (de Silva et al. (2016, 2017)). Kwon et al. (2014), Yang et al. (2016) and Chen et al. (2019b) studied the innermost UMZ in the channel and pipe, called the quiescent core. The quiescent core region in the turbulent channel flow was defined at a velocity threshold of 95% of the centreline streamwise velocity U_{CL} by Kwon et al. (2014) and Yang et al. (2016). Inside the quiescent core, turbulence intensity is very low. In Kwon et al. (2014), the quiescent core of the channel was found to be very large which can occupy more than half of the channel height on average. The quiescent core displayed significant meandering, thickening and thinning behaviours, and can penetrate very close to the walls, matching the observations by Antonia et al. (1992) where traced flow element originated from the channel wall could penetrate to the near-wall region of the opposite wall. The core is bounded by thin interface of strong shear. Yang et al. (2016) observed a strong distribution density of prograde vortices accompanied by locally minimised retrograde vortices across the quiescent core boundary.

de Silva et al. (2016) investigated multiple UMZs in the TBL. The number of UMZs increased log-linearly with the Reynolds number. The thickness of the UMZ increased as a function of the wall-distance, forming a hierarchical distribution of UMZs in the boundary layer. The hierarchical structural arrangement matched the scaling model by Perry and Chong (1982) in figure 2.1. The subsequent study by de Silva et al. (2017) found the velocity jump across the ISL to be inversely proportional to the wall-distance, being more abrupt when closer the wall. The thickness of the ISLs was also a function of the wall-distance, being thicker when moving away from the wall. The dynamical evolution of UMZ investigated by Laskari et al. (2018) showed that when the number of UMZ increases, all existing UMZs become thinner and move away from the wall with a higher modal velocity to compensate for the new zones. The hierarchical scaling of the UMZs, i.e., thinner zones and sharper velocity jumps across thinner ISLs nearer the wall, formed the basis of a

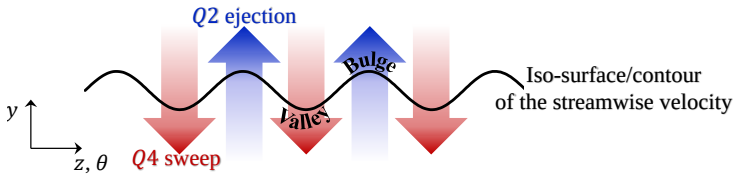

Figure 2.4: Schematic illustration of ISL (UMZ interface) contortion associated to LSMs.

UMZ-vortical fissure model by Bautista et al. (2019). Turbulence statistics were reproduced using a step-like initial velocity profile resembling the hierarchical UMZ behaviour of the flow in a TBL.

The ISLs are very tortuous, with bulges and valleys similar to the large-scale engulfment feature of the turbulent/non-turbulent interface (TNTI). In Kwon et al. (2014), the ISL bounding the channel quiescent core showed significant meandering in the wall-normal direction on the streamwise-wall-normal plane. The contortion of the ISLs defined as iso-contours or iso-surfaces of the streamwise velocity, i.e., the wall-normal fluctuation of the ISL location, manifests the LSMs in wall turbulence (Yang et al. (2017)). Figure 2.4 schematically shows the bulges and valleys on the contorted ISL associated to the LSMs. Bulges and valleys on the ISL are induced by the ejections of low-speed fluids up away from the wall and the sweeping of high-speed fluids towards the wall, respectively. The clustered vortical structures along the ISL are responsible for $Q2$ ejections and $Q4$ sweeps around the ISL (Tomkins and Adrian (2003); Ganapathisubramani et al. (2003)). The reconstructed velocity field using an LSM model by Saxton-Fox and McKeon (2017) largely reproduced the classical features of UMZs including the large-scale bulges on the ISLs. The level of contortion (tortuosity) of the $2D$ ISLs was quantified by Yang et al. (2016) by measuring the length of ISL per unit length in the streamwise and the spanwise directions of the channel. The ISL tortuosity was found higher in the spanwise direction compared to the streamwise direction. de Silva et al. (2017) found that the ISLs are more tortuous when being further away from the wall. Kevin et al. (2019) confirmed that the ISL contortion intensifies with increasing distance from the wall.

On the detection of UMZ

The UMZ identification technique varies across studies, which may be classified into two general categories: the PDF-based methods and the ISL-based methods.

Study	Re_τ	Identification	Quantity	Threshold
Eisma et al. (2015)	2053	Triple decomposition	ω_{SH}	Composite criterion
Gul et al. (2020)	340 – 1259	Extraction of vortex-sheets	$[A_{ij}]_+$	1.5 × local mean $[A_{ij}]_+$

Table 2.1: ISL-based identification methods and user-defined parameters used in the ISL-based studies. ω_{SH} is the shear component of vorticity obtained from the shear component of the velocity-gradient tensor; $[A_{ij}]_+$ is the largest eigenvalue of $A_{ij} = S_{ik}\omega_{kj} + S_{jk}\Omega_{ki}$.

Study	Re_τ	Identification	$\mathcal{L}_x/\delta$	$\mathcal{B}/U_\infty(\%)$
Adrian et al. (2000)	358, 831, 2022		1.2	3.0, 2.5, 0.9
Kwon et al. (2014)	1000–4000	Double-pdf	1.2	1.25
Yang et al. (2017)	930	Double-pdf	2.0	–
de Silva et al. (2016)	$10^3 - 10^4$	Peak detection	2.0	1.5
de Silva et al. (2017)	$10^3 - 10^4$	Peak detection	2.0	2.0
Heisel et al. (2020)	$3800 - 10^6$	Peak detection	0.1	2.0
Laskari et al. (2018)	5300	Constrained peak detection	0.5	1.5
Chen et al. (2020)	500	Constrained peak detection	0.2	1.0
Fan et al. (2019)	550–5186	Kernel density estimation		

Table 2.2: PDF-based identification methods and user-defined parameters used in the PDF-based studies.

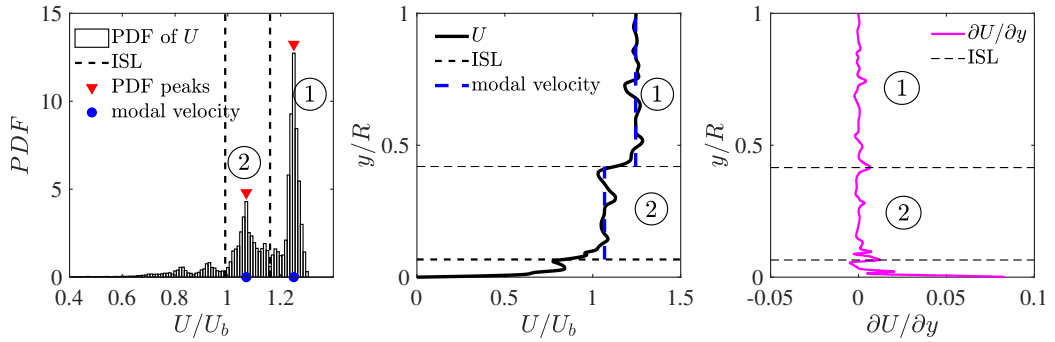

Figure 2.5: Illustration of (a) PDF-based and (c) ISL-based identification method for UMZs and ISLs. The velocity profile in (b) is the same as in figure 2.3(b).

The PDF-based methods seek for large regions of similar instantaneous streamwise velocity U (modal velocity), which result in distinct peaks on the probability density function (PDF) of U (Adrian et al. (2000)). This is demonstrated in figure 2.5(a) for the same snapshot used in figure 2.3. The peaks on the PDF of U represent large regions travelling at similar velocities, i.e., modal velocities at the peaks. The UMZ interface are then identified between the adjacent peaks. The ISL-based methods directly seek for the location of ISL/UMZ interface as thin regions of high shear, and then identify the UMZs as regions bounded between the ISLs as illustrated in figure 2.5(c). Studies using the ISL-based and the PDF-based methods are listed in table 2.1 and 2.2, respectively. The recent ISL-based experimental study by Gul et al. (2020) identified the ISLs as sheet-like vortex structures in regions with highly correlated strain-rate and vorticity. Most of the UMZ studies (Kwon et al. (2014); de Silva et al. (2016, 2017); Yang et al. (2017); Laskari et al. (2018); Fan et al. (2019); Chen et al. (2020) adopted the PDF methods following Adrian et al. (2000) to identify the UMZs from the PDF of U. de Silva et al. (2016, 2017) defined the ISLs in the middle between two adjacent peaks and Chen et al. (2020) defined the ISLs at the minimum bin between the neighbouring peaks. The PDF-based studies themselves differ in the constraints when sampling for the PDF peaks. Kwon et al. (2014) and Yang et al. (2017) used a double-histogram method, all the peaks (modal velocities) on the instantaneous histograms of U (such as the peaks on figure 2.5(a)) are collected; a secondary histogram of all the modal velocities revealed the most frequently-occurred UMZ, i.e., the quiescent core. Majority of the local UMZs and their modal velocities at the PDF peaks would not be persistent enough to survive in the secondary PDF. de Silva et al. (2016, 2017); Chen et al. (2020) kept all the instantaneous local UMZ recognised in their peak detection process and grouped them based on their modal velocities.

The number of UMZ and ISL identified in a flow depends on the detection method, and is sensitive to the parameters used in each method. The key limitation of the PDF-based methods is that the PDF must be computed in a small domain. A sampling domain being too large is equivalent to spatial averaging in which the peaks on the PDF of U will diminish. The streamwise sub-domain length $\mathcal{L}_x$ used in each study is listed in table 2.2. In Kwon et al. (2014); de Silva et al. (2016) and de Silva et al. (2017), the histograms of U were computed from a $2D$ subdomain with $\mathcal{L}_x = 2\delta$. In Chen et al. (2020), the histograms were computed by using $3D$ snapshots with a much shorter streamwise length $\mathcal{L}_x = 0.2R$ to compensate the spanwise averaging of U. The bin size $\mathcal{B}$ of the histograms also affects the PDF peak detection for UMZ identification. A bin size being too small would results in

spurious PDF peaks, whereas a bin size too large may be incapable to show distinct peaks. Laskari et al. (2018) and Chen et al. (2020) used constraints for spurious peak filtering. Laskari et al. (2018) additionally used a temporal filter to remove UMZs lived too short for the analysis on the UMZ temporal evolution. Fan et al. (2019) replaced the discrete histogram with continuous kernel density estimation (KDE) functions of U with a bandwidth $h = \frac{4}{3}^{1.5}\sigma N^{-1.5}$ (σ is the standard deviation of U and N is the sample size of U used for a KDE) which self-adjusts with the sample size of U. The KDE algorithm is insensitive to $\mathcal{L}_x$ and suggested a lower number of recognised UMZ on average than the traditional PDF-based studies. The PDF-based methods including Fan et al. (2019)'s KDE method, although differ in the number of recognised UMZ, reported qualitatively consistent UMZ characteristics.

The ISL-based studies in table 2.1 directly detect the ISLs by extracting high shear regions, the ISLs were defined by setting thresholds on the shear strength. The user-defined parameters decide which UMZ or ISL to be collected. A stricter constraint or threshold trims the sample of local UMZs in which the PDF-based and the ISL-based methods will preferentially preserve the relatively large UMZs (higher peaks in the PDF of U) and strong ISLs (higher local shear strength), respectively.

2.2 Non-Newtonian pipe flow

The fundamental difference between a Newtonian and a non-Newtonian fluid is that the viscosity of a non-Newtonian fluid changes with the shear stress, i.e., the relationship between the shear stress and the shear rate is non-linear due to variable viscosity. The non-Newtonian fluids with variable viscosity may be classified into two types: one with time-dependent viscosity and the other one with time-independent viscosity. The latter type of non-Newtonian fluids can be further categorised as viscoplastic fluids and viscoelastic fluids. In viscoplastic fluids, the viscosity and shear-rate are functions of shear stress only.

- Non-Newtonian fluids
  - Time-dependent
    - Thixotropic
    - Rheopectic
  - Time-independent
    - Shear-thinning
    - Shear-thickening
    - Bingham

Figure 2.6 shows the general functions of shear stress versus shear-rate for different kinds of viscoplastic fluids. This study is limited to shear-thinning fluids which exhibit decreased viscosity with increasing shear rate. An example of such nature is ground liquefaction during earthquakes when massive shear results in dramatically decreased material viscosity and turns clay to liquid. In reality, most industrial fluids and body fluids are non-Newtonian, and many of them are shear-thinning, e.g., oil and slurries. The number of studies on wall-bounded flow of shear-thinning fluids are very limited compared to Newtonian flows. The experimental studies on shear-thinning fluid flows in the pipe are listed in table 2.4. Table 2.3 lists the rheology models of the non-Newtonian fluids. The experiments of shear-thinning fluids without yield-stress behaviour, fitted by the power-law model rather than the Herschel-Bulkley model are more relating to this study. The power-law rheology describes shear-thinning ($n < 1$), shear-thickening ($n > 1$) and Newtonian fluids ($n = 1$).

Fitz-Gerald (1974) used the power-law rheology in the numerical model of glandular secretion in pipes, below a certain power-law exponent n, laminar and turbulent flows co-existed. In the experiments by Pinho and Whitelaw (1990) and Draad et al. (1998), turbulent transition was delayed in shear-thinning fluids, the critical Reynolds number Re_{cr} for transition increased, the flow was still not fully turbulent at $Re_D \approx 7700$ for $n = 0.56$. In the experiment by Biswas et al. (2016)

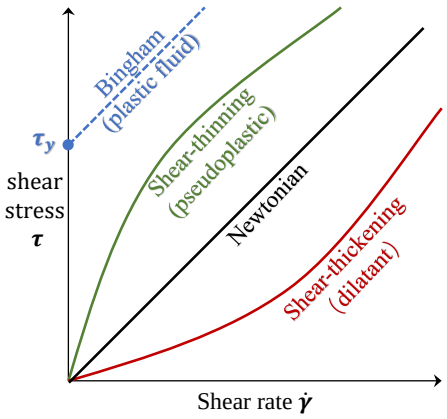

- Shear-thinning:
  the apparent viscosity decreases with increasing shear rate
- Shear-thickening:
  the apparent viscosity increases with increasing shear rate
- Bingham:
  the fluid behaves like a rigid body for $\tau < \tau_y$ (τ_y is the yield stress)

Figure 2.6: Relationship between the shear rate and shear stress for different types of time-independent non-Newtonian fluids.

	Model	
Generalised models	Power-law	$\mu = K\dot{\gamma}^{n-1}$
	Cross power-law	$\mu = \mu_\infty + \frac{\mu_0-\mu_\infty}{1+(K\dot{\gamma})^n}$
	Carreau	$\mu = \mu_\infty + \frac{\mu_0-\mu_\infty}{(1+(\lambda_c\dot{\gamma})^2)^{n/2}}$
	Carreau-Yasuda	$\mu = \mu_\infty + \frac{\mu_0-\mu_\infty}{(1+(\lambda_c\dot{\gamma})^a)^{n/a}}$
Yield-stress models	Herschel-Bulkley	$\mu = \tau_y/\dot{\gamma} + K\dot{\gamma}^{n-1}$
	Casson	$\sqrt{\tau} = \sqrt{\tau_y} + \sqrt{\mu_\infty\dot{\gamma}}$
	Quemada	$\mu = \mu_0\left(1 - \frac{1}{2}H\frac{k_0-k_\infty\sqrt{\dot{\gamma}}}{1+\sqrt{\dot{\gamma}}}\right)$

Table 2.3: Rheology models for non-Newtonian fluids. μ is the apparent viscosity as function of shear-rate. K (fluid consistency coefficient), n (power-law index), μ_0 (viscosity at zero shear rate), μ_∞ (viscosity at infinite shear rate) and τ_y (yield stress) are constant. λ_c, H, k_0 and k_∞ are empirical constant parameters of the models.

of blood flow as a shear-thinning fluid in a rigid pipe, Re_{cr} was delayed in blood compared to a Newtonian fluid so that using a Newtonian model for blood in the transition regime of the flow may leads to wrong medical predictions. Pinho and Whitelaw (1990) quantified the delay of turbulence transition and the suppression of turbulent fluctuations particularly in the radial and azimuthal directions of the pipe due to the shear-thinning effect. Stability analysis by Draad et al. (1998) suggested that the delay in turbulence transition is caused by the elongated polymers which stabilise the flow by increasing the critical disturbance velocity. The relationship between the critical velocity for turbulence transition in shear-thinning fluids in pipes and the pipe diameter were determined by Mitchell and Myers (2007). Peixinho et al. (2005) investigated laminar, transitional and fully-turbulent flows in the pipe of shear-thinning fluids with a yield stress (Herschel-Bulkley rheology) and without a yield stress (power-law rheology). The turbulence transition of shear-thinning fluids showed an increase of the root mean square (RMS) of the axial velocity. The RMS axial velocity in shear-thinning fluids was found larger than the Newtonian flow in the near-wall region.

The experiment by Nouri et al. (1993) for concentric and eccentric annuli of shear-thinning fluids suggested that the turbulent fluctuation is lowered in all three (axial, azimuthal and radial) directions, but is more significantly in the off-axial directions. Escudier and Presti (1996) measured velocity fluctuations in the flow of clay which fitted accurately to the Herschel-Bulkley rheology. They confirmed the suppression of off-axis turbulence intensities in the shear-thinning fluid while the axial turbulence intensity was found similar to the Newtonian case. The reduction of off-axis turbulent intensities leads to drag reduction. Nouri et al. (1993) reported that the drag reduction in shear-thinning pipe flow can achieve above 60%. In Draad et al. (1998), a reduction over 20% in the turbulent intensity compared to Newtonian fluids were found in the radial and the azimuthal directions which was explained by the suppression on small-scale turbulence. Escudier et al. (1999) suggested that the drag reduction from the lowered turbulence intensity occurs beyond the viscous sublayer in the buffer layer and can expand into the log-law region.

Peixinho et al. (2005) and Escudier et al. (2005, 2009) also investigated on the asymmetric mean axial velocity profile in transitional shear-thinning fluid flow in the pipe reported by Escudier and Presti (1996). Such asymmetry only appears in the transitional regime, the mean velocity profiles in laminar and fully-turbulent flows of non-Newtonian fluids are axisymmetric, similar as in Newtonian fluids. The asymmetry was found to be apparent during the whole stage of transition and was time-varying (Benslimane et al. (2016)). The greater the shear-thinning

characteristics, the stronger the fluid asymmetry appears (Wen (2016)). In the transitional regime, the degree of asymmetry approximately grows with the square root of Reynolds number. Esmael and Nouar (2008) and Esmael et al. (2010) studied the three-dimensional features associated to the asymmetric mean axial velocity profile in transitional shear-thinning pipe flow. Large-scale coherent structures of two counter-rotating longitudinal vortices were observed which were responsible for the turbulent transition to a weak turbulence.

The DNS studies of shear-thinning fluids using the power-law rheology model (including cross power-law) are listed in table 2.5. Rudman et al. (2001) conducted experiments and DNS of a weakly turbulent flow of a thixotropic fluid in the pipe using the power-law rheology. The simulation results using the power-law rheology showed significant discrepancy with the experimental results by under-predicting the superficial flow velocity by approximately 30%. The results suggested that time-dependent thixotropic fluids cannot be modelled by the simple power-law. The essential difference between a shear-thinning fluid and a thixotropic fluid is whether it is time-dependent. A shear-thinning fluid has a variable viscosity which is solely dependent on the shear rate, and the viscosity changes instantly with the shear rate. Thixotropic fluids are similarly to shear-thinning fluids but the behaviour is time-dependent; when shear rate increases, the viscosity decreases gradually with a delayed response. Therefore, the change in rheology and flow structures in a thixotropic fluid is relatively slow compared to shear-thinning fluid when subjected to immediate change in the shear rate.

The DNS results by Rudman et al. (2001) suggested that the axial turbulent intensity is marginally higher in non-Newtonian fluids. Rudman et al. (2004) examined the effect of different parameters in the power-law and the Herschel-Bulkley rheology on shear-thinning fluids in the pipe. The flow was not fully-developed at all three indices investigated from $n = 0.5$ up to $n = 0.75$. As the flow index decreases, the near-wall streaks which is a universal feature of wall-bounded flows (Kline et al. (1967)) became less homogeneous and the turbulent flow became intermittent. The temporal signals of velocity and pressure near the wall at different index suggested that the most shear-thinning case ($n = 0.5$) is significantly different than the flows at higher indices. The $2D$ contours of the streamwise velocity suggested that the flow at $n = 0.5$ is transitional with self-sustaining structures similar to the turbulent slugs in transitioning flow of Newtonian fluids.

Zhen et al. (2013) performed DNS of three shear-thinning fluids using the power-law model and particularly analysed the most shear-thinning case ($n = 0.7$) with comparison to the Newtonian fluid. The effect of shear-thinning on the evo-

lution of a hairpin vortex was investigated in a channel. The turbulent energy dissipation was found higher in the more shear-thinning flows with lower n. A possible mechanism for the delay of turbulence transition in shear-thinning fluids was suggested to be associated to the weakening of hairpin vortices which is believed to be the topological building blocks of wall turbulence in many studies. While the hairpin vortices are relatively intact in the Newtonian case, as the flow becomes shear-thinning, the vortices started to lose coherence and broke up into smaller-scale structures due to strong vortex instability. The weakening of vortices in purely shear-thinning (viscoplastic rather than viscoelastic) flows was believed to be associated with an instability of the vortices which leads to increased viscous dissipation.

Singh et al. (2017) investigated the turbulent kinetic energy budget of shear-thinning pipe flow using the DNS data of power-law fluids. The effect of shear-thinning on the turbulent kinetic energy production, transport and dissipation was evaluated. The shear-thinning effect suppressed the overall turbulent kinetic energy production. The shear-thinning effect on the turbulent kinetic energy budget was found to be confined approximately within $y^+ < 60$. Additional terms in the mean momentum equation and dissipation terms are introduced by variable viscosity. The additional negative term in the mean momentum equation increases in magnitude as n decreases and results in increasing mean velocity gradient in a more shear-thinning fluid. The additional dissipation term in the kinetic energy budget equation results in a net decrease in the total viscous dissipation.

Gavrilov and Rudyak (2016, 2017) investigated power-law shear-thinning fluids in the pipe at higher Reynolds numbers. The reduction of off-axis fluctuations was linked to the suppression of energy transport from axial streamwise component to off-axis components. This suppression on off-axis turbulent activities leads to a strong axial velocity pulsation. As the flow became more shear-thinning, the turbulent momentum transfer between near-wall region and the outer region reduced. The increase of viscosity away from the wall due to decreasing shear rate leads to the damping of the wall-normal velocity pulsations. The damped wall-normal fluctuation is responsible for the reduction of the momentum transport from the pipe core toward the wall.

	Method	Fitting model	n	Re_g
Pinho and Whitelaw (1990)	PIV	Power-law	0.56	240~7700
			0.64	7800~15000
			0.75	720~30000
			0.90	1480~43000
Nouri et al. (1993)		Power-law	0.75	8900, 26600
Escudier and Presti (1996)	Doppler anemometer	Herschel-Bulkley	5.35	550~25300
Escudier et al. (2005)	Doppler anemometer	Carreau-Yasuda	0.376-0.673	540~45300
		Herschel-Bulkley	0.423-0.534	550~25300
Peixinho et al. (2005)	Laser Doppler	Cross power-law	0.68, 0.71	2100~2700
Esmael and Nouar (2008)	Laser Doppler	Herschel-Bulkley	0.47, 0.5	1805~4867
Escudier et al. (2009)	Doppler anemometer	Carreau-Yasuda	0.66	2110~16020
Esmael et al. (2010)	Laser Doppler	Herschel-Bulkley	0.5	1805~4867
Biswas et al. (2016)	Doppler ultrasound			1000~3300
Wen (2016)	PIV	Carreau-Yasuda	0.366-0.727	1210~7939
Benslimane et al. (2016)	Doppler ultrasound	Herschel-Bulkley	0.59-0.79	360~2920

Table 2.4: Experimental studies of shear-thinning (with and without yield stress) non-Newtonian fluids flow in straight pipes.

	Numerical method	n	Re_τ	Re_g	L_x/R
Rudman et al. (2001)	SEM	0.69	180	3964, 5500	6π
Rudman et al. (2004)	SEM	0.5	180	5339	8π, 16π
		0.69	180	5501	10π
		0.75	180	5514	8π
Zhen et al. (2013)	Pseudo-spectral	0.7	140, 200, 258	4000,6000,8000	8π
		0.8			
		0.9			
Gavrilov and Rudyak (2016, 2017)	FVM	0.4	446	18150	15
		0.5	251	9200	
		0.6	267, 492	9400, 18760	
		0.7	280	9600	
		0.8	292, 530	9800, 19460	
Singh et al. (2017)	SEM	0.4	323	11862	8π
		0.6		11093	
		0.8		10630	

Table 2.5: DNS studies of non-Newtonian fluids flow in straight pipes.

2.3 Invariants of the velocity-gradient tensors

The turbulent structures in fine scales can be characterised by the invariants of the velocity-gradient tensor. For incompressible flow, the velocity-gradient tensor (VGT) $A_{ij} = \partial U_i/\partial x_j$ can be decomposed into symmetric part and antisymmetric part as $A_{ij} = S_{ij} + \Omega_{ij}$, where the symmetric strain-rate tensor

$$S_{ij} = \frac{1}{2}\left(\frac{\partial U_i}{\partial x_j} + \frac{\partial U_j}{\partial x_i}\right), \tag{2.1}$$

and the anti-symmetric rate-of-rotation tensor

$$\Omega_{ij} = \frac{1}{2}\left(\frac{\partial U_i}{\partial x_j} - \frac{\partial U_j}{\partial x_i}\right). \tag{2.2}$$

Ω_{ij} can be expressed by components of vorticity $\boldsymbol{\omega} = \nabla \times \mathbf{U}$ as

$$\boldsymbol{\Omega} = \frac{1}{2}\begin{bmatrix} 0 & -\omega_3 & \omega_2 \\ \omega_3 & 0 & -\omega_1 \\ -\omega_2 & \omega_1 & 0 \end{bmatrix}.$$

The vorticity (curl of the velocity field) in the Cartesian coordinates and the cylindrical coordinates has

$$\boldsymbol{\omega} = \left(\frac{\partial v_z}{\partial y} - \frac{\partial v_y}{\partial z}\right)\mathbf{e}_x + \left(\frac{\partial v_x}{\partial z} - \frac{\partial v_z}{\partial x}\right)\mathbf{e}_y + \left(\frac{\partial v_y}{\partial x} - \frac{\partial v_x}{\partial y}\right)\mathbf{e}_z, \tag{2.3}$$

and

$$\boldsymbol{\omega} = \left(\frac{1}{r}\frac{\partial v_z}{\partial \theta} - \frac{\partial v_\theta}{\partial z}\right)\mathbf{e}_r + \left(\frac{\partial v_r}{\partial z} - \frac{\partial v_z}{\partial r}\right)\mathbf{e}_\theta + \frac{1}{r}\left(\frac{\partial (r v_\theta)}{\partial r} - \frac{\partial v_r}{\partial \theta}\right)\mathbf{e}_z, \tag{2.4}$$

respectively. The characteristics equation of A_{ij},

$$\lambda^3 + P\lambda^2 + Q\lambda + R = 0 \tag{2.5}$$

has three invariants. The first invariant P is the negative trace of A_{ij}. Thus, for incompressible flows, $P = -A_{ii} = 0$.

$$Q = \frac{1}{4}(\omega_i\omega_i - 2S_{ij}S_{ij}) \tag{2.6}$$

$$R = -\frac{1}{3}(S_{ij}S_{jk}S_{ki} + \frac{3}{4}\omega_i S_{ij}\omega_j) \tag{2.7}$$

The second and third invariants, Q and R in equations (2.6) and (2.7) can each be decomposed to constituent strain-rate and rotation part, which are the invariants of the strain-rate and rotation tensors: Q_ω is half the enstrophy; Q_s is proportional to the rate of dissipation, ε, as $Q_s = -\varepsilon/4\nu$; R_s represents strain skewness; R_ω is the enstrophy production.

$$Q_\omega = \frac{1}{4}\omega_i\omega_i \tag{2.8}$$

$$Q_s = -\frac{1}{2}S_{ij}S_{ij} \tag{2.9}$$

$$R_s = -\frac{1}{3}S_{ij}S_{jk}S_{ki} \tag{2.10}$$

$$R_\omega = -\frac{1}{4}\omega_i S_{ij}\omega_j \tag{2.11}$$

The physical interpretation for these invariants was extensively reviewed by Chong et al. (1990), Cantwell (1993), Soria et al. (1994), Blackburn et al. (1996) and Tsinober (2009). The sign of Q represents the local dominance between Q_ω and Q_s, between rotation and strain, and between enstrophy and dissipation, i.e., $Q > 0$ represents excess of enstrophy over strain product and $Q < 0$ represents regions where viscous dissipation of kinetic energy dominates. Regions of strong Q_ω ($Q > 0$) are occupied by tube-like structures and regions of strong Q_s are concentrated with sheet- or ribbon-like structures (da Silva and Pereira (2008)).

These invariants are often plotted as joint PDFs in the $Q-R$, Q_s-Q_ω, Q_s-R_s and $Q_\omega - R_\omega$ space. Figure 2.7 shows the physical interpretations of the PDFs. The $Q-R$ space is divided into four sectors by the line of discriminant $D = (27/4)R^2+Q^3$. The physical meaning of $Q-R$ distributions depends on the signs of R and D. When $D > 0$, the local flow is predominantly swirling (high enstrophy); sector I ($R > 0$) implies predominant vortex compression over stretching and sector II ($R < 0$) implies the opposite. When $D < 0$, the local flow is predominantly straining; sector III ($R < 0$) indicates tube-like structures and sector IV ($R > 0$) sheet-like structures. The $Q-R$ joint PDF exhibited a preferential distribution - a upturned 'tear drop' shape in a vast group of turbulence. The 'tear drop' shape is formed by the 'Vieillefosse tail' (Vieillefosse (1982)) of high rate of kinetic energy dissipation along $D = 0$ in $R > 0$ and enlarged sector II over sector I, i.e., vortex stretching over vortex compression (Cantwell (1993)). Figure 2.7 shows the physical interpretation for the $Q_\omega - Q_s$ and $Q_\omega - R_\omega$ space similar to Soria et al. (1994), da Silva and Pereira (2008) and Buchner et al. (2016). In the $Q_\omega - Q_s$ space, the line of $Q_\omega = -Q_s$ indicates vortex

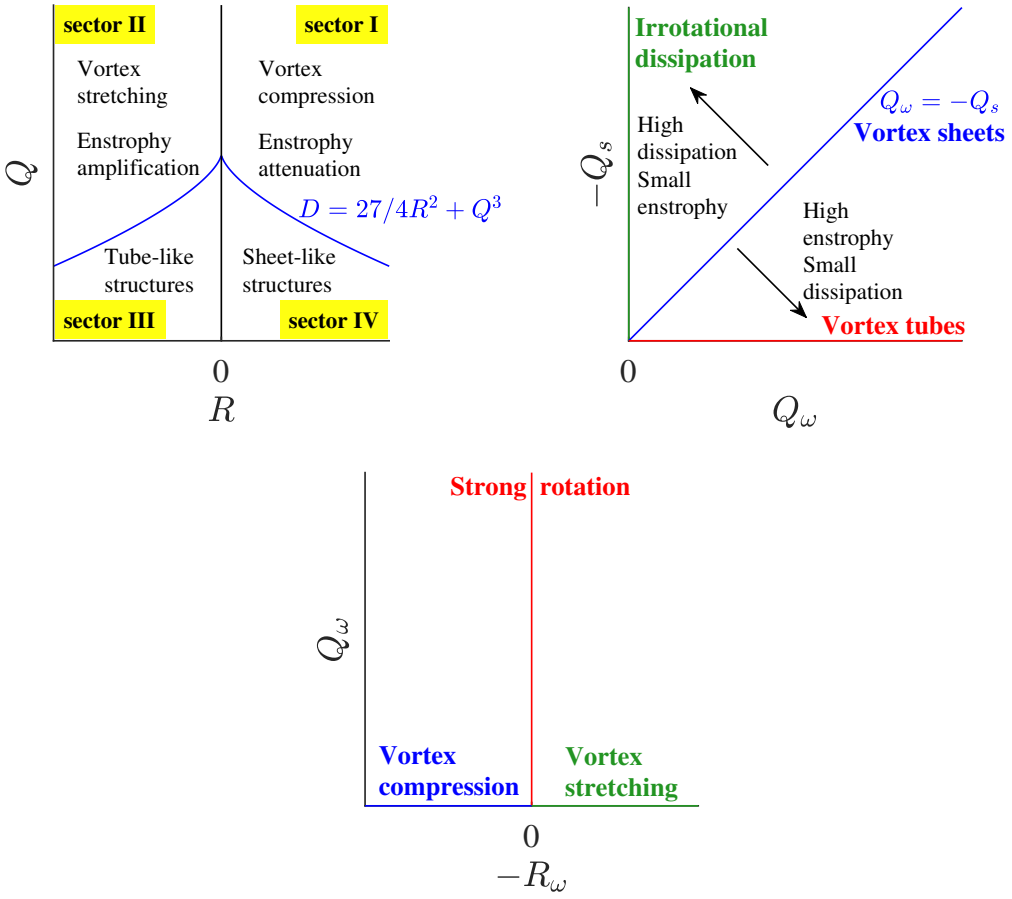

Figure 2.7: Physical interpretations for the velocity-gradient tensor invariants $Q-R$, $Q_s - Q_\omega$ and $Q_\omega - R_\omega$ space.

sheet structures with balanced enstrophy and kinetic energy dissipation. Unlike the ubiquity of the $Q-R$ distribution, the Q_s-Q_ω joint PDF in wall-bounded flows is very different from the free shear flows and homogeneous isotropic turbulence. Wall-bounded flows are inhomogeneous due to the mean shear and the presence of self-similar hierarchical-scaled vortices originated from the wall. The mean shear which fuels turbulence production in shear flows is exerted (steered) by the viscous force from the wall, and results in a more complex topology of the multi-scaled turbulent motions. In the viscous sublayer of the channel flow by Blackburn et al. (1996) and Couette-Poiseuille flow by Wu et al. (2019), the joint PDF of Q_s-Q_ω was found to be nearly aligned along $Q_\omega=-Q_s$ because of the superior mean shear near the wall where enstrophy and dissipation are both very strong. Blackburn et al. (1996) also reported that the influence of the presence of the wall gradually disappeared from the PDFs beyond buffer layer in which the PDFs in the outer region became ubiquitous to free shear flows.

Chapter 3

Methodology

3.1 Direct numerical simulation

The present study investigates fully-developed turbulent pipe flows at Reynolds numbers up to $Re_\tau = 1000$ by means of direct numerical simulation (DNS). The three-dimensional incompressible Navier-Stokes equations are solved for fields of fluid velocity $\mathbf{u}$ and pressure p by a massively parallelized MPI (Message Passing Interface) solver, Nek5000 (Fischer et al. (2008)). Nek5000 is extensively used in the research group for simulations of turbulent flows in pipes, channels, annulus, and jets. The continuity equation of mass conservation (zero divergence of $\mathbf{u}$ for incompressibility),

$$\nabla \cdot \mathbf{u} = 0, \tag{3.1}$$

and the equations of momentum conservation,

$$\rho \frac{D\mathbf{u}}{Dt} = \rho\left(\frac{\partial \mathbf{u}}{\partial t} + \mathbf{u} \cdot \nabla \mathbf{u}\right) = -\nabla p + \nabla \cdot \boldsymbol{\tau} + \mathbf{f} \tag{3.2}$$

are solved by using the high-order spectral element method (SEM) which is a weighted residual method. The simulations of flows at high Reynolds numbers benefit from the reduced numerical dispersion and dissipation of the SEM with spectral accuracy. In the simulation, the fluid density is kept as $\rho = 1$, and no external force $\mathbf{f}$ is applied. The flow is driven by the pressure force, $-\nabla p$, i.e., an axial pressure gradient $\partial p/\partial x$. For incompressible flows, the general viscous stress tensor, $\boldsymbol{\tau} = \mu\big(\nabla \mathbf{u} + (\nabla \mathbf{u})^T\big) - \frac{2}{3}\mu(\nabla \cdot \mathbf{u})I$ where I is the identity matrix is reduced to $\boldsymbol{\tau} = \nabla \cdot \big(\mu(\nabla \mathbf{u} + (\nabla \mathbf{u})^T\big)$. For Newtonian fluids with a constant viscosity μ, the viscous force, $\nabla \cdot \boldsymbol{\tau}$ is simplified as $\nabla \cdot \boldsymbol{\tau} = \mu \nabla^2 \mathbf{u}$ (∇^2 is the Laplacian operator), and the full stress tensor is only solved in simulations of non-Newtonian fluids with

variable viscosity. Nek5000 adopts a semi-implicit time scheme, in which the viscous terms are solved implicitly by a third-order backward differentiation (BDF3) while the non-linear terms are solved by a third-order extrapolation (EXT3).

The boundary condition of the pipe is set as no-slip at the wall, and the periodic condition is applied in the streamwise direction, at the inlet and outlet of the pipe. In this study, the radial, azimuthal and axial/streamwise directions of the pipe are denoted as r, θ and x, respectively. The wall-normal location $y = R - r$ where R is the pipe radius. The solutions are solved in the Cartesian coordinates without encountering the singularity associated with the cylindrical coordinates at the pipe centreline (Jung and Chung (2012); Wang et al. (2018)). The horizontal and the vertical directions in the Cartesian coordinates are denoted as x_c and y_c, respectively in order to differ from the notation of the streamwise direction, x, and the wall-normal direction, y. The velocity components in the horizontal and vertical directions of the Cartesian coordinates are U_x and U_y, respectively. The velocity components U, V and W are in the streamwise, wall-normal and azimuthal directions of the cylindrical coordinates. The radial and azimuthal velocities, V_r and W are obtained via vector rotation as

$$V_r = U_x \cos(\theta) + U_y \sin(\theta),$$

$$W = -U_x \sin(\theta) + U_y \cos(\theta),$$

where $\theta = \arctan(y/x)$. The wall-normal velocity V is defined as positive away from the wall as $V = -V_r$. The instantaneous velocities are denoted by capital letters and the fluctuating velocities are in lower cases. The velocity gradients are obtained in the wavenumber space during the simulation, which are transformed to the physical space by inverse Fourier transformation.

The pipe length is $30R$ for all the four Reynolds numbers studied, which is chosen to be longer than the maximum wavelength of VLSMs and superstructures reported for pipes (Eggels et al. (1994); Morrison et al. (2004); Guala et al. (2006); Hutchins and Marusic (2007b); Monty et al. (2007); Wu and Moin (2008); Wu et al. (2012); Baltzer et al. (2013)). In SEM, each hexahedral element in the computational domain is refined by Gauss-Lobatto-Legendre (GLL) nodes with Lagrange polynomial order of N for the velocity field and $N - 2$ for the pressure field. This arrangement is known as $P_N - P_{N-2}$ (Maday and Patera (1989); El Khoury et al. (2013)). The computational mesh is unstructured on the cross-stream $(r-\theta)$ planes and uniform in the streamwise direction. Figure 3.1 shows the unstructured mesh on a cross-stream plane. The computational grids for different Reynolds numbers

Re_D	Re_τ	Elements	Grid points	Δx^+	Δr^+	$R\Delta\theta^+$
5300	180	49248	25.2×10^6	[3.03, 9.93]	[0.14, 4.36]	[1.52, 4.96]
11700	360	350208	179×10^6	[3.02, 9.99]	[0.16, 4.07]	[1.52, 4.94]
17000	500	832728	426×10^6	[3.05, 9.95]	[0.16, 4.24]	[1.48, 4.83]
37700	1000	6089952	3.12×10^9	[3.00, 9.99]	[0.16, 4.31]	[1.53 ,4.75]

Table 3.1: DNS parameters and spatial resolution of the present turbulent pipe flow at different Reynolds numbers.

are shown in quarters. The element boundaries are highlighted in red. The mesh in $3D$ is shown in figure 3.2 for the lowest Reynolds number. The GLL points in polynomial distribution inside each element is clearly visible. The grid is refined near the wall and is the finest when nearest to the wall. The parameters of the spatial discretisation of the pipe at different Reynolds numbers are shown in table 3.1. The grid resolution is shown in wall units as Δx^+, Δr^+ and $R\Delta\theta^+$. A grid independence test for the computational mesh of the pipe using different order or GLL nodes was reported by Wang (2017) where the cross-stream mesh is adopted from. The $2D$ cross-stream mesh of the pipe at each Reynolds number has been used in the DNS performed in the research group of turbulent flow in straight pipes, bend pipes (Wang (2017), Wang et al. (2018)) and round jets (Dunstan (2020)). The present DNS of pipe flow at $Re_\tau = 1000$ is one of the largest simulations performed using Nek5000 and on the UK national supercomputing system, ARCHER. The simulation is by far the largest case performed in the research group which has over three billion computational grid points and requires over 10^4 processors. For such petascale simulations, a preconditioner, i.e., an algebraic multigrid (AMG) solver is applied once at the initial stage of the simulation to speed up and improve the scalability of the simulation.

Transformation of the DNS data from the original unstructured mesh to structured uniform mesh is required for data post-processing in order to produce turbulence statistics. The data are remapped on a uniform polar mesh when computing turbulent statistics, for instance, probability density functions.

3.2 Vector and tensor transformation

For pipe flows, the solutions of the Navier-Stokes equations in the Cartesian coordinates often require transformation to the cylindrical coordinates. The vectors (e.g., velocity) are transformed by a transformation matrix B as $V_{(r,\theta,z)} = BV_{(x,y,z)}$ for a

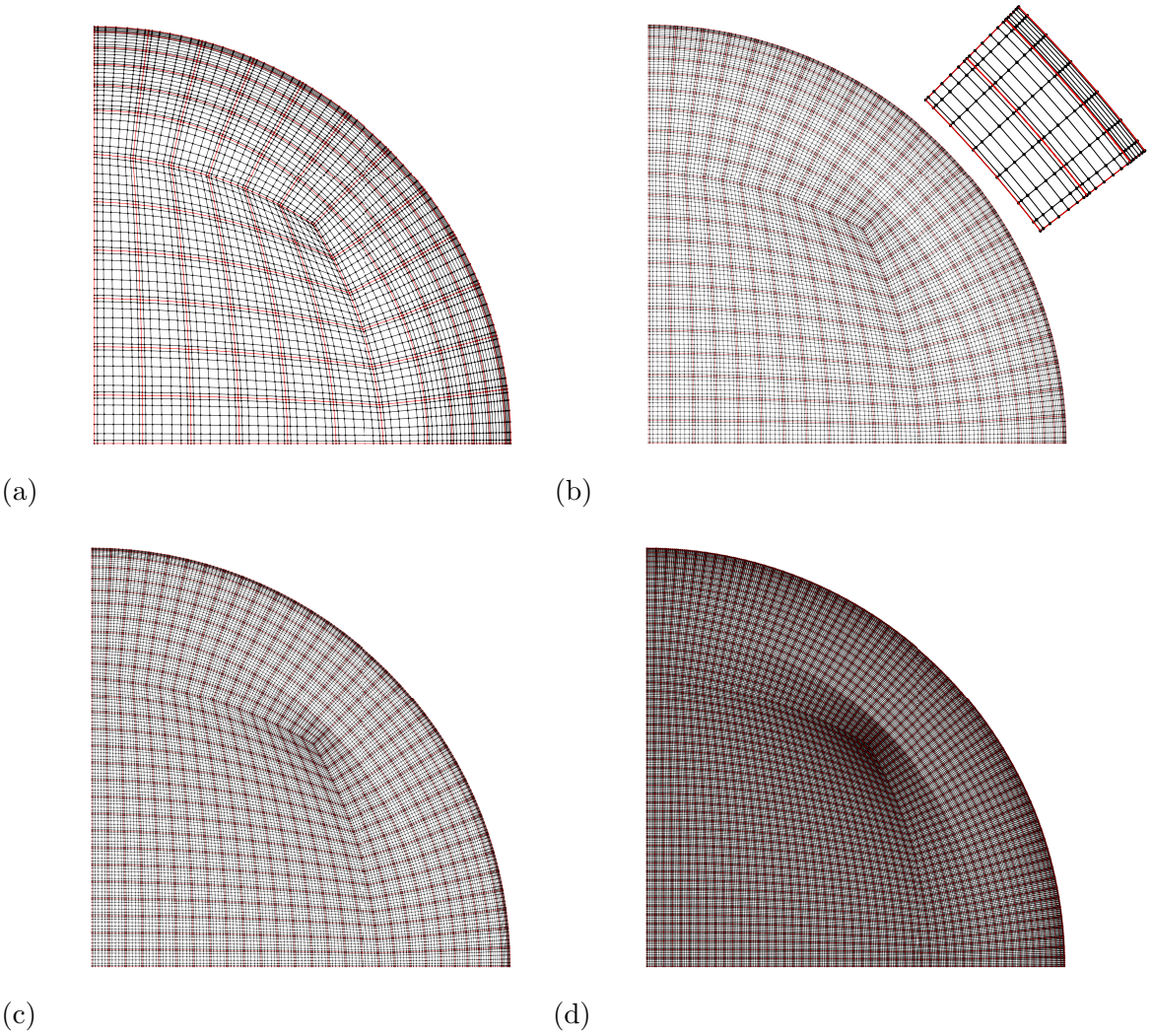

Figure 3.1: Cross-stream $(r-\theta)$ view of the computational mesh for simulation at (a) $Re_\tau = 180$, (b) $Re_\tau = 360$, (c) $Re_\tau = 500$ and (d) $Re_\tau = 1000$.

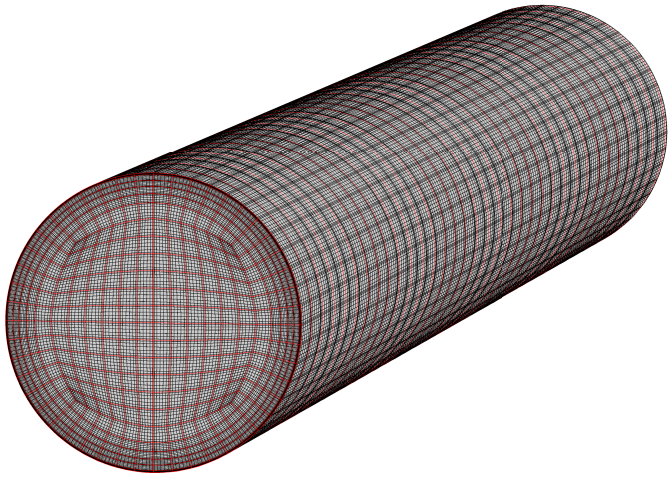

Figure 3.2: $3D$ view of the computational mesh of one-third of the pipe for simulation at $Re_\tau = 180$.

vector V:

$$\begin{bmatrix} v_r \\ v_\theta \\ v_z \end{bmatrix} = \begin{bmatrix} \cos(\theta) & \sin(\theta) & 0 \\ -\sin(\theta) & \cos(\theta) & 0 \\ 0 & 0 & 1 \end{bmatrix} \begin{bmatrix} v_x \\ v_y \\ v_z \end{bmatrix}. \tag{3.3}$$

The tensors (e.g., S_{ij}, Ω_{ij}) are transformed using the same transformation matrix as $A_{(r,\theta,z)} = BA_{(x,y,z)}B^{-1}$ for a tensor A:

$$\begin{bmatrix} s_{rr} & s_{r\theta} & s_{rz} \\ s_{\theta r} & s_{\theta\theta} & s_{\theta z} \\ s_{zr} & s_{z\theta} & s_{zz} \end{bmatrix} = \begin{bmatrix} \cos(\theta) & \sin(\theta) & 0 \\ -\sin(\theta) & \cos(\theta) & 0 \\ 0 & 0 & 1 \end{bmatrix} \begin{bmatrix} s_{xx} & s_{xy} & s_{xz} \\ s_{yx} & s_{yy} & s_{yz} \\ s_{zx} & s_{zy} & s_{zz} \end{bmatrix} \begin{bmatrix} \cos(-\theta) & \sin(-\theta) & 0 \\ -\sin(-\theta) & \cos(-\theta) & 0 \\ 0 & 0 & 1 \end{bmatrix}. \tag{3.4}$$

3.3 Proper orthogonal decomposition

Proper orthogonal decomposition (POD) is a linear modal decomposition technique (Berkooz et al. (1993)) which was shown to be effective in extracting coherent activities with large energy contribution in turbulent flows (Buxton et al. (2017)). In this study, $2D$ snapshot POD is applied as follows.

A velocity field with M total spatial data points and N available snapshots

forms a snapshots matrix $\mathbf{V}$ with rank $(2M \times N)$ where

$$\mathbf{V} = \left[\mathbf{u}^1, \mathbf{u}^2 \cdots \mathbf{u}^N\right] = \begin{bmatrix} u_1^1 & u_1^2 & \cdots & u_1^N \\ u_2^1 & u_2^2 & \cdots & u_2^N \\ \vdots & \vdots & \vdots & \vdots \\ u_M^1 & u_M^2 & \cdots & u_M^N \\ v_1^1 & v_1^2 & \cdots & v_1^N \\ \vdots & \vdots & \vdots & \vdots \\ v_M^1 & v_M^2 & \cdots & v_M^N \end{bmatrix}. \tag{3.5}$$

The auto-covariance matrix $\mathbf{C} = \mathbf{V}^T\mathbf{V}$ with rank $(N \times N)$ is solved for its eigenvalues and eigenvectors from $\mathbf{CA} = \lambda\mathbf{A}$. The eigenvectors $\mathbf{A}(N \times N)$ and the eigenvalues $\lambda(1 \times N)$ are sorted for a descending order of $\lambda_1 > \lambda_2 > \cdots > \lambda_N$.
The N POD modes in $\mathbf{\Phi} = \left[\phi_1, \phi_2, \cdots, \phi_N\right]$ are calculated as

$$\phi_i = \frac{\mathbf{VA}_i}{\left\|\mathbf{VA}_i\right\|}, \qquad i = 1, 2, \cdots, N,$$

where the rank of $\mathbf{\Phi}$ is $(N \times N)$.

The POD mode coefficient $\mathbf{a}$ is calculated as

$$\mathbf{a} = \mathbf{\Phi}^T\mathbf{U}.$$

The original snapshot can be reconstructed from using all modes as

$$\mathbf{U} = \mathbf{\Phi a}.$$

A snapshot can also be reconstructed from using a collection of selected modes, $\hat{\mathbf{\Phi}}$ as

$$\hat{\mathbf{U}} = \hat{\mathbf{\Phi}}\hat{\boldsymbol{a}}.$$

Chapter 4

DNS of turbulent pipe flow

This chapter investigates viscous Newtonian fluid flows in a straight circular pipe. DNS is performed at four Reynolds numbers, Re_τ = 180, 360, 500 and 1000 with computational parameters shown in table 3.1. The Navier-Stokes equations are solved in the non-dimensional form. Equations 3.1 and 3.2 are non-dimensionalised by a characteristic length, i.e., the pipe radius R, and a characteristic speed, i.e., the bulk mean velocity U_b. For incompressible Newtonian fluids, equation 3.2 is solved as

$$\frac{\partial u_i}{\partial t} + u_j \frac{\partial u_i}{\partial x_j} = -\frac{\partial p}{\partial x_i} + \frac{1}{Re} \frac{\partial^2 u_i}{\partial x_j^2} \tag{4.1}$$

where the Reynolds number $Re = \rho U_b R/\mu$.

In this chapter, the instantaneous fields and the turbulence statistics are represented first to evaluate the quality of the DNS data. The turbulence statistics are compared with historical DNS data of the pipe from the literature. The main body of this chapter investigates the large-scale coherent structure, i.e., the uniform-momentum zones (UMZ) and the internal shear layers (ISL) in the pipe. Three UMZ/ISL identification methods are used, which are each placed in a separate subsection with the characteristics of the UMZs and ISLs identified by each of the identification methods.

4.1 Instantaneous fields of velocity and vorticity

The circular contours in figure 4.1 show the instantaneous streamwise velocity U and the streamwise fluctuation u in a cross-stream plane for the four Reynolds numbers. The scale increase from the wall to the pipe centre at each Reynolds number is clear. The contours in the right-hand-side column are plotted on wall-parallel $(x-\theta)$ planes at $y^+ \approx 10$. The increasingly more complex flow and wider range of scales at higher

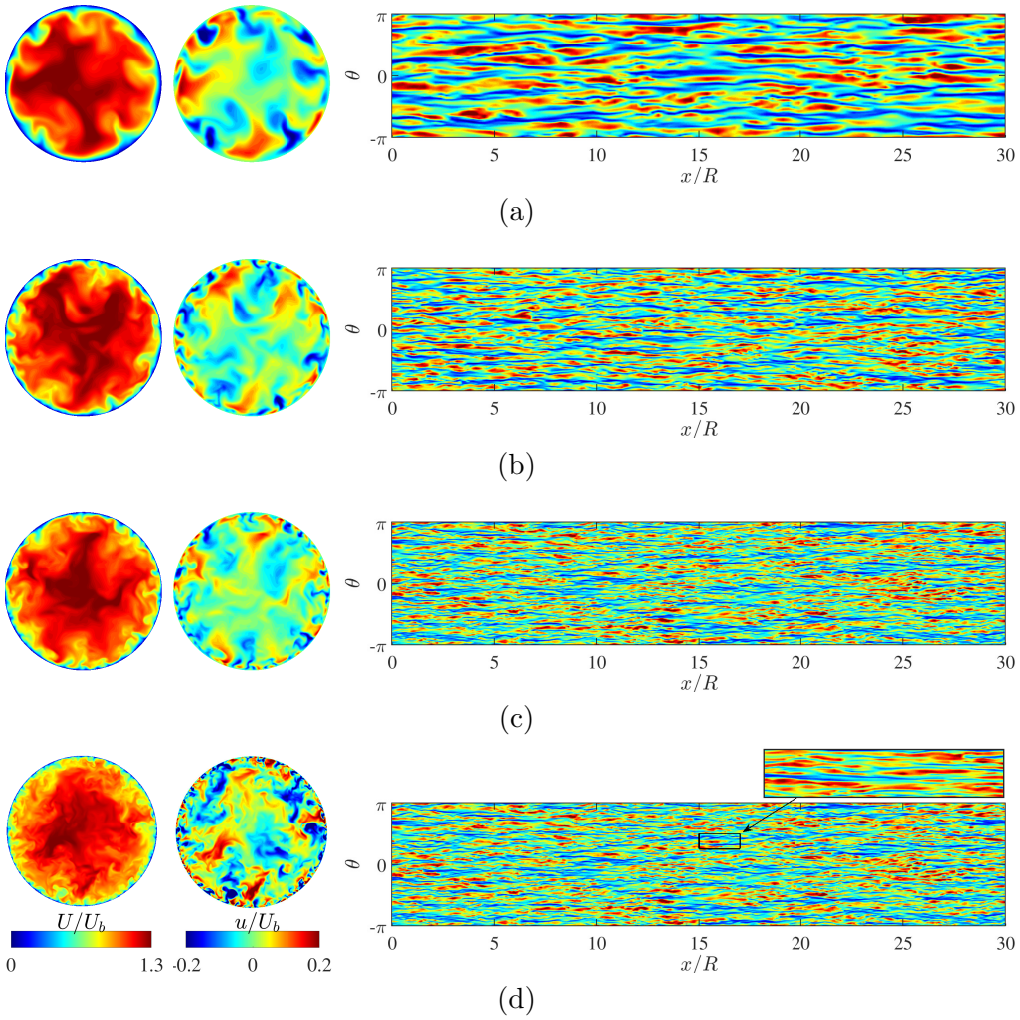

Figure 4.1: Contours of the instantaneous streamwise velocity U (the left column) and streamwise fluctuation u (the middle and the right columns) for the pipe flow at (a) Re_τ = 180, Re_τ = 360, Re_τ = 500 and Re_τ = 1000.

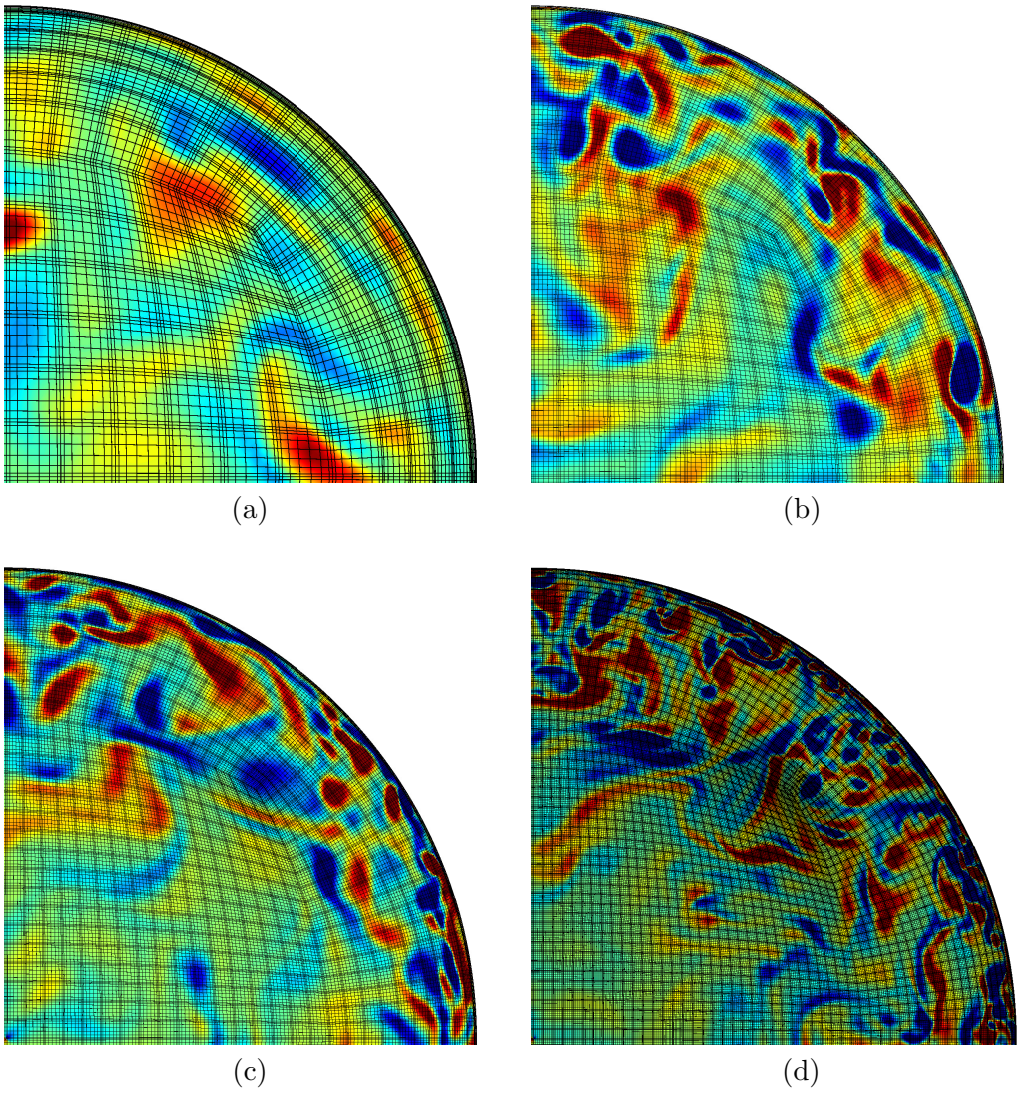

Figure 4.2: Cross-stream contours of the instantaneous streamwise vorticity ω_x for (a) Re_τ = 180, (b) Re_τ = 360, (c) Re_τ = 500 and (d) Re_τ = 1000. The contours are shown in quarters, overlaid with the computational grids shown in figure 3.1.

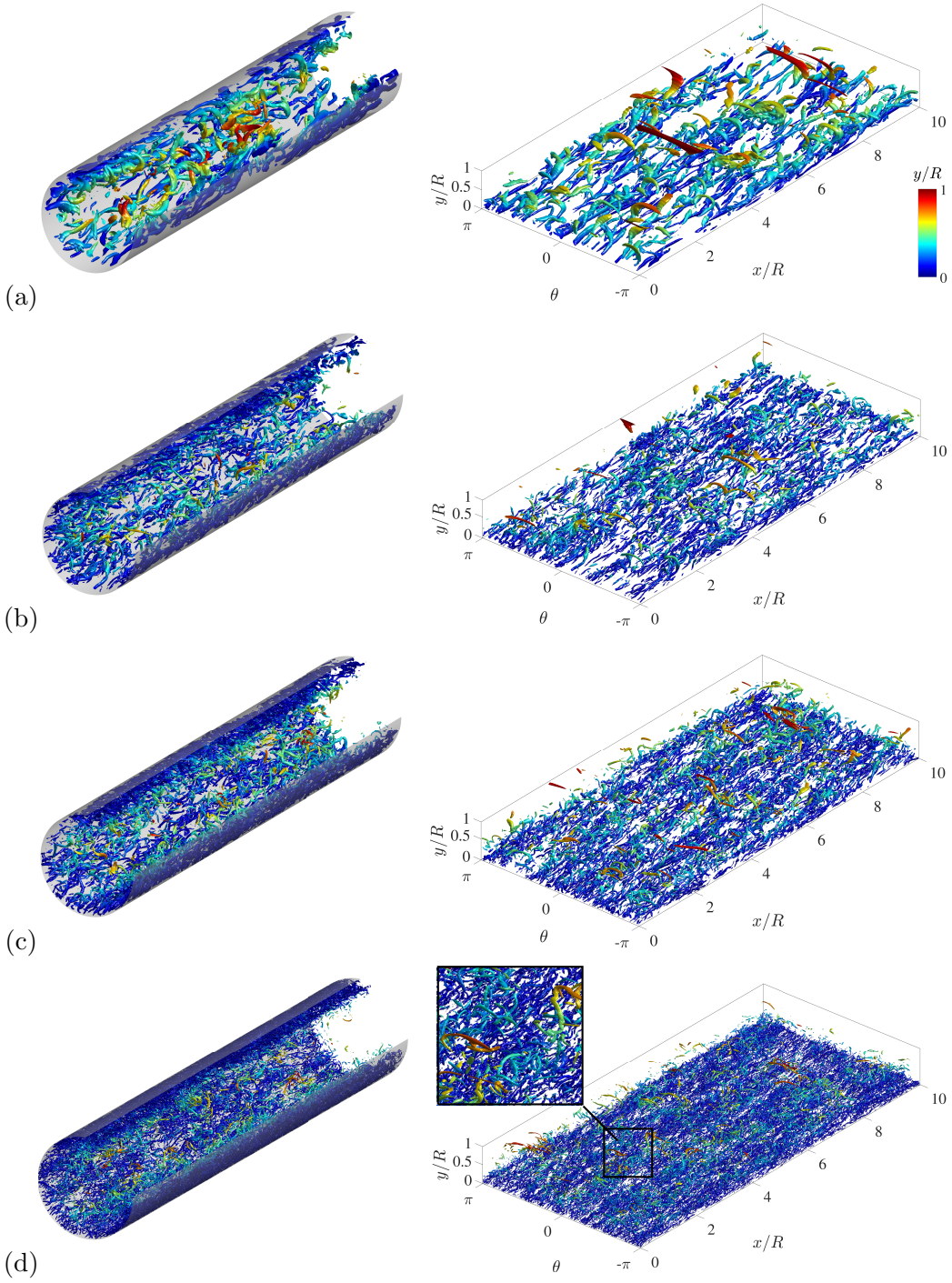

Figure 4.3: Iso-surfaces of Q for (a) Re_τ = 180, (b) Re_τ = 360, (c) Re_τ = 500 and (d) Re_τ = 1000. The iso-surfaces are shown in the first 1/3 of the streamwise domain. The pipe is unwrapped in the right column.

Reynolds numbers are apparent, especially in the near-wall region. The pattern of the streamwise elongated high- and low-speed streaks near the wall are clear. The average spanwise spacing between the adjacent high- or low-speed streaks near the wall is approximately 100 wall units, which implies there should be roughly 11, 23, 31 and 63 high-speed streaks at Re_τ = 180, 360, 500 and 1000, respectively in figure 4.1.

Figure 4.2 shows the contours of the streamwise vorticity ω_x for each Reynolds number with their spectral element grid. It is clear that the vortical structures are stronger nearer the wall. The small-scale counter-rotating vortices in figure 2.2 appear next to the wall. These vortices are significantly smaller at high Reynolds number, confined in a closer vicinity of the wall. The overlaid mesh provides a visual evaluation on the grid resolution. The vortical structures which scale with the Reynolds number, are well-resolved. There is no visible discontinuity in ω_x from spatial discretisation. The three-dimensional view of the vortical structures is shown by $Q-$criterion in figure 4.3. The iso-surfaces of Q show the densely populated quasi-streamwise vortical structures near the wall. The decrease in the smallest structure scale is apparent. The vortical structures become more complex as Reynolds number increases. The well-defined and smooth worm-like vortical structures indicate that the present DNS of the pipe flows is sufficiently resolved at all four Reynolds numbers.

4.2 Mean flow statistics

The profile of the mean streamwise velocity at the four Reynolds numbers are shown in figure 4.4(a). In the viscous sublayer ($y^+ < 5$), all the profiles of the inner-scaled $\overline{U}$ collapse to the linear part of the law of the wall, $U^+ = y^+$. Away from the wall ($y^+ > 20$), $\overline{U}$ no longer scales with the wall unit, the profiles of U^+ at different Reynolds numbers do not collapse. It is clear that the profiles of U^+ show better agreement with the log-law at higher Reynolds numbers. The logarithmic region is not observed at the lowest Reynolds number Re_τ = 180; U^+ deviates from the log-law, $U^+ = \kappa^{-1} ln(y^+) + B$ substantially, which have been reported as the low-Reynolds number effect on the turbulence statistics by Eggels et al. (1994) in the pipe, Moser et al. (1999) and Antonia and Kim (1994) in the channel. Very far from the wall, the deviation of the profiles from the log-law with an increase in $\overline{U}$ indicates the wake region in the pipe centre.

The inner-scaled root-mean-square (RMS) velocities are shown in figures 4.4(b-d). The profiles of u_{rms} and v_{rms} collapse well with the inner scaling in the

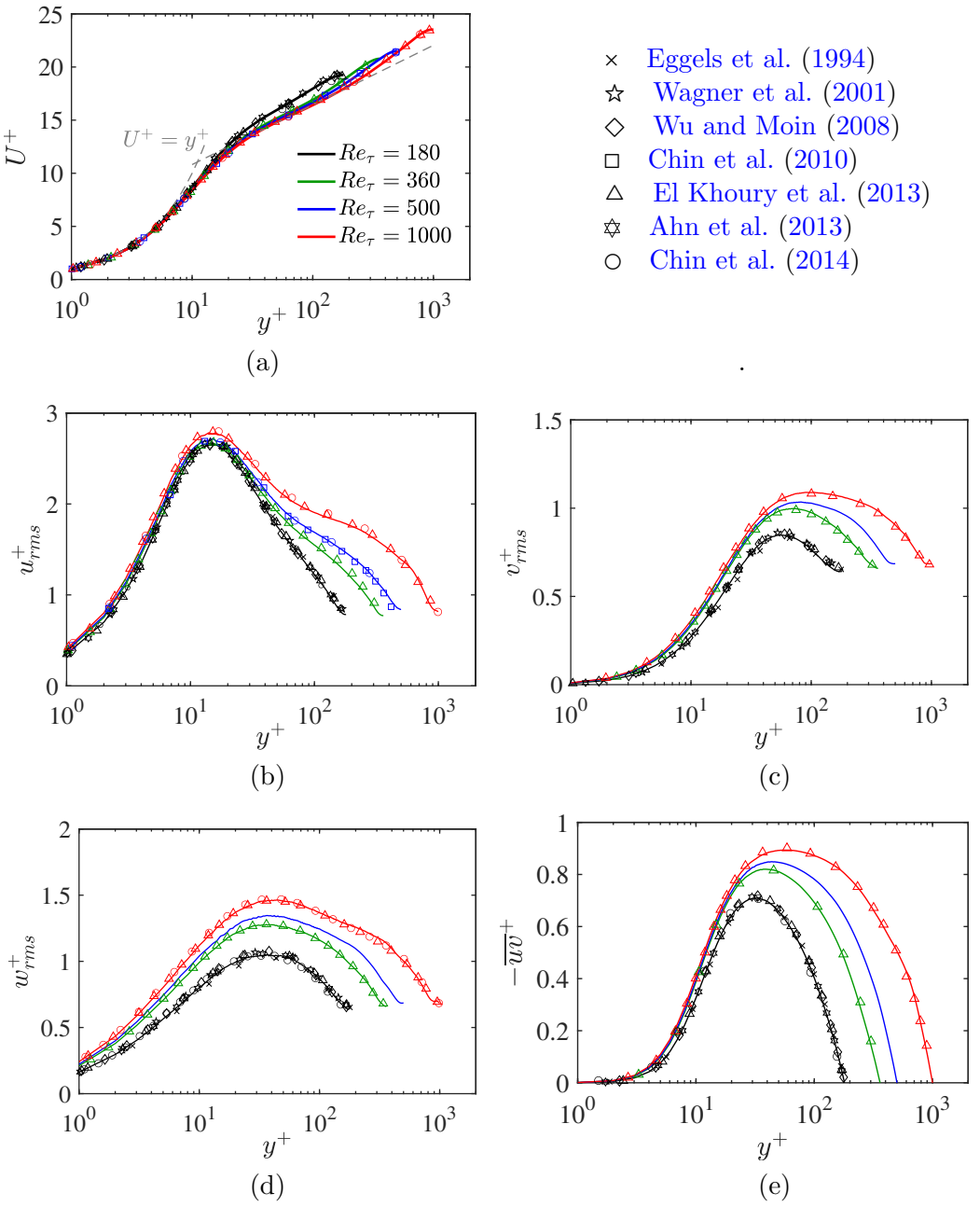

Figure 4.4: (a) Mean streamwise velocity profile, $\overline{U}$. The log-law, $U^+ = \kappa^{-1} ln(y^+) + B$ ('– – –') is plotted for $\kappa = 0.41$ and $B = 5.2$. Root-mean-square velocity fluctuations in (b) the streamwise direction, u_{rms}, (c) the wall-normal direction, v_{rms}, and (d) the azimuthal direction, w_{rms}. (e) The mean Reynolds shear stress $-uv$. The DNS results from the literature are overlaid by symbols.

viscous sublayer whereas they start to separate for $y^+ > 20$. The peaks of u_{rms} and v_{rms} increase with the Reynolds number. The maximum of u_{rms} is roughly located at $y^+ = 15$ as was found by Moser et al. (1999); Abe et al. (2001); Hutchins et al. (2009); Monty et al. (2009); Jiménez et al. (2010); El Khoury et al. (2013) and Chin et al. (2014). The increase in maximum u_{rms} is believed to be induced by the fast-travelling large-scale structures, leaving their footprints in an increasingly closer proximity to the wall at higher Reynolds numbers (del Álamo and Jiménez (2003); El Khoury et al. (2013)).

The maximum of RMS velocity in the wall-normal direction, v_{rms} shows a much more substantial increase with Re_τ than u_{rms}. The location of the maximum of v_{rms} shift away from the wall as Re_τ increases, and is further away from the wall than the location of maximum u_{rms} at each Reynolds number. In figure 4.4(d), the profiles of the RMS velocity in the azimuthal direction, w_{rms} clearly does not hold with inner scaling, where substantial discrepancies are found even in the near-wall region. Similar to v_{rms}, the location of maximum w_{rms} show Reynolds number dependence which moves further away from the wall with increasing Reynolds number (Buschmann et al. (2009)). The non-vanishing Reynolds stress term, uv, is shown in figure 4.4(e). The Reynolds shear stress $-uv$ is responsible for momentum transport in wall turbulence. The profiles of $-\overline{uv}$ is similar to u_{rms} and v_{rms} in terms of inner scaling, which collapse well for $y^+ < 10$. The profiles of $-\overline{uv}$ show a clear low-Reynolds number effect at $Re_\tau = 180$. The profile of $-\overline{uv}$ at $Re_\tau = 180$ deviates from the profiles at higher Reynolds numbers which overlap in the viscous sublayer.

Turbulent statistics are compared with the DNS results from the literature which are listed in table 4.1. The present data shows an excellent agreement with the previous DNS of the pipe. The data is used in the study of coherent structures, i.e., the uniform-momentum zones (UMZ) and the internal shear layers (ISL) in turbulent pipe flows.

Publication	Re_D	Re_τ	Numerical method	L/R	Δx^+	Δr^+	$R\Delta\theta^+$
Eggels et al. (1994)	5300	180	2^{nd}-order FVM	10	7.03	[0.94, 1.88]	8.84
Wagner et al. (2001)	5300	180	2^{nd}-order FVM	10	3.70	[0.36, 4.32]	4.70
Wu and Moin (2008)	5300	180	2^{nd}-order FDM	15	5.31	[0.17, 1.65]	2.22
Chin et al. (2010)	17000	500	2^{nd}-order SEM	$\pi \sim 20\pi$	6.8	[0.07, 5.50]	8.20
El Khoury et al. (2013)	5300	180	3^{rd}-order SEM	25	[3.03, 9.91]	[0.14, 4.44]	[1.51, 4.93]
	11700	360			[3.03, 9.91]	[0.16, 4.70]	[1.49, 4.93]
	37700	1000			[2.01, 9.98]	[0.15, 5.12]	[0.98, 4.87]
Ahn et al. (2013)	5300	180	2^{nd}-order FDM	30	5.25	[0.17, 1.63]	2.20
Chin et al. (2014)	5000	180	2^{nd}-order SEM	20π	6.70	[0.50, 3.60]	8.40
	17000	500		8π	6.80	[0.07, 5.50]	8.20
	37600	1000		8π	7.87	[0.60, 7.30]	6.56
present study	5300	180	3^{rd}-order SEM	30	[3.03, 9.93]	[0.14, 4.36]	[1.52, 4.96]
	11700	360			[3.02, 9.99]	[0.16, 4.07]	[1.52, 4.94]
	17000	500			[3.05, 9.95]	[0.16, 4.24]	[1.48, 4.83]
	37700	1000			[3.00, 9.99]	[0.16, 4.31]	[1.53, 4.75]

Table 4.1: Parameters of DNS compared with the present study in the literature for turbulent pipe flow from Re_τ = 180 to 1000.

4.3 The quiescent core of the pipe

In this section, the quiescent core in the pipe is investigated using the DNS data of a single Reynolds number at $Re_\tau = 500$. The quiescent core region in channels is bounded by two ISLs: an upper and a lower interface defined at a single velocity threshold U_κ. In pipe, the core is bounded by a continuous boundary, circumferentially enclosed in the azimuthal direction.

The results in this section were previously published in Chen et al. (2019b).

4.3.1 Identification of the quiescent core

The quiescent core of the pipe is identified by using the *double-PDF* method (table 2.2) following Kwon et al. (2014) and Yang et al. (2016). Numerous instantaneous PDFs of the streamwise velocity U are computed from a subdomain with streamwise window size of $\mathcal{L}_x/R = 0.2$ in all the snapshots. The PDFs are sampled from a uniform cylindrical grid because for pipe, the uniform polar mesh on the circular cross-stream $(r-\theta)$ planes is more equivalent to the channel and TBL which have uniform grids in the Cartesian coordinates, i.e., the sampling is uniform in the wall-parallel and wall-normal directions regardless of the coordinate system.

Figure 4.5(a) shows an example of the instantaneous PDF of U in the $3D$ subdomain. 110 bins are used in the PDF of $U/U_{CL} \in [0, 1.1]$ with a bin width $\mathcal{B} = 1\%$ of U_{CL}. The peaks on the PDF are detected using a constrained peak detection scheme following Laskari et al. (2018). Three constraints are applied in the detection scheme: (i) a minimum distance between two adjacent peaks, $F_d = 3\%$ of U_{CL} so that two peaks being too close to each other are seen to be spurious and treated as one local UMZ, (ii) a minimum height of peaks, $F_h = 0.5\%$ so that peaks with a bin count less than 0.5% of the total count are ignored, and (iii) a minimum prominence of the peak, $F_p = 25\%$ which requires a recognised peak to be 25% higher than the average bin count of its neighbouring bins. On the PDF in figure 4.5(a), there are three recognised peaks, i.e., three local UMZs travelling at three modal velocities, U_m under the constrained peak detection scheme. These three local UMZs are shown on the cross-stream contour of U in figure 4.5(d) by the thin blue contours defined at velocity thresholds marked by '▲'. The modal velocities of the local UMZs at the peaks on each instantaneous PDF are collected from all available snapshots.

A secondary PDF is computed for all the collected U_m, shown in figure 4.5(b). The PDF distribution is very similar to the DNS results by Kwon et al. (2014) and Yang et al. (2016). The dominant peak marked by '▼' indicates the

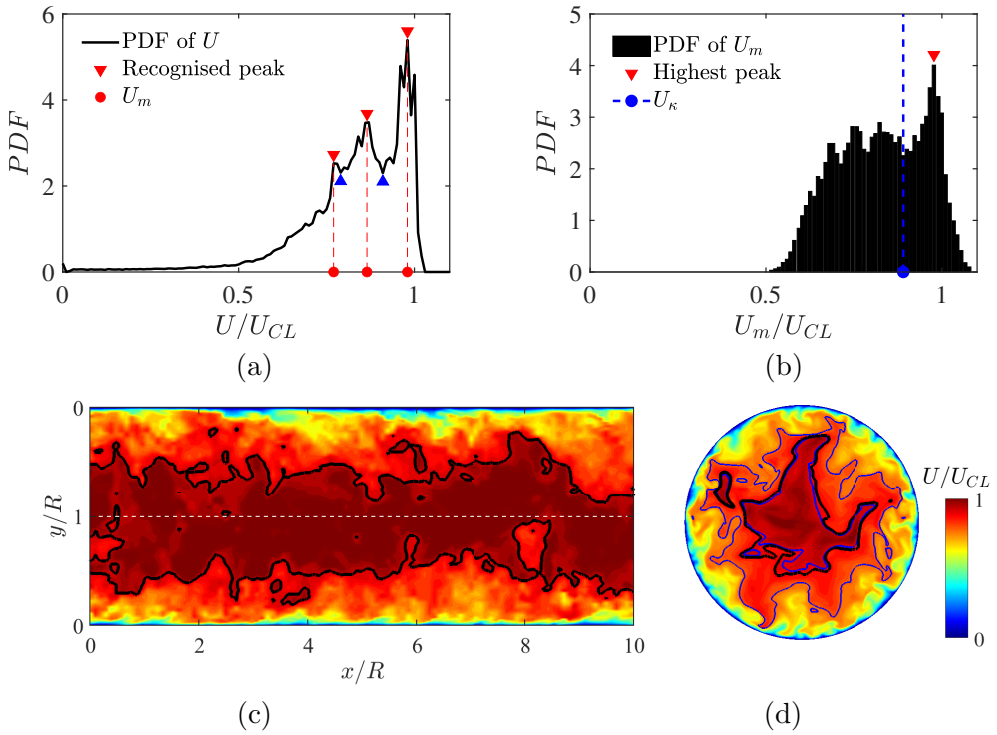

Figure 4.5: (a) PDF of the instantaneous streamwise velocity, U, constructed using the $3D$ subdomain with a streamwise length of $\mathcal{L}_x = 0.2R$ from a snapshot. The recognised peaks from the peak detection scheme are marked by '▼', which indicate local UMZs with modal velocity U_m. (b) PDF of the modal velocities U_m collected from all the PDF of U in all subdomains from all available snapshots over time. The threshold velocity U_κ for the quiescent core is marked by the blue dashed line. (c,d) Coloured contours of U from the same snapshot used in (a), on (c) a streamwise-wall-normal (x–y) plane and (d) the cross-stream (r–θ) plane within the subdomain where the PDF in (a) was computed from. The white dashed line in (c) indicates the pipe centreline. The thick black contours in (c,d) indicate the quiescent core boundary defined by $U_\kappa/U_{CL} = 0.9$. The two blue contours in (d) show the local UMZs defined at threshold velocities marked by '▲' in (a).

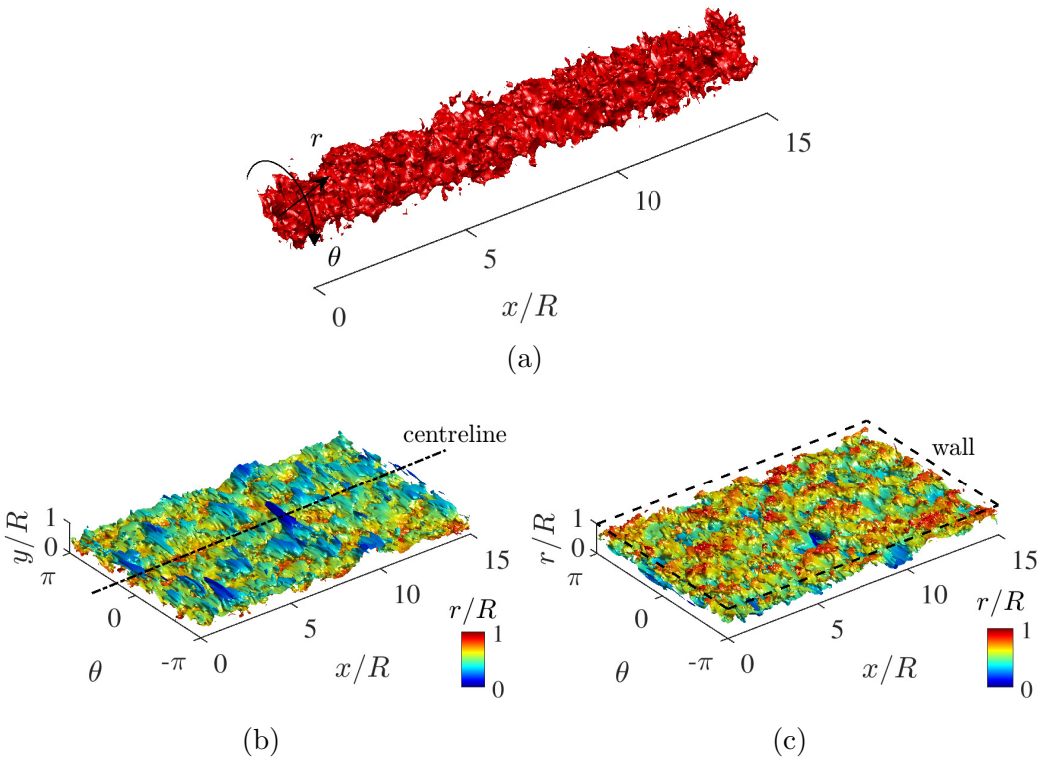

Figure 4.6: Visualisation of the quiescent core in $3D$: (a) iso-surface of the streamwise velocity at U/U_{CL} = 0.9. The core is unwrapped to a sheet by mapped to the cylindrical coordinates in (b,c). (b) shows the side of the core interface facing the wall and (c) shows the core interface facing the pipe centreline. The interfaces in (b,c) are coloured by the radial extent of the interface, so that the bulges and the valleys in figure 2.4 are in blue and red, respectively.

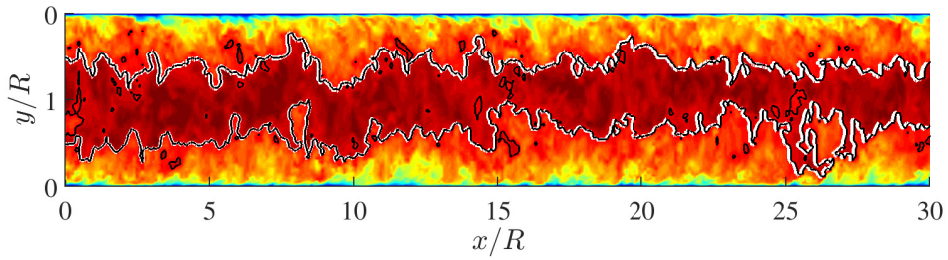

Figure 4.7: The quiescent core as contour of the streamwise velocity at U/U_{CL} = 0.9 (black) and the quiescent core after eliminating the islands outside the main enclosed core region.

most likely modal velocity for the quiescent core region in the pipe. In other words, the appearance of local UMZs travelling at this velocity is the most frequent. On this secondary PDF of U_m, the less-dominant peaks were seen as spurious peaks by Kwon et al. (2014). The core boundary is defined by a threshold velocity U_κ at the local maximum between the dominant peak and its adjacent peak as marked by '●'. The PDF of U_m suggests that $U_\kappa \approx 0.9U_{CL}$ in the pipe at $Re_\tau = 500$.

The quiescent core is enclosed by the continuous core boundary shown by the black contour of $U/U_{CL} = 0.9$ in figures 4.5(c,d). The pipe core shows similar thinning, thickening, and wall-normal meandering behaviours to the cores in channels. The $3D$ view of the core is shown in figure 4.6 for a half of the streamwise computational domain. The core is very contorted in $3D$ which shows large-scale streaky features in figures 4.6(b,c). The core is unwrapped by transforming to the cylindrical coordinates. The core interface is shown with the sides facing the pipe centreline and facing the wall, respectively. The interface is coloured by the radial location of the iso-surface, so that the bulges and valleys on the interface are indicated by blue and red, respectively, similar to figure 2.4. The blue bulges are caused by lower-speed fluid ejected up from the wall, and the red valleys are caused by the faster-speed fluid sweep closer to the wall.

The small islands outside the main core region with $U/U_{CL} \geq U_\kappa$ and inside the main core with $U/U_{CL} < U_\kappa$ are ignored in Kwon et al. (2014) via inner enveloping. Similarly, in order to define the core boundary as continuous ISL, these islands are eliminated in this study by removing enclosed contours of significantly shortened length. As figure 4.7 shows, the islands are excluded in the continuous core boundary highlighted in white.

4.3.2 Meandering and intermittency of the core

The meandering with the thinning of the quiescent core can cause the core to approach significantly close to the wall and leaves the pipe centreline outside (Kwon et al. (2014)). The chance of the core leaving the centreline outside was measured by an intermittency factor $\gamma(y)$ by Kwon et al. (2014) in the channel, similar to the intermittency of turbulent/non-turbulent interface (TNTI) in TBL. γ as a function of wall-normal location is the proportion of time a wall-normal location is left outside the core. A higher γ indicates less chance for a wall-normal location to be included inside the core.

Figure 4.8 shows γ of the quiescent core of the pipe. The results by Kwon et al. (2014) for a channel core defined at a higher U_κ at $0.95U_{CL}$ are overlaid. γ for a pipe core defined at an arbitrary velocity at $U_\kappa = 0.95U_{CL}$ is plotted for comparison.

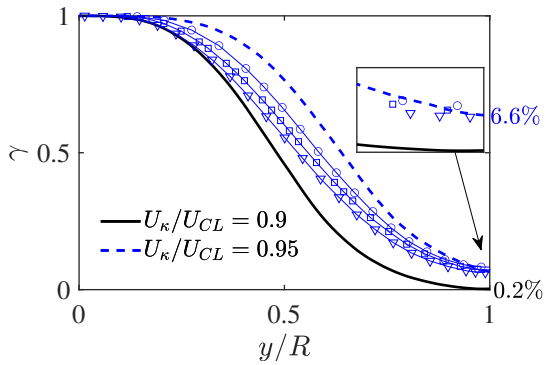

Figure 4.8: The quiescent core intermittency, γ at different wall-distance. The results from Kwon et al. (2014) for a quiescent core defined at U_κ/U_{CL} = 0.95 in TBL at $Re_\tau \approx 1000$ ('○'), 2000 ('□') and 4000 ('▽') are shown.

The profiles of γ exhibit similar trend and always have $\gamma = 1$ at the pipe wall which is never bounded inside the core. The profiles of the channel show a dependence on the Reynolds number, the profiles shift to the left so that more flows stay in the core when Reynolds number increases. This corresponds to that the cores defined at a fixed velocity threshold are thicker at higher Reynolds number because the location of $\overline{U}$ reaching a certain U_κ is closer to the wall at a higher Reynolds number. At the centreline, $\gamma > 0$ indicates that the quiescent core can leave the centreline outside as observed. By comparing the centreline intermittency (γ at $y/R = 1$) of the cores in the channel and pipe at two different velocity thresholds, the centreline intermittency mostly depends on U_κ rather than Reynolds number or the geometry. The cores defined at $U_\kappa/U_{CL} = 0.95$ spend approximately 6.6% of the time away from the centreline for channels at $Re_\tau = 1000$ to 4000 and for the present pipe flow at $Re_\tau = 500$. The quiescent core of the pipe defined at $U_\kappa/U_{CL} = 0.9$ spends only 0.2% of the time excluding the centreline because it is naturally thicker. A core defined at any arbitrary velocity threshold lower than this would have $\gamma = 0$ at the pipe centreline.

4.3.3 Conditional average properties across the core boundary

Conditional averaged streamwise velocity U and azimuthal vorticity $\Omega_\theta = \partial V/\partial x - \partial U/\partial r$ are computed around the quiescent core interface, as functions of the wall-normal distance from the core interface, ξ. The conditional averaged quantities are denoted as $\langle\cdot\rangle$. $\langle U\rangle$ and $\langle\Omega_\theta\rangle$ are computed in a region with a wall-normal span of $0.3R$, centring the core interface as shown in figure 4.9. Figure 4.12 shows the profiles of $\langle U\rangle$, velocity gradient of $\langle U\rangle$, and $\langle\Omega_\theta\rangle$ as functions of the wall-

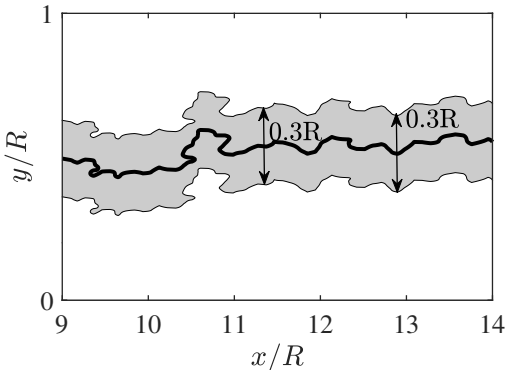

Figure 4.9: Illustration of the wall-normal span around the quiescent core interface for conditional averaging.

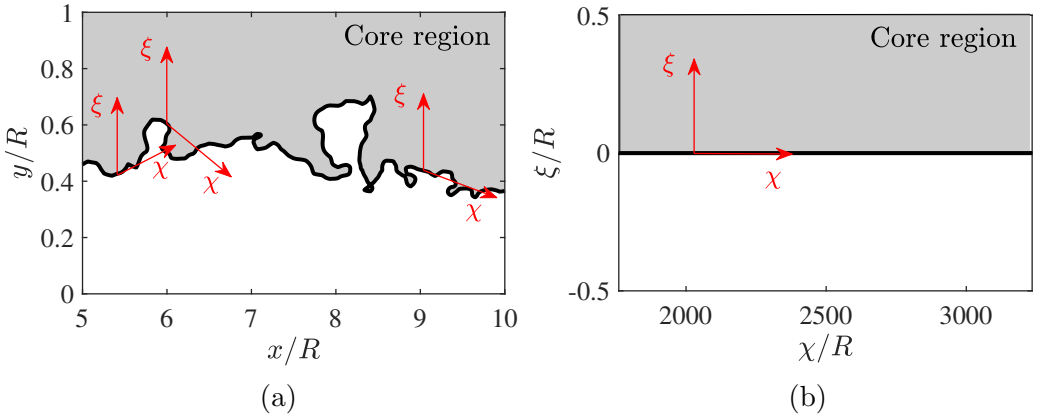

Figure 4.10: Schematic illustration of coordinate transformation from axial direction to the direction tangential to the interface used by the present study.

normal distance from the core interface, ξ. The conditional averaging is computed essentially by taking average in the tangential direction χ along the core interface, the transformation from x to χ is schematically shown in figure 4.10. The direction ξ is always normal to the wall. Another coordinates transformation for computing averages along a tortuous interface used in Kankanwadi and Buxton (2020) is shown in figure 4.11 where the $\chi - \xi$ axes are orthogonal and ξ is normal to the interface. In this study, we use the transformation in figure 4.10.

Figures 4.12(a) and (b) show the profiles of $\langle U \rangle$ across the interface. The dot-dashed lines at $\xi = 0$ are virtually the interface. The well-known streamwise velocity jump in the vicinity of the interface is clear. With positive ξ representing locations

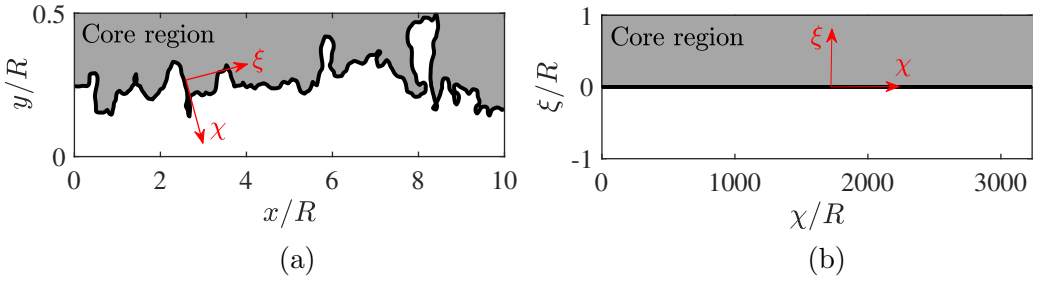

Figure 4.11: Schematic illustration of coordinates transformation from orthogonal axes to axes tangential and normal to the quiescent core interface by Kankanwadi and Buxton (2020).

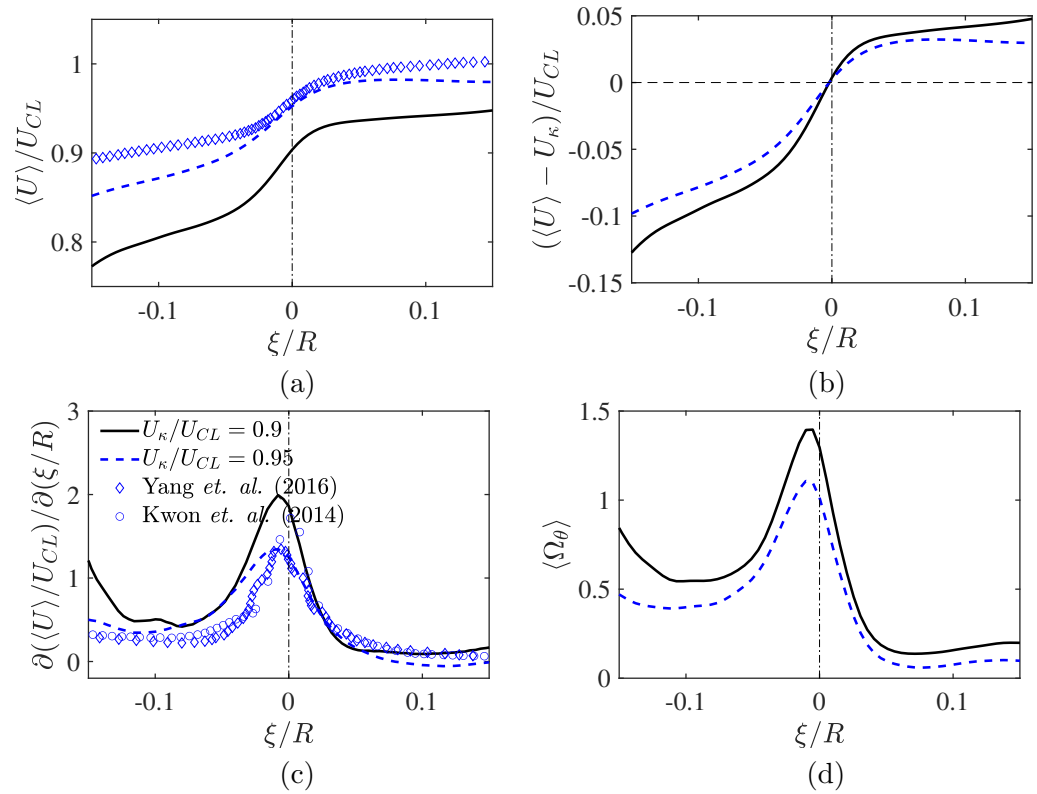

Figure 4.12: Conditional average of (a,b) the streamwise velocity U, (c) velocity gradient of U and (d) the azimuthal vorticity Ω_θ across the core interface as functions of the distance to the core boundary, xi. $\xi > 0$ indicates inside of the core region. Symbols are the results of the quiescent core defined at U_κ/U_{CL} = 0.95 in TBL at $Re_\tau \approx 1030$ by Kwon et al. (2014) and the channel at Re_τ = 930 by Yang et al. (2016).

inside the core, $\langle U \rangle$ exhibit a suddenly steeper increase across the interface and stays relatively constant in the core region. The cores defined at a higher velocity threshold of $U_\kappa/U_{CL} = 0.95$ in the present pipe and the channel by Yang et al. (2016) are overlaid with lines and symbols in blue. The quiescent cores defined at higher U_κ show smaller increases in U which is clearer in figure 4.12(b) with $\langle U \rangle - U_\kappa$. This should be expected because the core interface defined at a higher U_κ resides further away from the wall where velocity changes less abruptly. The profiles of the velocity gradient of $\langle U \rangle$ over ξ in figure 4.12(c) suggest consistent results. The peaks in $\partial\langle U \rangle/\partial\xi$ at the interface correspond to the step-like jump in $\langle U \rangle$. The peak of the cores defined at higher U_κ exhibit lower velocity gradients since velocity changes less abruptly across them.

The abrupt jumps of U across the interface lead to the peaks of azimuthal vorticity, Ω_θ around the interface in figure4.12(d). The profiles of $\langle \Omega_\theta \rangle$ reach a local maximum slightly before entering the core region and stay relatively low inside the core. The conditional averaged results in figure 4.12 paint a consistent picture of the large-scale structural distribution of the UMZs and ISLs in the pipe to the channel (Kwon et al. (2014); Yang et al. (2016)). The quiescent core of the pipe showed complex contortion in $3D$. The step-like jump in the streamwise velocity across the interface is associated with the concentrated vorticity along the core interface which is essentially an ISL.

4.4 Uniform-momentum zones

In this section, multiple UMZs and the UMZ interfaces (ISL) are investigated using the DNS data of the pipe at a single Reynolds number, Re_τ = 500. The first part of this section investigates the statistical characteristics of the UMZ and UMZ interfaces. The similarities and differences in different wall-bounded flows are discussed via comparison with the results of multiple UMZs in the TBL by de Silva et al. (2016, 2017). The second part of this section investigates the contortion of the UMZ interface in $3D$. The role of the spanwise vortices clustering along the UMZ interface (Adrian et al. (2000)) is investigated, and the coupled dynamics of the vortical structures and the ISLs are revealed. The footprints of the LSM (Rao et al. (1971); Metzger and Klewicki (2001); Jiménez et al. (2004)) on the near-wall cycle and the large-scale modulation of the near-wall bursting events by the LSM (Hutchins and Marusic (2007a,b); Marusic and Hutchins (2008); McKeon and Sharma (2010); Chung and McKeon (2010); Baars et al. (2017)) are investigated in the UMZ aspect. The asymmetry of the large-scale modulation (Agostini and Leschziner (2014, 2016)) is quantified.

The results in this section were previously published in Chen et al. (2020).

4.4.1 Identification of multiple UMZs

The identification of multiple UMZs in the pipe adopts the PDF method used by Adrian et al. (2000); de Silva et al. (2017) and Laskari et al. (2018). The identification of the local UMZs is very similar to the process discussed in section 4.3.1. The local UMZs are detected from the instantaneous PDFs of U with a bin size of $\mathcal{B}$ = 1%U_{CL}. Each PDF of U is computed from a $3D$ subdomain with streamwise window size of $\mathcal{L}_x/R$ = 0.2. The sampled data points are uniform in the cylindrical coordinates. Figure 4.13 shows an example of the UMZ detection which is very similar to figure 4.5. The PDF method collects all the local UMZs on each PDF of U instead of filtering them by a secondary PDF for the modal velocity U_m on the peaks. The peaks are detected by a similar constrained peak detection scheme used in section 4.3.1 following Laskari et al. (2018). The constrained peak detection scheme is composed of (i) a minimum distance between two adjacent peaks, $F_d = 3\%$ of U_{CL} so that spurious peaks being too close to each other are treated as one UMZ; (ii) a minimum height of peaks, F_h = 0.5% so that peaks with a bin count less than 0.5% of the total PDF bin count are ignored; and (iii) a minimum prominence of the peak, F_p = 25% which requires a recognised peak to be 25% higher than the average bin count of its neighbouring bins. In the snapshot used in figure 4.13, three local

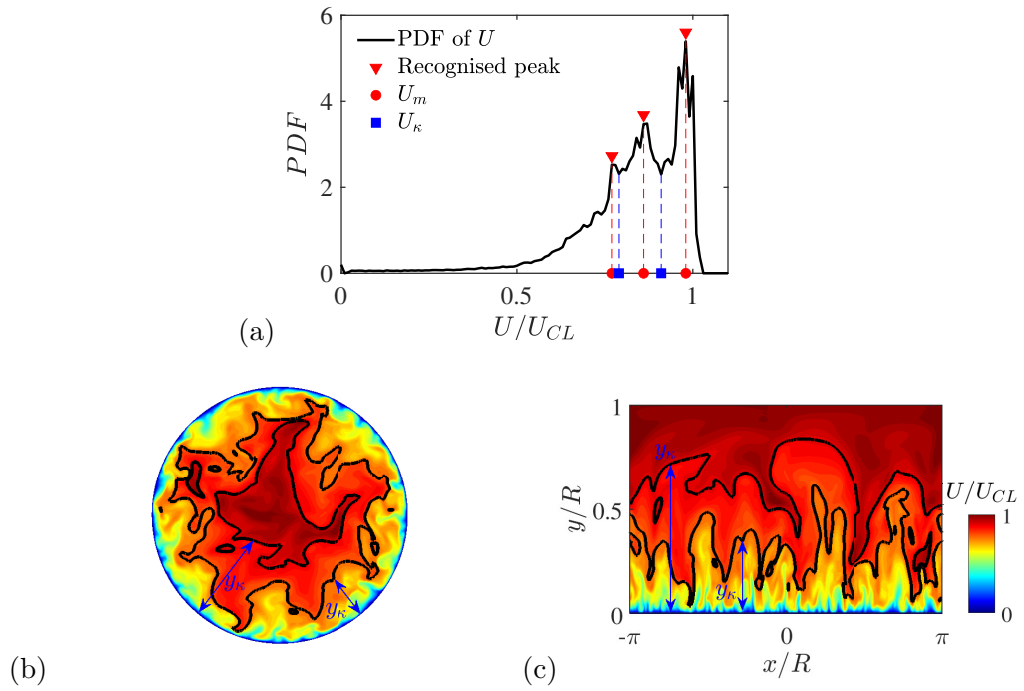

Figure 4.13: (a) PDF of the instantaneous streamwise velocity, U, constructed using the $3D$ subdomain with a streamwise length of $\mathcal{L}_x = 0.2R$ from a snapshot. The recognised peaks from the peak detection scheme are marked by '▼', which indicate local UMZs with modal velocity U_m. The velocity thresholds U_κ of the UMZ interfaces are marked by the '■' at the minimum bin between adjacent peaks. (b) Coloured contours of U from the same snapshot and subdomain used in the PDF in (a) on the cross-stream $(r-\theta)$ plane. The contour is also shown unwrapped in (c). The two contour lines are defined at U_κ and demarcate the three identified local UMZs.

UMZs ('▼') are identified by the peak detection scheme. Each of the local UMZs travels approximately at a modal velocity U_m ('●'), and are demarcated by two interfaces defined by velocity thresholds U_κ ('■') at the minimum bins between each two adjacent peaks on the PDF. The UMZs and UMZ interfaces are shown in the cross-stream contour of U. The two iso-contour defined at U_κ separate the three zones in the flow region. The UMZ and UMZ interfaces defined at lower thresholds are naturally closer to the wall.

As discussed in section 2.1.1, the number of UMZ detected on each PDF, N_{UMZ} is sensitive to the constraints applied in the peak detection. Stricter conditions will largely reduce N_{UMZ}. Laskari et al. (2018) adjusted their constraints with a targeting average $N_{UMZ} \approx 4.5$ estimated from the Reynolds number dependency of N_{UMZ} in TBL by de Silva et al. (2016). The trend suggests $N_{UMZ} \approx 2.5$ at $Re_\tau = 500$.

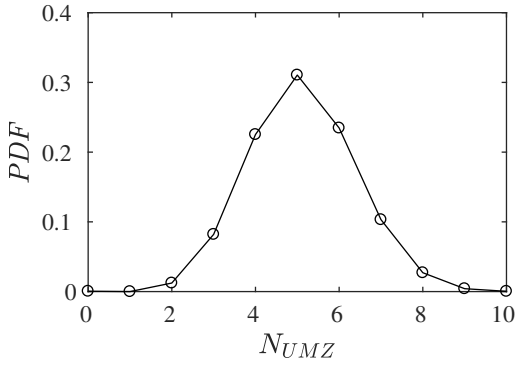

Figure 4.14: PDF of the number of UMZs identified on each instantaneous PDF of U.

This is found to be underestimating for the present pipe flow at $Re_\tau = 500$ because many well-distinct peaks are seen to be neglected. This suggests that for a TBL and a pipe flow at a similar Reynolds number, there are potentially more UMZs in the pipe due to the full circumferential wall confinement. Therefore, no targeting N_{UMZ} is pre-defined. The constraints are chosen only for a robust combination which preserves the well-defined peaks on the PDFs. Figure 4.14 shows the PDF of N_{UMZ} of all the PDFs of U using all available snapshots. The PDF is at its maximum at $N_{UMZ} = 5$, suggesting that there are five UMZs in the pipe flow at $Re_\tau = 500$ on average. The PDF agrees with the normal distribution found by de Silva et al. (2016) and Laskari et al. (2018), indicating that a sufficient number of instantaneous UMZs have been obtained for statistical analysis.

4.4.2 The grouping of UMZs

The local UMZs collected from all the snapshots are classified into a few groups based on their zone modal velocities U_m. The UMZs are grouped by the magnitude of U_m similar to de Silva et al. (2016, 2017). Six U_m groups denoted as M_i are defined by uniform ranges of U_m listed in table 4.2. The UMZs in group M_6 travelling at the lowest U_m on average are naturally the closest to the wall, and the UMZs in group M_1 with $U_m/U_{CL} \in [1.0, 1.1)$ are the innermost UMZs in the pipe, travelling above the centreline velocity. Figure 4.15 shows the PDF of the number of UMZs categorised in each U_m group. The distribution of N_{UMZ} in U_m groups follows the time-averaged PDF of U (dashed line). Group M_6 with the lowest modal velocity range has the lowest UMZ count, and group M_2 has the highest number of UMZ.

Group M_i	U_m/U_{CL}	Colour	Symbol
1	$[1.0, 1.1)$	blue	●
2	$[0.9, 1.0)$	red	▲
3	$[0.8, 0.9)$	green	■
4	$[0.7, 0.8)$	magenta	×
5	$[0.6, 0.7)$	cyan	◆
6	$[0.5, 0.6)$	yellow	◀

Table 4.2: The range of modal velocity U_m, symbols and colours for UMZ groups M_i grouped by U_m.

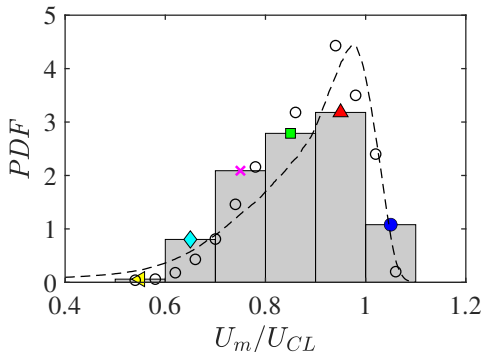

Figure 4.15: PDF of the number of UMZs categorised in each U_m group M_i (bars). The time-average PDF of the streamwise velocity U in the present pipe flow (– – –) and the PDF of U_m in TBL at $Re_\tau = 8000$ (○) by de Silva et al. (2016) are overlaid.

The number of UMZs travelling above the centreline velocity in group M_1 is also relatively low as expected. The distribution agrees well with the distribution of UMZ count in U_m groups in TBL by de Silva et al. (2016) shown by '○'.

4.4.3 The statistical characteristics of UMZ and UMZ interface

Wall-normal distribution of the UMZ and UMZ interfaces

Figures 4.16(a) and (b) show two UMZ interfaces at $U_m/U_{CL} \approx 0.9$ and 0.6, belonged in the highest-counting and the lowest-counting UMZ group, M_2 and M_6, respectively. The UMZ interface folds three-dimensionally due to the local ejection and sweep events around the interface. The group averaged interface wall-normal location for the UMZs in different U_m groups, $\langle y_\kappa \rangle$ is shown in figure 4.17. The angle brackets $\langle \cdot \rangle$ indicate averages of each group. For a given UMZ, its wall-normal location is defined from its lower-bounding interface to the wall, as illustrated in figure 4.13(b). In figure 4.17, the UMZs in group M_6 travelling at $U_m < 0.6U_{CL}$ are

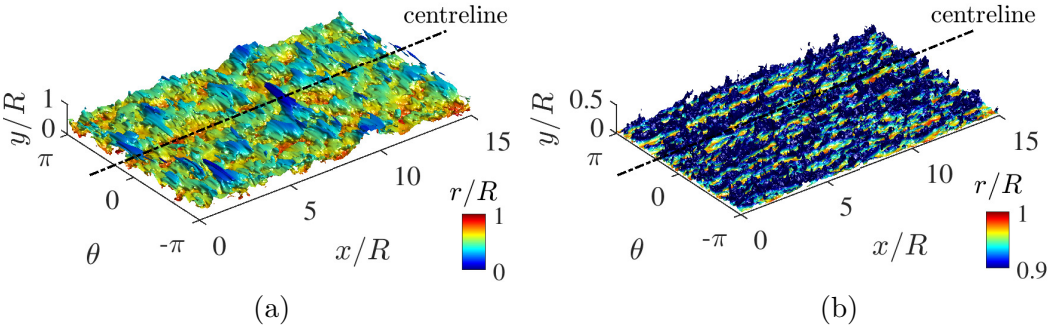

Figure 4.16: Visualisation of UMZ interfaces in $3D$: iso-surface of the instantaneous streamwise velocity at (a) U/U_{CL} = 0.9 and (b) U/U_{CL} = 0.59. The interfaces are unwrapped and show the side facing the pipe centreline. The interfaces are coloured by the radial extent of the interface, the bulges and the valleys in 2.4 are in blue and red, respectively.

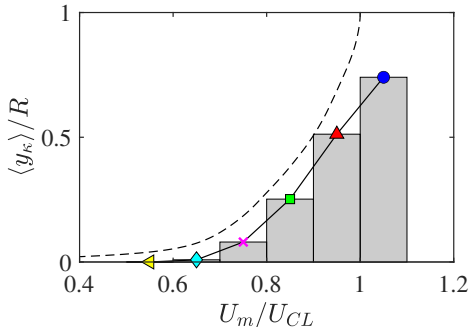

Figure 4.17: Group averaged UMZ interface wall-normal location, y_κ, for UMZs grouped by modal velocity U_m. The dashed line is the mean velocity profile of $\overline{U}$ in figure 4.4(a), plotted as $y(\overline{U})$.

very close to the wall with $\langle y_\kappa \rangle$ almost equal to zero. $\langle y_\kappa \rangle$ gradually increases from group M_6 to M_1, the trend of $\langle y_\kappa \rangle$ follows the mean profile of U plotted as $y(\overline{U})$. The non-linear increase of $\langle y_\kappa \rangle$ for UMZs departing away from the wall from group M_6 to M_1 indicates that the UMZs are more closely distributed nearer the wall, and the faster-travelling UMZs in groups $M_{1:3}$ are further apart from each other, being thicker. The results of $\langle y_\kappa \rangle$ indicate that the multiple UMZs in the pipe are not uniformly distributed in the wall-normal direction but in a hierarchical distribution where zones near the wall are more densely populated, similar to TBL (de Silva et al. (2016, 2017)).

Zonal mean velocity profiles inside and outside the UMZs

The zonal mean streamwise velocity and streamwise turbulent fluctuation are computed inside and outside the UMZs following Kwon et al. (2014). The zonal means inside a UMZ is averaged in the region between the centreline and the UMZ lower-bounding interface closer to the wall where its y_κ is measured from, in other words, over its radial extent from the pipe centre. The zonal means outside a UMZ is averaged over the region between its lower interface and the wall. Means inside the UMZ are denoted with a hat ($\widehat{U}$, $\widehat{u^2}$); means outside the UMZ are denoted with a tilde ($\widetilde{U}$, $\widetilde{u^2}$) similar to Kwon et al. (2014). Figure 4.18 shows the zonal means inside with dot-dashed lines and zonal means outside with dashed lines. The time-average profiles $\overline{U}$ and $\overline{u^2}$ (solid lines) are shown as references.

In figure 4.18(a), the zonal mean profiles of U inside and outside the UMZs in different U_m groups are plotted. The mean streamwise velocity inside the UMZ, $\widehat{U}$ is always higher than $\overline{U}$ whereas the mean outside the UMZ, $\widetilde{U}$ is always lower than $\overline{U}$. The profiles of $\widetilde{U}$ collapse with $\overline{U}$ in the near-wall region, and start to deviate from $\overline{U}$ away from the wall. This should be expected since in the concept of UMZ, the velocity develops in a step-like fashion from the wall to the pipe centre and most of the velocity changes happen across very thin spans (ISL) in the wall-normal direction. Therefore, the velocity difference between $\widehat{U}$ and $\widetilde{U}$ for each U_m group indicates the average velocity jump across the UMZ interfaces which will be quantified in later analyses. $\widehat{U}$ data is available in a large range of wall-normal locations, which can extend very close to the wall at $y/R \approx 0.01$ for group M_5. This well illustrates the large meandering nature of the UMZs. To measure the meandering of the UMZs in terms of how far they can reach close to the wall in extreme cases, figure 4.18(b) shows the minimum wall-normal location, $\widehat{y}$ where the UMZ can extend, in other words, where $\widehat{U}$ is last available near the wall. $\widehat{y}$ increases steadily for UMZs near the wall to the pipe centre, from $\widehat{y}/R \approx 0.01$ to 0.05 from group M_5 to M_2, whereas the innermost UMZs in group M_1, travelling beyond U_{CL} with $\widehat{y}/R \approx 0.22$ is significantly less close to the wall.

Figures 4.18(c,d) show the zonal mean profiles of U and u^2 for UMZs in group M_2 only. The results are compared to a single UMZ, namely the quiescent core in the channel defined at $U_\kappa/U_{CL} = 0.95$ by Kwon et al. (2014). In figure 4.18(c), $\widehat{U}$ in the pipe can extend further towards the wall due to the grouping: the profile is averaged with other UMZs in group M_2, defined at lower U_κ than the channel core, naturally being closer to the wall. The differences between the pipe profiles and the channel profiles are mainly caused by the difference in $\overline{U}$ due to the Reynolds number difference. Higher Reynolds number of the channel ($Re_\tau = 1000$) has $\overline{U}$

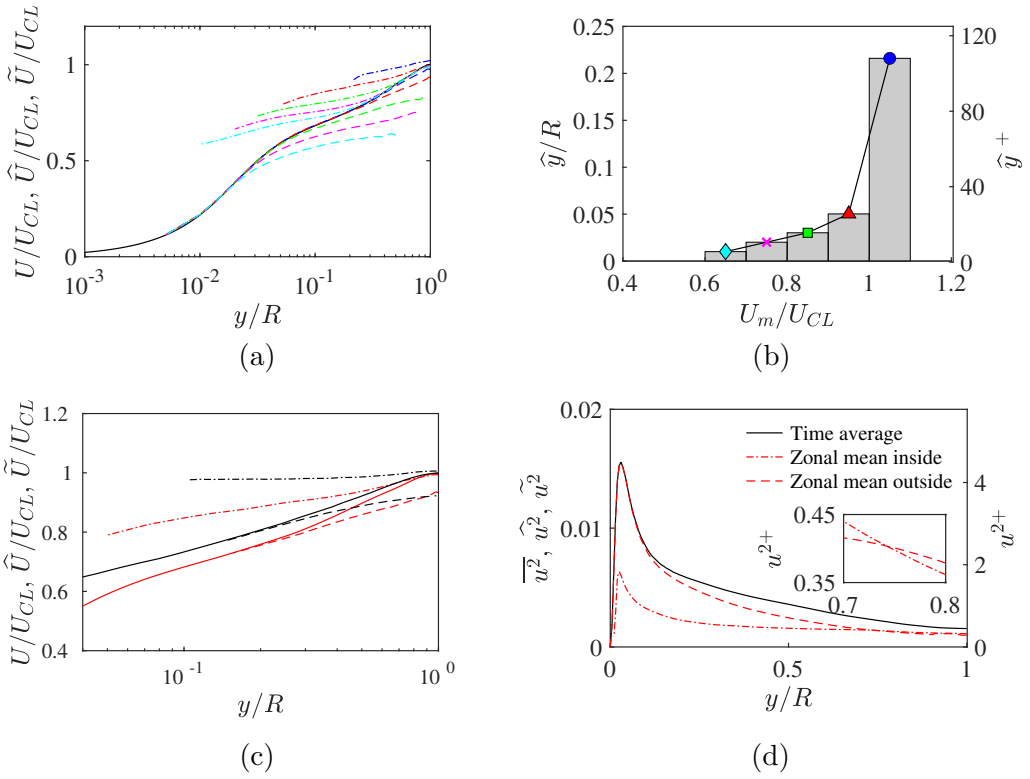

Figure 4.18: Profiles of zonal averaged streamwise velocity U for UMZs in different U_m groups: (a) groups $M_{1:5}$ with colours defined in table 4.2 and (c) group M_2 (red), overlaid with channel flow results by Kwon et al. (2014) (black). (b) The wall-normal location of the most near-wall data of zonal mean U of each U_m group in (a), $\widehat{y}$ (Symbols as in table 4.2). (d) The zonal mean streamwise fluctuation u^2 for group M_2 only. The solid lines (——) in (a,c,d) are the time-average U and u^2. The dot-dashed lines (– · –) are the zonal means inside the UMZ, $\widehat{U}$ and $\widehat{u^2}$; the dashed lines (– – –) are the zonal means outside the UMZ, $\widetilde{U}$ and $\widetilde{u^2}$.

developing faster nearer the wall. Otherwise, the trend between $\widehat{U}$, $\widetilde{U}$ and $\overline{U}$ is very similar in pipe and channel.

Figure 4.18(d) shows the zonal mean streamwise fluctuation u^2, which is computed relative to zonal means of U as in equation (4.2) following Kwon et al. (2014).

$$\widehat{u^2} = (U - \widehat{U})^2, \widetilde{u^2} = (U - \widetilde{U})^2 \tag{4.2}$$

The turbulent intensity inside the UMZ, $\widehat{u^2}$, is much lower than the turbulent intensity outside the zone, $\widetilde{u^2}$. The difference between $\widehat{u^2}$ and $\widetilde{u^2}$ becomes smaller towards the centreline. $\widehat{u^2}$ and $\widetilde{u^2}$ cross over at $y/R \approx 0.74$ where $\widehat{u^2}$ starts to be larger than $\widetilde{u^2}$ until the centreline (see the zoomed subset in figure 4.18(d)). A similar behaviour of $\widehat{u^2}$ and $\widetilde{u^2}$ was reported for the channel by Kwon et al. (2014), the crossover point for $\widetilde{u^2} > \widehat{u^2}$ was also found at $y/h \approx 0.74$ (h is the channel half height). Therefore, despite the Reynolds number effect, the quiescent core of channel and the UMZs of the pipe in group M_2 are very similar.

Conditional averages across the UMZ interface

Conditional averaged flow properties are computed across the UMZ interfaces as functions of the distance from the interface, ξ, similar to figure 4.12 in section 4.3.3. Figure 4.19(a) shows the group average streamwise velocity $\langle U \rangle$ against ξ for a single U_m group, M_2, overlaid with channel flow results by Yang et al. (2016). The angle brackets $\langle \cdot \rangle$ in this section indicate conditional averaging across the interface for UMZs in a U_m group with respect to ξ. $\xi > 0$ represents regions inside the radial extent of the UMZ. In figure 4.19(a), the abrupt jump in $\langle U \rangle$ across the UMZ interface is similar between UMZs in group M_2 and the quiescent core boundary in the channel: before entering the zone from the wall ($\xi < 0$), $\langle U \rangle$ develops fairly slow until the near vicinity of the interface where $\langle U \rangle$ exhibits a sharp change in the rate. The velocity gradient $\partial \langle U \rangle / \partial \xi$ for group M_2 is shown in figure 4.19(c), overlaid with the channel flow results by Kwon et al. (2014) and Yang et al. (2016). A local maximum of velocity gradient at the interface corresponds to the abrupt jump in $\langle U \rangle$.

Figures 4.19(e,f) show the streamwise fluctuation u^2 across the UMZ interface. In figure 4.19(e), the profiles of u^2 of the present pipe flow and the channel core of are very similar, the streamwise fluctuation decreases dramatically when passing the interface from the wall where the fluctuation level is high; u^2 reaches a local minimum approximately at the interface, and then remains much lower inside the UMZ. In figure 4.19(f), the u^2 profiles for groups M_3 and M_4 are noticeably different

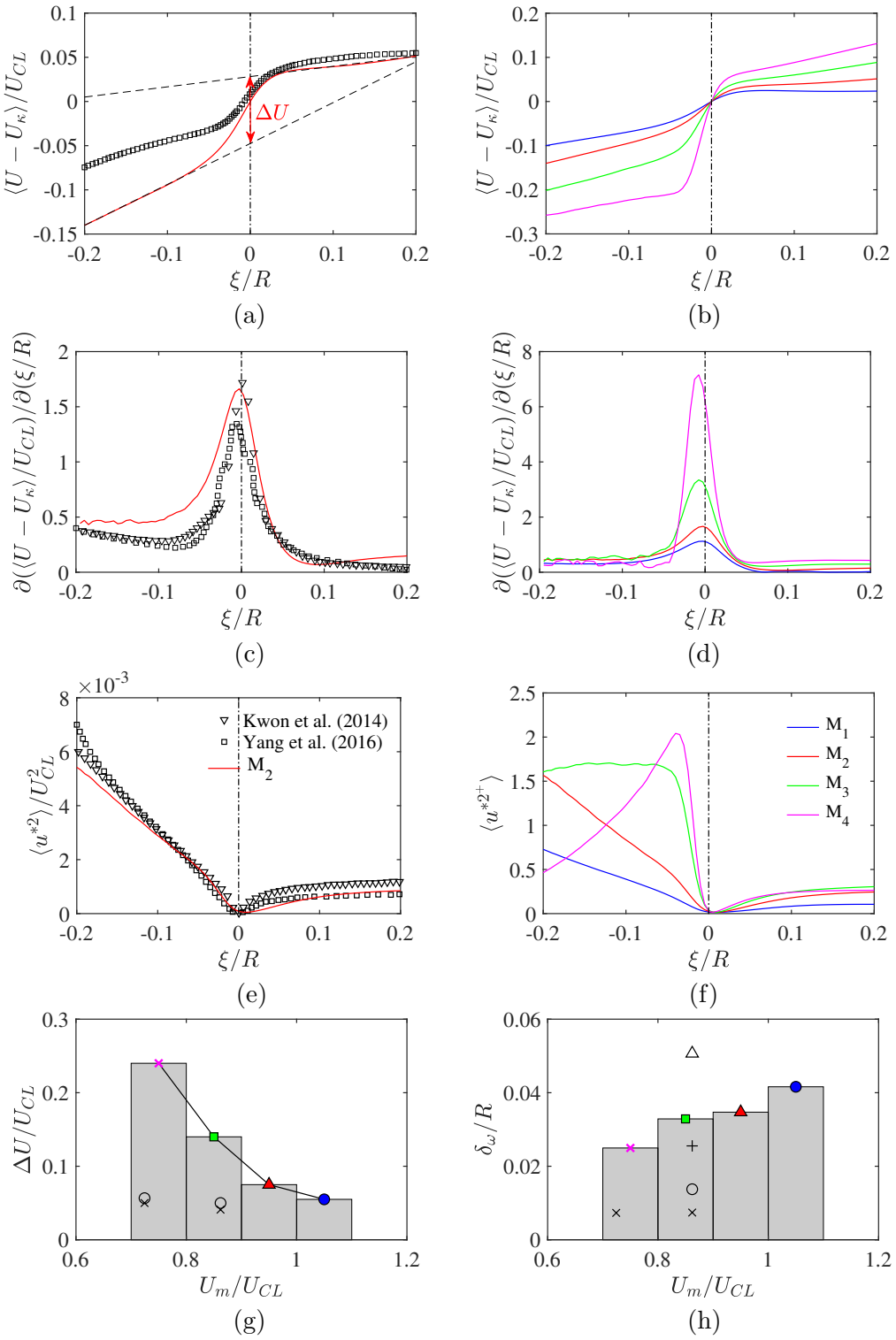

Figure 4.19: Conditional averages as functions of the distance from the lower-bounding UMZ interface, ξ for (a) the streamwise velocity U for U_m group M_2, (b) U for groups $M_{1:4}$, (c) velocity gradient $\partial U/\partial\xi$ for group M_2, (d) $\partial U/\partial\xi$ for groups $M_{1:4}$, (e) streamwise fluctuation u^{*2} for group M_2, and (f) u^{*2} for groups $M_{1:4}$. The legends in (e) and (f) apply to (a,c,e) and (b,d,f), respectively. (g) The magnitude of velocity jump in U across the UMZ interface, ΔU for groups $M_{1:4}$. (h) The UMZ interface thickness δ_ω calculated from equation (3.1) for groups $M_{1:4}$. (g,h) are overlaid with TBL results by de Silva et al. (2017) at Re_τ = 14500 (×), Re_τ = 8000 (○), Re_τ = 2800 (+) and Re_τ = 1200 (△).

from groups M_1 and M_2. This is because that the UMZs in groups $M_{3,4}$ are much closer to the wall (see figure 4.17), close enough to capture the rapid increase of $\overline{u^2}$ in the near-wall region.

Figure 4.19(b) shows $\langle U \rangle$ against ξ for U_m groups $M_{1:4}$. The increase in U across the UMZ interface is larger (higher magnitude) and more abrupt (higher velocity gradient) for interfaces closer to the wall as found in TBL by de Silva et al. (2017). Figure 4.19(d) corresponds to figure 4.19(b), showing the increase in the maximum velocity gradient at the interface for the slower-travelling UMZs residing closer to the wall. The magnitude of the velocity jump across the UMZ interfaces, ΔU is defined similarly as in Yang et al. (2016), and is illustrated in figure 4.19(a). The average ΔU for UMZs in each group is shown in figure 4.19(g) together with the TBL results by de Silva et al. (2017) at Re_τ = 8000 and 14500. ΔU in both pipe and TBL are found to be larger for UMZs travelling at lower U_m nearer the wall. It is clear that ΔU in pipe is significantly larger than TBL. This maybe partly caused by the lower Reynolds number in pipe: the number of UMZs is generally lower at lower Reynolds number so that U jumps across fewer interfaces with larger ΔU to achieve the centreline velocity. The increase in ΔU with decreasing Reynolds number is shown by the TBL results where the Re_τ = 8000 case ('○') has higher ΔU than Re_τ = 14500 ('×'). However, this increase in ΔU with lowering Reynolds number is not as significant as the difference in ΔU between pipe and TBL.

In figures 4.19(a-d), the sharp velocity jumps and the peaked velocity gradients at the UMZ interface take place over a visibly small distance over ξ, indicating that the UMZ interfaces themselves have a thickness as reported by de Silva et al. (2017). The thickness of the interfaces is estimated by

$$\delta_\omega = \frac{\Delta\langle U \rangle}{\partial\langle U \rangle / \partial y \,|_{max}} \tag{4.3}$$

following Kwon et al. (2014) and de Silva et al. (2017). Figure 4.19(h) shows the group average UMZ interface thickness δ_ω. δ_ω is lower for UMZs closer to the wall as found in TBL, so that the thinner UMZs nearer the wall are also bounded by thinner interfaces, which are accompanied with sharper and larger jumps of U. The UMZ interfaces being thinner nearer the wall is consistent to de Silva et al. (2017). The hierarchical distribution of UMZs, UMZ interfaces, and ΔU together suggest a discrete step-like instantaneous velocity profile in wall-bounded flows, which was used as an initial velocity profile in the modelling of a TBL by Bautista et al. (2019)

The overlaid TBL results of δ_ω at $Re_\tau = 1200 - 14500$ is comparable to group M_3 of the pipe. The interface thickness in TBL increases when Re_τ decreases as

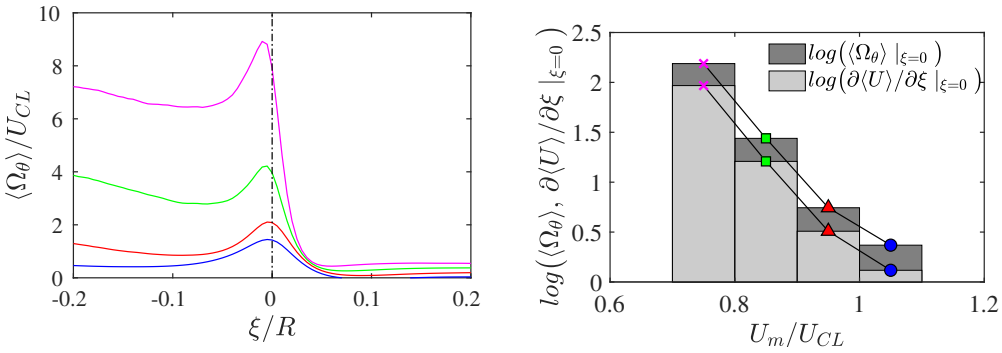

Figure 4.20: (a) Conditionally averaged azimuthal vorticity Ω_θ as functions to the distance from the lower-bounding UMZ interface, ξ for U_m groups $M_{1:4}$. (b) The local maximum Ω_θ in (a) and the local maximum $\partial U/\partial\xi$ in figure 4.19(d) at the UMZ interface ($\xi \approx 0$).

expected since there are less UMZs in larger scales at lower Reynolds numbers. The UMZ interface in pipe at a much lower Reynolds number, $Re_\tau = 500$, has δ_ω laid between the $Re_\tau = 1200$ and 2800 cases of TBL, indicating that the UMZ interfaces are, on average, thinner in pipe than TBL. This supports the results of ΔU where the velocity jump in U was found stronger in pipe. The UMZ interfaces are found to be thinner in the DNS data of pipe than the experimental data of TBL which may due to the limited spatial resolution in the experiments.

Figure 4.20(a) shows the conditional average of the azimuthal vorticity, $\langle\Omega_\theta\rangle$ against ξ. $\langle\Omega_\theta\rangle$ peaks at the proximity of the interface similar to $\partial\langle U\rangle/\partial\xi$ in figure 4.19(d). The magnitude of $\langle\Omega_\theta\rangle$ away from the interface at $\xi/R = -0.2$ is increasingly higher for the groups of UMZs residing closer to the wall because vorticities are stronger nearer the wall. The local maximum of $\langle\Omega_\theta\rangle$ at $\xi = 0$ in figure 4.20(a) and $\partial\langle U\rangle/\partial\xi$ in figure 4.19(d) are plotted in figure 4.20(b). The peak azimuthal vorticity and streamwise velocity gradient exhibit very similar trends: $\langle\Omega_\theta\rangle$ and $\partial\langle U\rangle/\partial\xi$ at the interface decrease almost log-linearly from the wall (M_4) towards the centre (M_2), though the innermost UMZs in group M_1 show a slightly lowered rate of decrease.

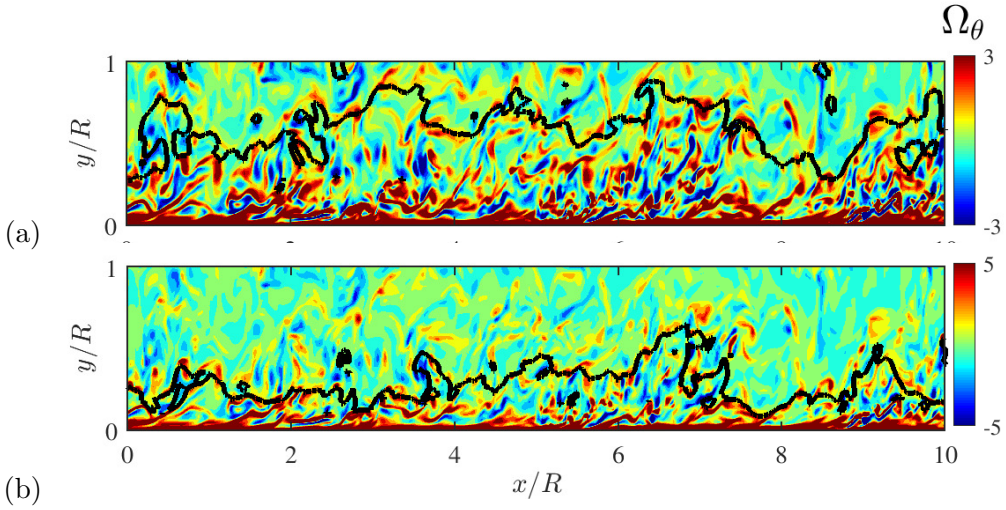

Figure 4.21: Contours of the azimuthal vorticity Ω_θ on a $x-y$ plane, superpositioned with instantaneous UMZ interfaces defined at (a) U_κ/U_{CL} = 0.9 and (b) U_κ/U_{CL} = 0.8. The background contours of Ω_θ differ in the range of the colour axis.

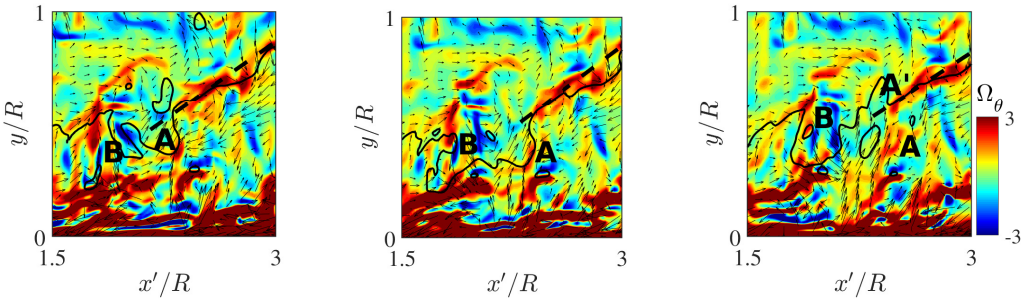

Figure 4.22: Contours of Ω_θ and a UMZ interface defined at U_κ/U_{CL} = 0.9 on a streamwise moving frame approximately at the bulk mean velocity, moving downstream with time from (a) to (c). The time gap between each two snapshots shown is uniform. Label A in (a,b) marks a prograde vortex which is weakened (b), and merged with nearby vortices at A' in (c). Label B marks a strong retrograde vortex on the interface. The vectors are the in-plane streamwise and wall-normal velocity fluctuations, u and v.

4.4.4 The vortex clusters on UMZ interfaces

Dynamics of the UMZ interface-azimuthal vortex attachment

The local peaks of the azimuthal vorticity at the UMZ interfaces in figure 4.20(a) suggests a strong correlation between the UMZ interfaces and the vortical structures. This matches the observation of clustered spanwise vortices along the UMZ interfaces in TBL by Adrian et al. (2000). Figure 4.21 shows two UMZ interfaces defined at U_κ/U_{CL} = 0.9 and 0.8 from the same snapshot and on the same $x-y$ plane. The interfaces are plotted on the top of the contour of Ω_θ, in which the prograde vortices are in red and the retrograde vortices are in blue. Different colour scales are used in figures 4.21(a) and (b) to improve the clarity of the surrounding vortical structures at different vortical strengths. On this $x-y$ plane, the interface continuously follows the azimuthal vortices with similar strength, so that the interface of the lower-travelling UMZ in figure 4.21(b) is on average, much closer to the wall, and is attached to visibly stronger vortices nearer the wall. This is consistent with the observations by Adrian et al. (2000) where patches of spanwise vortices were found aligned along the strong shear layers inside TBL. In figure 4.21, the UMZ interface threads through the azimuthal vortices and folds into bulges and valleys to form a persistent vortex-interface attachment.

The dynamics of this attachment between the UMZ interfaces and surrounding vortical structures is investigated. Movies of the temporal evolution of the attachment in both fixed and moving frames are available at https://doi.org/10.1017/jfm.2019.947. Figure 4.22 shows three snapshots with a constant time gap in a streamwise-moving frame travelling downstream approximately at the bulk mean velocity U_b. In the moving frame, the inclined trains of eddies from the wall towards the pipe centre, marked by the dashed lines are visibly stationary. The interface contorts to follow the surrounding azimuthal vortices. In figure 4.22(a), the interface initially attached to vortex A distorts when vortex A deforms and moves with the flow in figure 4.22(b). In figure 4.22(c), when vortex A is weakened and merged with other nearby eddies, the local shape of the interface changes significantly to reattach to a nearby vortex at A' to maintain the desirable vortical strength along the interface.

The three-dimensional attachment

Figure 4.23 shows the vortex-interface attachment on a cross-stream plane of the pipe with the same two UMZ interfaces shown in figure 4.21. The azimuthal vortices are elongated in the azimuthal direction. The vortices at similar vortical strength

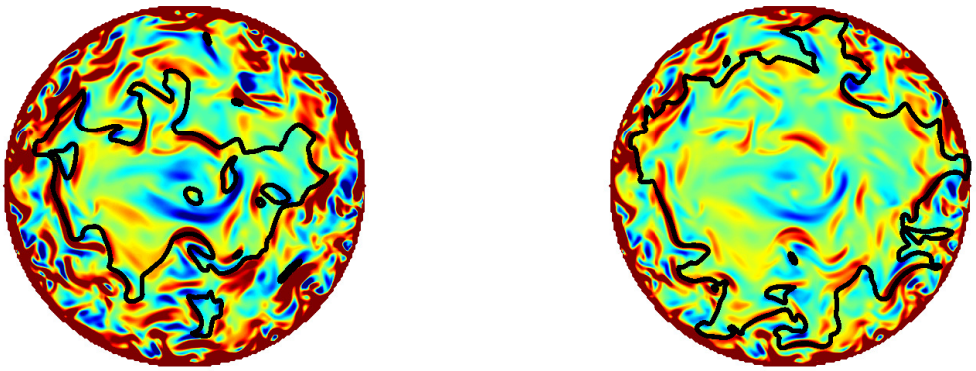

(a) (b)

Figure 4.23: Contours of the azimuthal vorticity Ω_θ on a $r-\theta$ plane, superpositioned with instantaneous UMZ interfaces defined at (a) $U_\kappa/U_{CL} = 0.9$ and (b) $U_\kappa/U_{CL} = 0.8$. The background contours of Ω_θ differ in the range of the colour axis.

reside at varying wall-normal locations. Similar to the attachment shown in the streamwise direction in figure 4.21, the UMZ interfaces contort to maintain a persistent attachment to individual vortices, twitch at the gaps between separate azimuthal vortices, and attach to the next nearby vortex at desired strength. The attachment in $3D$ is shown in figure 4.24 with UMZ interfaces as iso-surfaces of U_κ, coloured by the azimuthal vorticity on the surface. The attachment of the UMZ interface to vortical structures is visibly biased to red prograde vortices, whereas the blue retrograde vortices appear significantly less on the interface surface. The interfaces are coloured by ω_θ instead of Ω_θ where $\omega_\theta = \partial v/\partial x - \partial u/\partial r$, because for the interface at $U_\kappa/U_{CL} = 0.6$ residing in the proximity of the wall, the mean shear $\partial U/\partial y$ is too strong and the whole interface would appear in red.

To quantify the attachment, figure 4.25(a) shows the time-average PDFs of Ω_θ on the $3D$ interface of UMZs in different U_m groups. Through group M_1 to M_5, from the centre to the wall, the PDFs are increasingly skewed for stronger prograde vortices defined as positive Ω_θ. The prograde vortices are denoted as Ω_θ^p and the retrograde vortices are denoted as Ω_θ^r. Ω_θ^r is always negative, so that the strength of the retrograde vortices is $\mid \Omega_\theta^r \mid$. Ω_θ^p is stronger when being closer to the wall as expected for wall-bounded flows. The negative ends of the PDFs which represents the retrograde vortices on the UMZ interface show very small changes compared with Ω_θ^p. The magnitudes of Ω_θ^p at fixed PDF levels of 10^{-2}, 10^{-3} and 10^{-4} for each group (marked by '$\times$') are shown in figure 4.25(b). The increase in Ω_θ^p against U_m is almost linear.

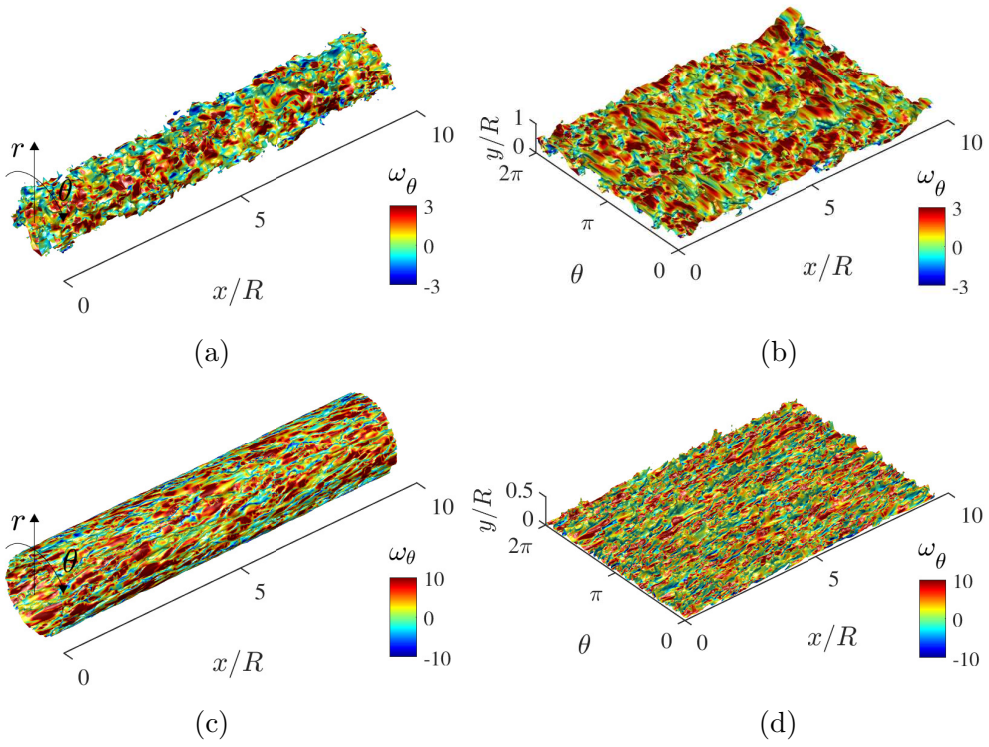

Figure 4.24: Iso-surfaces of the instantaneous streamwise velocity at (a,b) U/U_{CL} = 0.9 and (c,d) U/U_{CL} = 0.6, coloured by the azimuthal vorticity $\omega_\theta = \partial v/\partial x - \partial u/\partial r$ on the surface. The prograde vortices are in red. The iso-surfaces are unwrapped in (b,d), showing the sides facing the pipe centre.

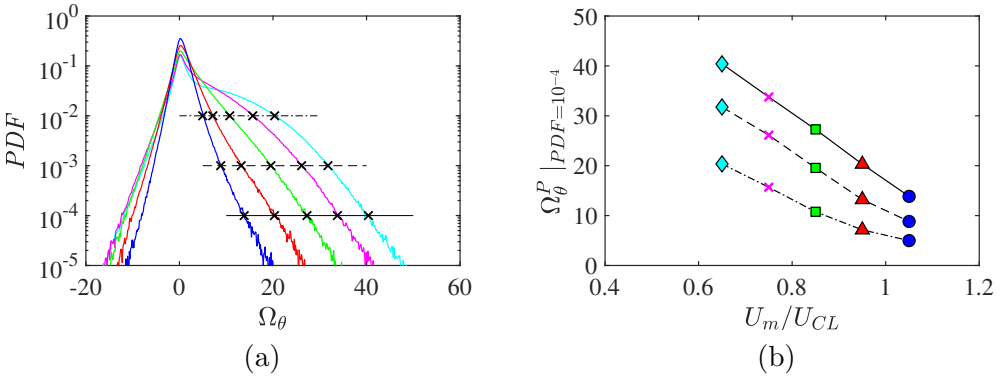

Figure 4.25: (a) PDF of the azimuthal vorticity Ω_θ on the UMZ interfaces for U_m groups $M_{i=1:5}$. Ω_θ is defined as positive for prograde vortices and negative for retrograde vortices. (b) The magnitude of prograde azimuthal vorticity, Ω^p_θ at probability density of 10^{-2}, 10^{-3} and 10^{-4} for groups as marked by '×' in (a).

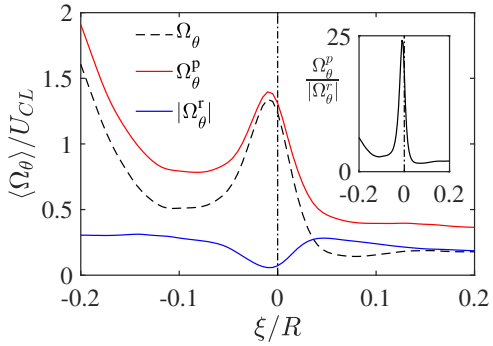

Figure 4.26: Conditionally averaged azimuthal vorticity Ω_θ, prograde vorticity Ω_θ^p and retrograde vorticity Ω_θ^r as functions of the distance from the UMZ interface, ξ for UMZs in U_m group M_2. The total azimuthal vorticity $\Omega_\theta = \Omega_\theta^p + \Omega_\theta^r = \Omega_\theta^p - |\Omega_\theta^r|$. The inset shows the ratio between Ω_θ^p and $|\Omega_\theta^r|$ against ξ.

Figure 4.26 shows the conditionally averaged profiles of the total azimuthal vorticity, the prograde vorticity, and the retrograde vorticity for UMZs in a single U_m group, M_2 against ξ. At the interface ($\xi = 0$) where the total Ω_θ peaks in figure 4.20(a), here it shows that nearly all the total vorticity Ω_θ at the interface is contributed by the prograde vortices Ω_θ^p while $|\Omega_\theta^r|$ decreases to a local minimum. The distribution of Ω_θ^p and $|\Omega_\theta^r|$ for group M_2 is very similar to the quiescent core in the channel (Yang et al. (2016)). Inside figure 4.26, the ratio between the prograde and retrograde vorticity on the interfaces of UMZs in group M_2 peaks at the interface, achieving $\Omega_\theta^p/|\Omega_\theta^r| \approx 25$. Results in this section suggest that the three-dimensional contortion of the UMZ interfaces is a consequence of the irregularly distributed azimuthal/spanwise vortices which move three-dimensionally with varying wall-normal locations. Additionally, the attachment is predominantly to prograde vortices.

4.4.5 The contortion of UMZ interface

The contortion of the UMZ interfaces forms bulges and valleys similar to the engulfment of TNTI. The interface contortion is essentially a different way of viewing the streaky feature of the streamwise velocity fluctuation. Figure 4.27 shows an instantaneous UMZ interface from group M_2 defined at $U_\kappa/U_{CL} = 0.9$, coloured by the interface radial location similar to figure 4.16. The valleys in red are induced by high-speed fluids sweep closer towards the wall, and the bulges in blue are induced by the low-speed fluids ejected away from the wall. The contorted interface residing away from the wall largely represents the LSM.

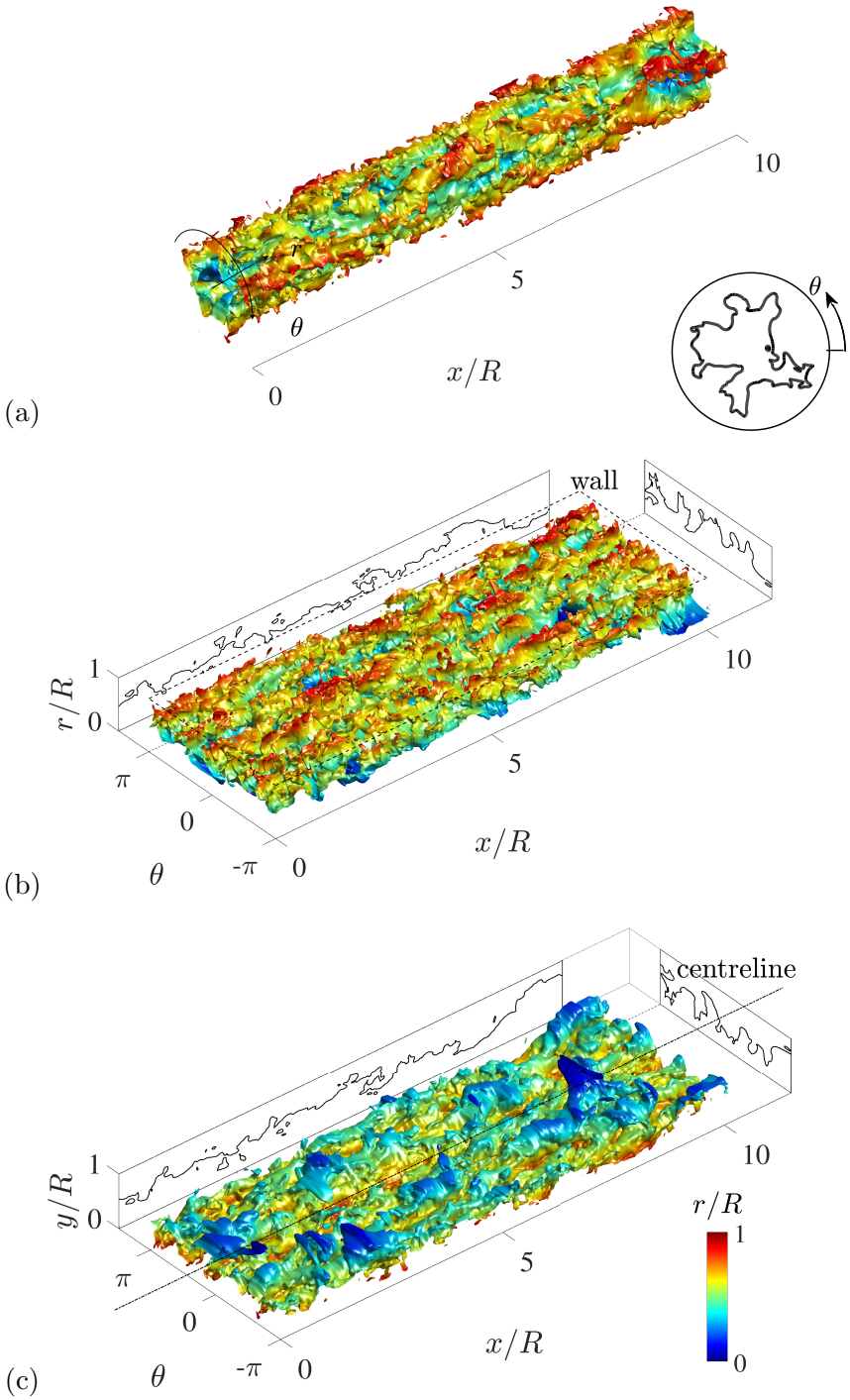

Figure 4.27: A $3D$ UMZ interface as iso-surface defined at $U_\kappa/U_{CL} = 0.9$, coloured by the interface radial elevation. The bulges of low-speed fluid ejected away from the wall are in blue, the valleys of high-speed fluid sweeping towards the wall are in red. The interface is unwrapped in the azimuthal direction, showing the side facing the wall in (b) and the side facing the pipe centre in (c). The interface $2D$ projections are plotted on the $x-y$ plane at $\theta = \pi$ and the cross-stream $r-\theta$ plane at $x/R = 10$.

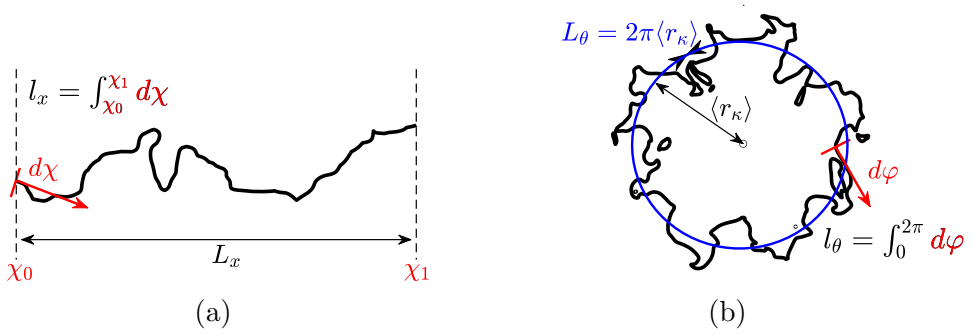

Figure 4.28: Schematic illustration of the definition of UMZ interface tortuosity, calculated as the length of interface per unit length in the streamwise and azimuthal directions.

The UMZ interface is unwrapped along the azimuthal direction in figure 4.27(b) and (c), showing the outer surface of the interface facing the pipe wall and the inside of the interface facing the pipe centre, respectively. The streaks of the high- and low-momentum pathways are very clear and are similar to interface visualised in a channel by Kwon et al. (2014) (see their figure 5). The inner surface in figure 4.27(c) is not visible without unwrapping. The inner face of the UMZ interface shows some significantly amplified bulges (blue), for example, at $\theta = 0$ and $x/R \approx 8$, which was not evident for the channel results. This particular UMZ interface in the figure is located relatively in the centre of the pipe ($\langle y_\kappa \rangle \approx 0.5R$) where the features of the LSM are visibly evident, and bears a clear similarity to those in the channel flow (Monty et al. (2007); Illingworth et al. (2018)).

The $2D$ contortion

The level of contortion (tortuosity) of the UMZ interfaces in the streamwise and the azimuthal directions are investigated. The length of the $2D$ UMZ interfaces on the $x-y$ planes and the $r-\theta$ planes are denoted as l_x and l_θ, respectively. In figures 4.27(b,c), the projections on the streamwise and cross-stream planes show examples for l_x and l_θ, respectively. Figure 4.28 shows the definition of l_x and l_θ which are computed by an algorithm that calculate the exact length of the interface using the high-resolution data. The lengths of the islands isolated from the continuous main part of the interface on $2D$ planes are preserved because it is found that the frequently observed islands are often connected to the main interface in $3D$, as a feature of the three-dimensional interface contortion.

The tortuosity of the UMZ interface is defined as the interface length per unit length in the streamwise and azimuthal directions, l_x/L_x and l_θ/L_θ as shown in figure 4.28. l_x is normalised by the fixed streamwise extent of the pipe $L_x = 30R$ while l_θ is normalised by the perimeter of a circle with a radius equals to the interface average radius, $\langle r_\kappa \rangle$. Because $\langle r_\kappa \rangle$ varies for UMZs in different U_m groups, the unit length in the azimuthal direction L_θ is not constant, being longer nearer the wall. In figure 4.29(a), the group average l_x/L_x and l_θ/L_θ increase as UMZs move away from the wall towards pipe centre, so that the level of UMZ interface contortion intensifies for interfaces further away from the wall in both directions. The UMZ interface is always more contorted in the azimuthal direction than in the streamwise direction with l_θ/L_θ always higher than l_x/L_x in all U_m groups. This was found the same in the channel by Yang et al. (2016) which has l_x/L_x overlaid in the figure as '□' and l_θ/L_θ by '☆'. The increase of both l_x/L_x and l_θ/L_θ is rather slow initially near the wall. However, away from the wall, l_θ/L_θ shows a significantly more rapid increase towards to the pipe centre whereas l_x/L_x increases much more slowly than l_θ/L_θ. The $2D$ azimuthal contortion l_θ/L_θ shows a very strong wall-distance dependence compared to l_x/L_x since L_θ increases in the radial direction with $\langle r_\kappa \rangle$. A constant unit azimuthal length $L'_\theta = 2\pi R$ is also used for normalisation, which is more comparable to the channel with a fixed spanwise extent. l_θ/L'_θ (represented by colour-filled symbols) still increases as UMZs move away from the wall but much more slowly with a very similar trend to l_x/L_x. Importantly, l_θ/L'_θ is still always higher than l_x/L_x as found in the channel, suggesting that the contortion of the UMZ interface is stronger in the azimuthal direction than in the streamwise direction in both channel and pipe.

The $2D$ contortion in the streamwise direction l_x/L_x from TBL by de Silva et al. (2016) of $Re_\tau = 1200-14500$ is also overlaid on the pipe results in figure 4.29(a). There is a clear increase in l_x/L_x when Reynolds number increases in TBL. For UMZs in U_m groups M_3 and M_4, the streamwise tortuosity of their interfaces in pipe at $Re_\tau = 500$ is quantitatively similar to the TBL results at a roughly doubled Reynolds number $Re_\tau = 1200$. This supports the previous findings in figures 4.19(g,h) where UMZs in pipe at a lower Reynolds number are quantitatively more similar to TBL at higher Reynolds numbers.

The $3D$ contortion

The $3D$ contortion of the UMZ interface is measured by the surface area of the interface S_κ per unit area $L_x L_\theta$. $L_x L_\theta$ is essentially the area of a smooth tube with a radius equals to the average radial location of an UMZ, $\langle r_\kappa \rangle$ as illustrated in figure

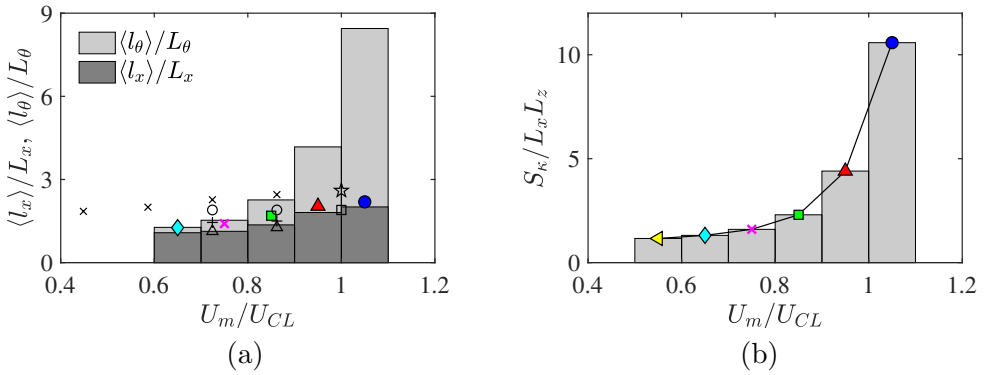

Figure 4.29: (a) The tortuosity of the $2D$ UMZ interface: the average length of UMZ interfaces per unit length in the streamwise direction, l_x/L_x and the in azimuthal direction, l_θ/L_θ for U_m groups $M_{1:5}$. $L_x = 30R$ is the constant pipe streamwise extent whereas the azimuthal extent $L_\theta = 2\pi\langle r_\kappa \rangle$ varies for UMZ interfaces with varying radial locations $\langle r_\kappa \rangle$. The colour-filled markers are l_θ/L'_θ, normalised by a constant azimuthal extent $L'_\theta = \pi R$. The results in TBL at $Re_\tau = 14500$ (×), $Re_\tau = 8000$ (○), $Re_\tau = 2800$ (+) and $Re_\tau = 1200$ (△) de Silva et al. (2017) are overlaid for l_x/L_x. The channel flow results at $Re_\tau = 1000$ by Yang et al. (2016) has l_x/L_x (□) and l_θ/L_θ (☆). (b) The tortuosity of the $3D$ UMZ interface: the average surface area of $3D$ UMZ interfaces, S_κ, per unit area $L_x L_z$.

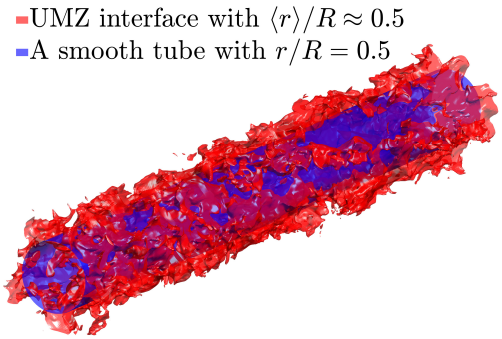

Figure 4.30: Illustration of measuring the $3D$ tortuosity of a UMZ interface by normalising the surface area of the interface S_κ with a unit area of a smooth tube defined by the average radius of the interface.

4.30. Figure 4.29(b) shows S_κ/L_xL_θ for U_m groups $M_{1:6}$. S_κ/L_xL_θ shows a very similar trend to l_θ/L_θ in which the increase is rather slow initially in groups $M_{6:4}$ with UMZ interface area roughly twice the unit area ($S_\kappa/L_xL_\theta \approx 2$). The $3D$ contortion is the lowest for UMZs closest to the wall (M_6) and achieve the highest $S_\kappa/L_xL_\theta \approx 11$ in group M_1. Importantly, S_κ of the inner most UMZ interfaces (M_1) is over 10 times the non-contorted reference area on average, indicating extremely large-scale engulfment of the interface of UMZs travelling above the centreline velocity. The contortion of the UMZ interfaces behaves as a function of the wall-distance, both the $2D$ and $3D$ contortion of UMZ interfaces intensify when departing away from the wall. This may be partly due to the suppression from the wall where interfaces are less free to meander and also because that the streamwise fluctuation is in smaller scales nearer the wall. The increase in UMZ interface contortion with distance from the wall shows the increase in meandering of the LSMs with wall-distance (Kevin et al. (2019)).

4.4.6 UMZ interface asymmetry

The symmetry/asymmetry between local $Q2$ ejections (bulges) and $Q4$ sweeps (valleys) on the UMZ interfaces is investigated over a wide range of scales in the pipe along the wall-normal direction. Figure 4.31 shows an unwrapped $3D$ UMZ interface in U_m group M_2 in (a), residing away from the wall, and another UMZ interface in group M_6 in (b), residing extremely close to the wall. The fluctuation of the wall-normal location of the UMZ interface is defined as $y'_\kappa = y_\kappa - \langle y_\kappa \rangle$. y'_κ is plotted on the cross-stream plane at $x/R = 5$. Positive y'_κ corresponds to the bulges on UMZ interfaces while negative y'_κ represents the valleys. In figure 4.31(a), y'_κ of the interface approximately at the half of the pipe radius shows no clear bias, whereas the interface near the wall in figure 4.31(b) is clearly skewed towards positive y'_κ, indicating amplified ejections over sweeps. This matches the findings in channel and TBL where the amplified near-wall activities as footprint of the large-scale structures (Marusic (2001); Jiménez et al. (2004); Hutchins and Marusic (2007b,a); Mathis et al. (2009a,b)) were found asymmetric towards ejections into bursting (Agostini and Leschziner (2014)).

The asymmetry between bulges and valleys, ejections and sweeps are measured by the skewness of y'_κ as a function of the wall-distance using in $3D$ volumetric data. The skewness of y'_κ is computed as $\zeta = y'^3_\kappa/\sigma^3$ where σ is the standard deviation of y'_κ. Positive ζ indicates asymmetry with biased ejection over sweep; negative ζ indicates sweep over ejection; and $\zeta = 0$ indicate locally balanced ejection and sweep. Figure 4.32 shows the average skewness $\langle \zeta \rangle$ for UMZs in U_m groups. The UMZs

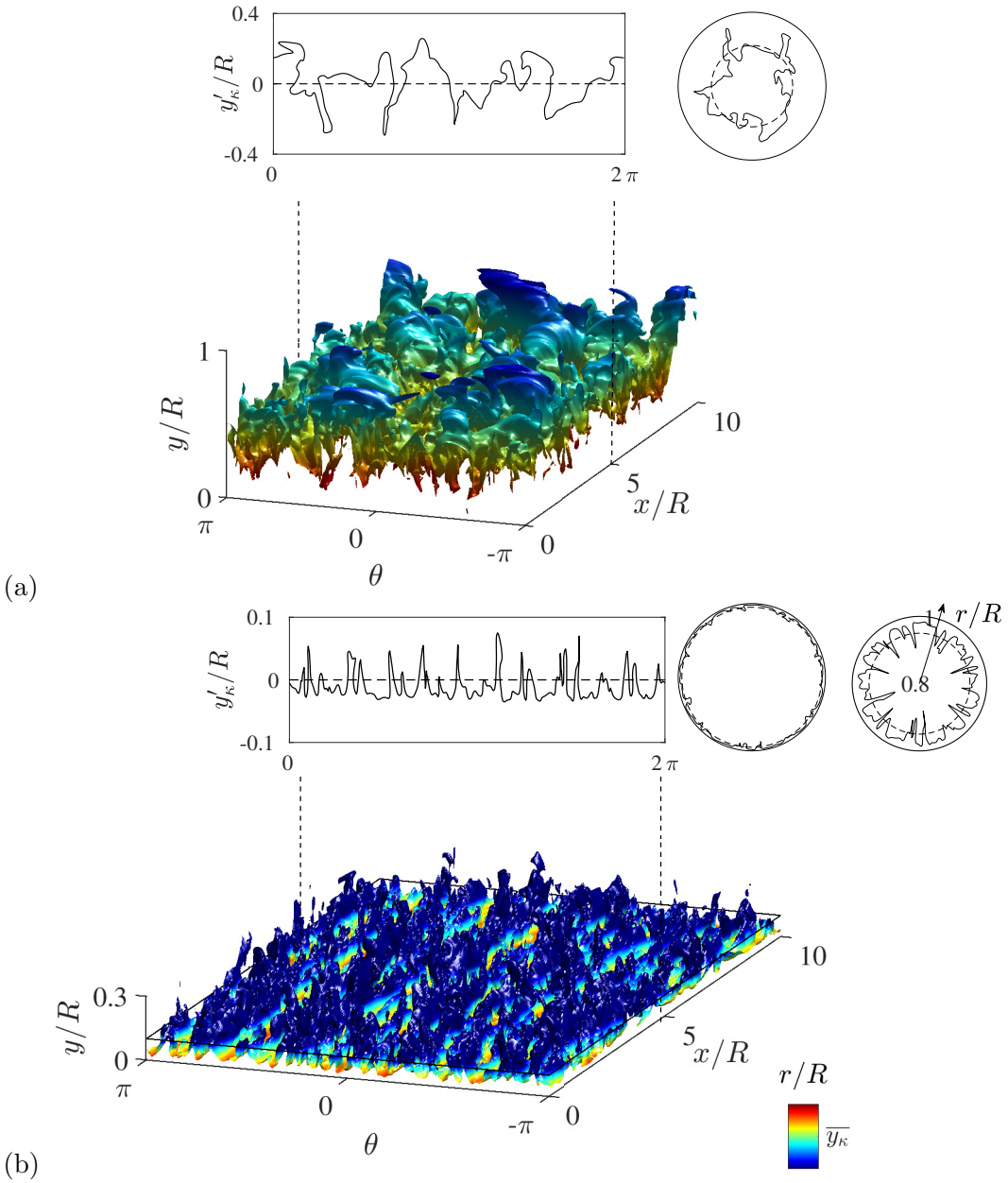

Figure 4.31: A $3D$ UMZ interface at (a) $U_\kappa/U_{CL} \approx 0.9$ and (b) $U_\kappa/U_{CL} \approx 0.6$. The colour axes are always centring the average wall-normal location of the interface $\langle y_\kappa \rangle$. The $2D$ projections of the interfaces are plotted at $x/R = 5$. The fluctuation of the interface wall-normal location, $y'_\kappa = y_\kappa - \langle y_\kappa \rangle$.

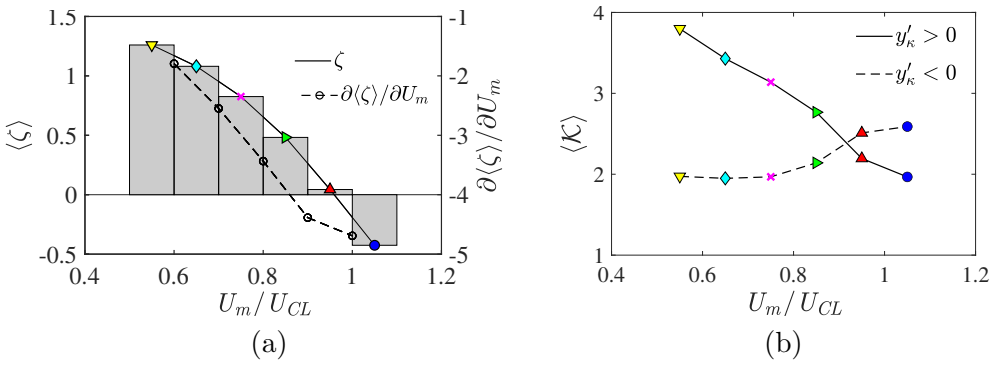

Figure 4.32: The average skewness of the UMZ interface wall-normal location fluctuation, ζ, around the average interface location, $y'_\kappa = y_\kappa - \langle y_\kappa \rangle$ of UMZs in each U_m group. Positive ζ indicates that the interface is skewed towards the pipe centre, and vice versa. $\zeta = 0$ indicates an overall balance between bulges and valleys on the interface. (b) The average kurtosis $\mathcal{K}$ of the positive ($Q2$ ejection) part and negative ($Q4$ sweep) part of the UMZ interface fluctuation y'_κ for UMZs in each U_m group.

closest to the wall in group M_6 show the highest asymmetry towards $Q2$ ejections. The level of asymmetry biased to ejection events decreases for UMZs departing away from the wall towards the pipe centre. For the UMZs in group M_2 which are the most comparable to the quiescent core in channel (Kwon et al. (2014); Yang et al. (2016)), $\zeta \approx 0$, indicating that the UMZs in this group have fairly balanced sweep and ejection. The innermost UMZ group M_1 is the only group with negative average ζ, so that these innermost UMZs travelling above the centreline velocity exhibit opposite asymmetry between local sweeps and ejections. The gradient of the decrease in asymmetry level, $\partial\zeta/\partial U_m$ is plotted on the right-hand-side y-axis.

Another observed feature of the UMZ interfaces in figure 4.31 is that the UMZ interface closer to the wall in figure 4.31(b) is spikier for $Q2$ ejections ($y'_\kappa > 0$) whereas the $Q4$ sweep regions are relatively smooth and flat. Away from the wall, the interface in figure 4.31(a) shows the opposite, in which the sweeps towards the wall are spikier than ejections. Figure 4.32 shows the statistical measurement of the spikiness of the UMZ interfaces by computing the kurtosis $\mathcal{K} = y'^4_\kappa/\sigma^4$ separately for the ejection part ($y'_\kappa > 0$) and the sweep part ($y'_\kappa > 0$) of the UMZ interfaces. The spikiness of the ejection part of the UMZ interface decreases monotonically with wall-distance whereas $\mathcal{K}$ of the sweep region increases towards the pipe centre. $\mathcal{K} \mid y'_\kappa > 0$ and $\mathcal{K} \mid y'_\kappa < 0$ cross over between groups M_2 and M_3, the UMZ interfaces in groups $M_{1,2}$ (which occupy the centred half of the pipe on average) have opposite spikiness between ejection and sweep structures from all the other UMZs residing closer to the wall. The UMZs closest to the wall in group M_6 has ejection regions

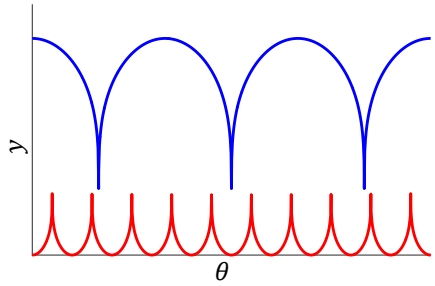

Figure 4.33: A schematic drawing of the reversed structure of ejections and sweeps

nearly twice sharper than the sweeps ($\mathcal{K} \mid y'_\kappa > 0 / \mathcal{K} \mid y'_\kappa < 0 \approx 1.93$) whereas the inner most UMZs has ejections 25% less sharp than the sweeps. The spiky upper part of the near-wall UMZ interfaces and the lower part of the centre interfaces show an interlocking structural arrangement between the near-wall ejections and the large-scale sweeps from the centre, illustrated by figure 4.33. The flatness of the near-wall sweeps and centre ejections on the UMZ interface is possibly due to the suppression from the wall and the congested pipe centre with flow coming in from the opposing walls, respectively.

4.4.7 Statistics of UMZs detected from KDE

As shown in table 2.2, in the list of all the UMZ studies identifying the UMZs from the PDF of U, Fan et al. (2019) replaced the PDF with the kernel density estimation (KDE) without the requirement of multiple user-defined constraints but a single KDE bandwidth h. Here, part of the statistical characteristics of the UMZs shown in previous sections are reproduced for UMZs identified from using their KDE approach. A consistent algorithm to Fan et al. (2019) is used: a Gaussian KDE with bandwidth $h = \sigma(4/3)^{1/5}N^{-1/5}$ where σ is the standard deviation of U from the snapshot and N is the sample size of U.

Figure 4.34(a) shows the histogram of U from an instantaneous snapshot where the kernel function and the peak detection agree to each other on the well-distinctive peaks. The KDE algorithm suggests fewer number of UMZs $N_{UMZ} \approx 3$ on average than the PDF method (figure 4.14), but N_{UMZ} is still higher in pipe than channel (Fan et al. (2019)) when both using KDE for UMZ detection. Figure 4.34(b) shows the PDF of the number of UMZs detected from KDE in each of the modal velocity groups used in this study. The KDE bandwidth filters away many of the slower-travelling UMZs in the lower U_m groups but the distribution is very

similar to the result from using the peak detection scheme (figure 4.15. In figures 4.34(a,b) show the average wall-normal location and the $2D$ contortion of UMZ interfaces in the higher U_m groups $M_{1:4}$ and correspond to figure 4.17(a) and 4.29(a) respectively. The change of detection scheme alters the group average but the trend of y_κ and l_θ/L_θ is consistent: the UMZs are thicker away from the wall, forming a hierarchical distribution and the UMZ interfaces are wavier when departing away from the wall. The replicated results using KDE instead of PDF peak detection show that the statistical behaviours of the UMZ are reasonably insensitive to the detection scheme.

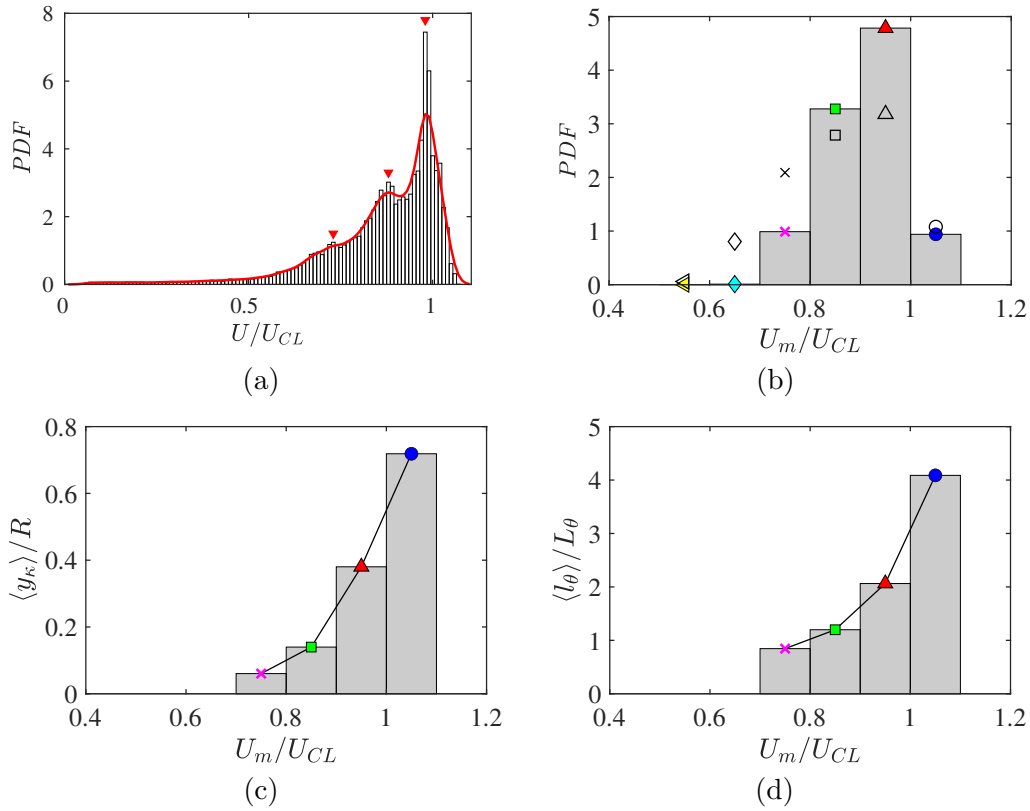

Figure 4.34: Results of UMZs detected from using the KDE method. (a) An instantaneous PDF of U. The red line is the kernel estimation function of the PDF with bandwidth $h = \sigma(4/3)^{1/5}N^{-1/5}$; the peaks on the KDE representing the local UMZs are marked by '▼'. (b) PDF of UMZs in each U_m group of $M_{1:6}$ as in table 4.2 for UMZs detected from KDE. (c) Conditional average interface wall-normal location y_κ for UMZs detected from KDE in U_m groups $M_{1:4}$. (d) $2D$ UMZ interface folding intensity in the azimuthal direction, l_θ/L_θ for each U_m group. The KDE results in (a,b,c,d) correspond to figures 4.5(a), 4.15, 4.17 and 4.29(a), respectively.

4.5 Internal shear layer

This section investigates the characteristics of the internal shear layers/UMZ interfaces, and the large-scale coherent structures around the ISLs in the present pipe using DNS data at all four Reynolds numbers, Re_τ = 180, 360, 500 and 1000. The ISLs are identified from using a unique method using the peaks on the velocity gradients with no ad-hoc filter applied on the ISL selection. This is different from all the previous UMZ and ISL studies in tables 2.2 and 2.1 in a way that no constraints, thresholds or filters are applied in the identification scheme.

In this study, ISLs are ranked by both their shear strength and wall-distance. As an extension of the UMZ results at a single Reynolds number Re_τ = 500 in section 4.4, the signature behaviours of the ISL including an abrupt streamwise velocity jump and a sharp decrease in velocity fluctuation across the ISL are first validated across Reynolds numbers in this section. The local imbalance between ejections and sweeps observed in section 4.4 are evident. In the last part, the $3D$ picture of flow structures around an ISL are obtained via volumetric conditional sampling.

Part of the results in this section were previously published in Chen et al. (2021).

4.5.1 Identification of ISL

Figure 4.35(a) shows the profiles of the instantaneous streamwise velocity U at several equally-spaced streamwise locations in the pipe at Re_τ = 1000, which is the highest Reynolds number of our dataset. The signatures of the UMZ where U changes sharply at several high-shear locations (in regions highlighted in magenta) between large regions of relatively constant U (highlighted in green) are clear. The red dotted lines are the streamwise cumulative averages from the pipe inlet to the $x-$location of each instantaneous profile. While averaging, the cumulative average profile of U rapidly converges to the mean velocity profile $\overline{U}$ (blue dashed lines). The corresponding profiles of the velocity gradient $\partial u/\partial y$ are shown in figure 4.35(b). The wall-normal locations of the locally peaked shear are represented by the peaks on the velocity gradient profiles, marked by '◀'.

The number of UMZs and ISLs is well known to be sensitive to the detection methods and user-defined parameters. The user-defined parameters decide which UMZ or ISL to be collected. Stricter conditions reduce the sample size where the PDF- and ISL-based methods will preferentially preserve the larger UMZs and stronger ISLs, respectively. The sample of UMZs and ISLs for statistical analysis is therefore, more or less, biased. In the present study, all $\partial u/\partial y$ peaks are used

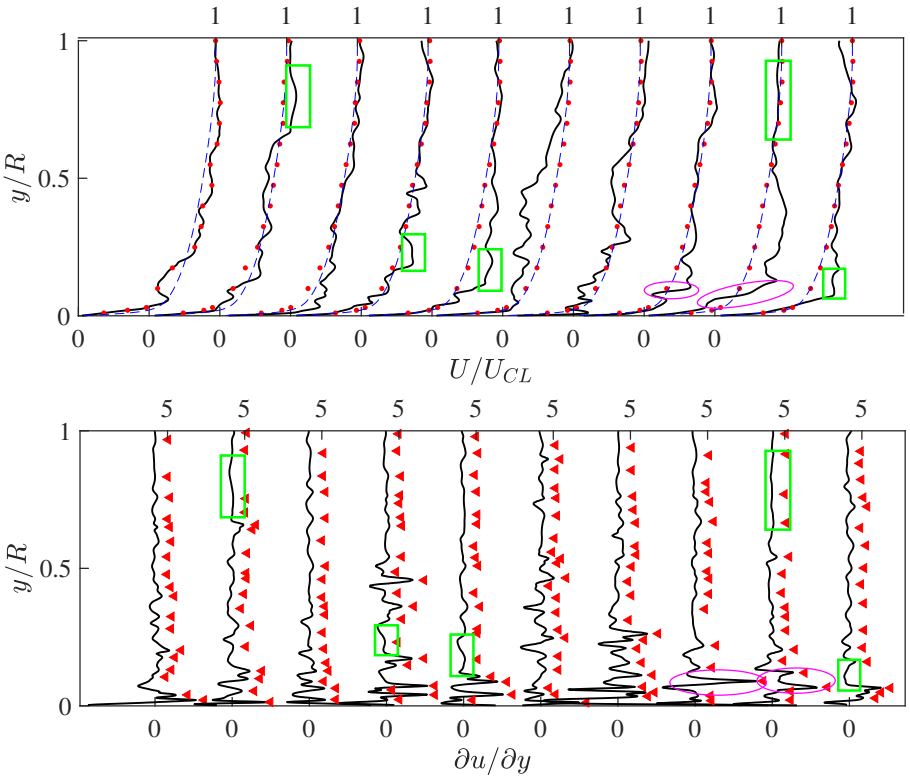

Figure 4.35: (a) Instantaneous velocity profiles U at ten equal-spaced streamwise location x from a snapshot at Re_τ = 1000 with gap $x/R \approx 3$. The blue dashed lines are the mean velocity profile $\overline{U}$ and the red dotted lines are the cumulative streamwise averages from the pipe inlet up to the $x-$location of each instantaneous profile. (b) Profiles of the velocity gradient $\partial u/\partial y$, corresponding to each profile of U in (a). The local maxima (peaks) of $\partial u/\partial y$ are marked by '◀'.

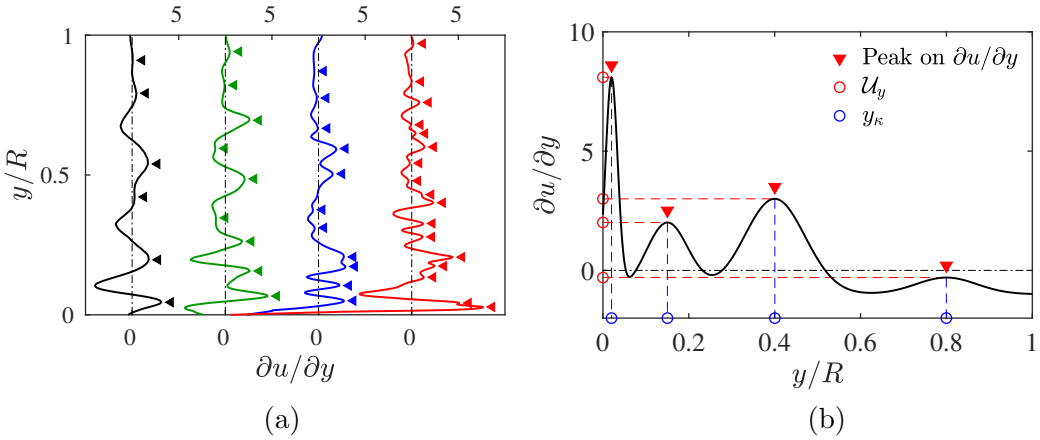

Figure 4.36: (a) An instantaneous profile of $\partial u/\partial y$ at Re_τ = 180 (black), 360 (green), 500 (blue) and 1000 (red). The peaks on $\partial u/\partial y$ are marked by '◀'. (b) An idealised instantaneous $\partial u/\partial y$ profile to illustrate the definition of the shear strength at the $\partial u/\partial y$ peaks, $\mathcal{U}_y$ and the wall-normal location of the locally peaked shear, y_κ.

without any ad-hoc filter to compute the statistics of the local high-shear regions. In this approach, the relatively weak ISLs and the ISLs bounding a very small UMZ which may have been neglected in the previous ISL-based and PDF-based methods will be included in the statistics. Figure 4.36(a) shows an $\partial u/\partial y$ profile at each of the four Reynolds numbers. There are clearly more peaks of high shear at higher Reynolds numbers as expected because of its wider range of scales. This is consistent with the observation of increasing number of UMZs with increasing Reynolds number (de Silva et al. (2016, 2017)).

The $\partial u/\partial y$ profiles in the whole $3D$ pipe domain over time are computed using a n^{th}-order centred finite difference scheme where n is the number of neighbouring data point available up to a limit of $n = 8$. As illustrated in figure 4.36(b), from each instantaneous $\partial u/\partial y$ profile, the number of peaks N_κ, the shear strength at the peaks $\mathcal{U}_y$, and the wall-distance of the peaks y_κ are collected. The ISLs identified on a $2D$ cross-stream plane of the pipe at Re_τ = 180 are shown in figure 4.37. On the $r-\theta$ plane, the points detected with local peak shears connect and form numerous contorted ISL filaments. The ISL filaments are visibly located in the middle of the red strong shear regions on the contour.

Figure 4.38(a) shows the PDFs of the number of peaks on the instantaneous $\partial u/\partial y$ profiles, N_κ. The number of ISL increases with the Reynolds number, consistent with de Silva et al. (2016) and Fan et al. (2019). The PDFs also increase in span with increasing Reynolds number so that the number of ISLs in the flow varies

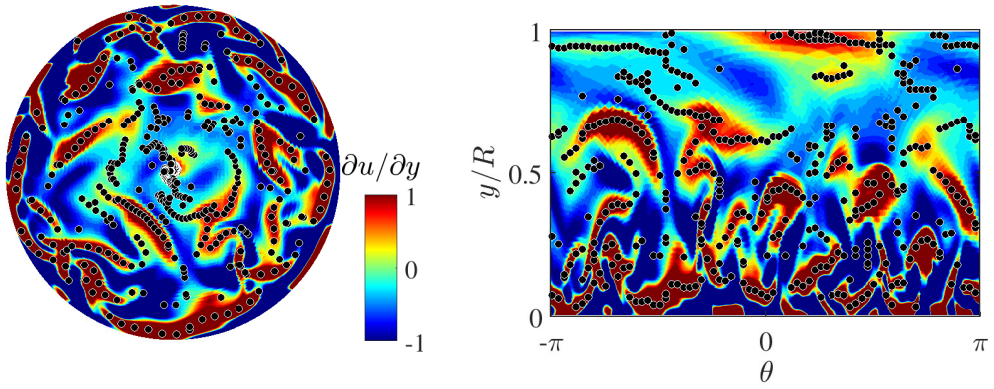

Figure 4.37: Contour of $\partial u/\partial y$ on a cross-stream plane in the pipe at Re_τ = 180, superpositioned with the ISLs detected from $\partial u/\partial y$ peaks.

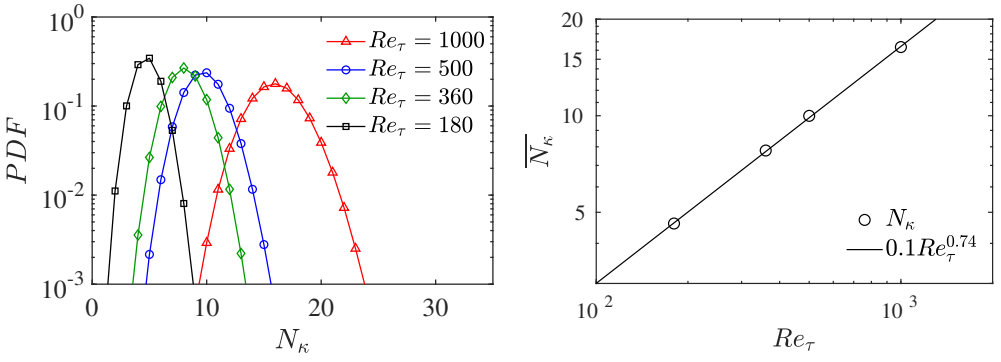

Figure 4.38: (a) PDF of the number of peaks detected from each $\partial u/\partial y$ profile, N_κ for Re_τ = 180 (black), Re_τ = 360 (green), Re_τ = 500 (blue) and Re_τ = 1000 (red). (b) Average number of peaks on a $\partial u/\partial y$ profile, $\overline{N_\kappa}$ with a fitting function of $\overline{N_\kappa} = 0.1Re_\tau^{0.74}$.

more largely at higher Reynolds numbers. The average number of ISL, $\overline{N_\kappa}$, for each Reynolds number is shown in figure 4.38(b). The fitting function $\overline{N_\kappa} = 0.1Re_\tau^{0.74}$ show an excellent agreement with the data, which suggests a power-law scaling of the average number of ISL with the Reynolds number. This provides a prediction on the number of hierarchical UMZs in a pipe flow at any Reynolds number lied in the range of $Re_\tau < 1000$. However, the fitting function needs to be tested on much higher Reynolds numbers ($\mathcal{O}(10^4)$) to validates its universality. Note that the results in later sections are computed from $\partial u/\partial y$ profiles with $N_\kappa = \overline{N_\kappa}$ only, in which $\overline{N_\kappa} = 5$, 8, 10 and 16 at $Re_\tau = 180$, 360, 500 and 1000, respectively, by taking the nearest integer.

Grouping of the ISL

The statistics of the ISLs are computed by group averaging. The group averaged quantities are denoted as $\langle\cdot\rangle$. The $\partial u/\partial y$ peaks are categorised into different groups based on their certain properties. Two grouping schemes are used for the ISLs: the ISLs are grouped based on their shear strength, $\mathcal{U}_y$ in section 4.5.2, and their wall-distance, y_κ in section 4.5.3. More importantly, instead of using user-defined ranges of $\mathcal{U}_y$ and y_κ for the grouping, the rankings of these two quantities are used. For groups based on the shear strength, on each profile of $\partial u/\partial y$ along the wall-normal direction, the peak with the highest $\mathcal{U}_y$ is ranked as 1, and the other peaks follow in a descending order of $\mathcal{U}_y$. For instance, the $\partial u/\partial y$ profile in figure 4.36(b) has four peaks, $p1$ to $p4$, which would be ranked as 1, 3, 2 and 4, respectively based on their $\mathcal{U}_y$ values. For groups based on the shear layer wall-distance, the peak being the closest to the wall is ranked as 1 and the others follow in an ascending order of y_κ so that $p1$ to $p4$ in figure 4.36(b) would be ranked as 1, 2, 3 and 4. In this study, the groups ranked by $\mathcal{U}_y$ are called the shear-strength group R_i^s and the groups ranked by y_κ are called the wall-distance group R_i^y, where i denotes the rank. The group R_1^s consists of the strongest positive shears on each $\partial u/\partial y$ profile, while group R_1^y includes the most near-wall shear layer on each $\partial u/\partial y$ profile.

4.5.2 ISL properties as functions of shear strength

In this section, group averages are computed for the shear-strength groups R^s. The average strength of the ISLs in each R^s group, $\langle\mathcal{U}_y\rangle$, is shown in figure 4.39(a) in wall units. As expected, group R_1^s with the highest shear from each $\partial u/\partial y$ profile naturally has the highest average shear strength, and the shear strength decreases rapidly as the rank increases. At all four Reynolds numbers, the average shear

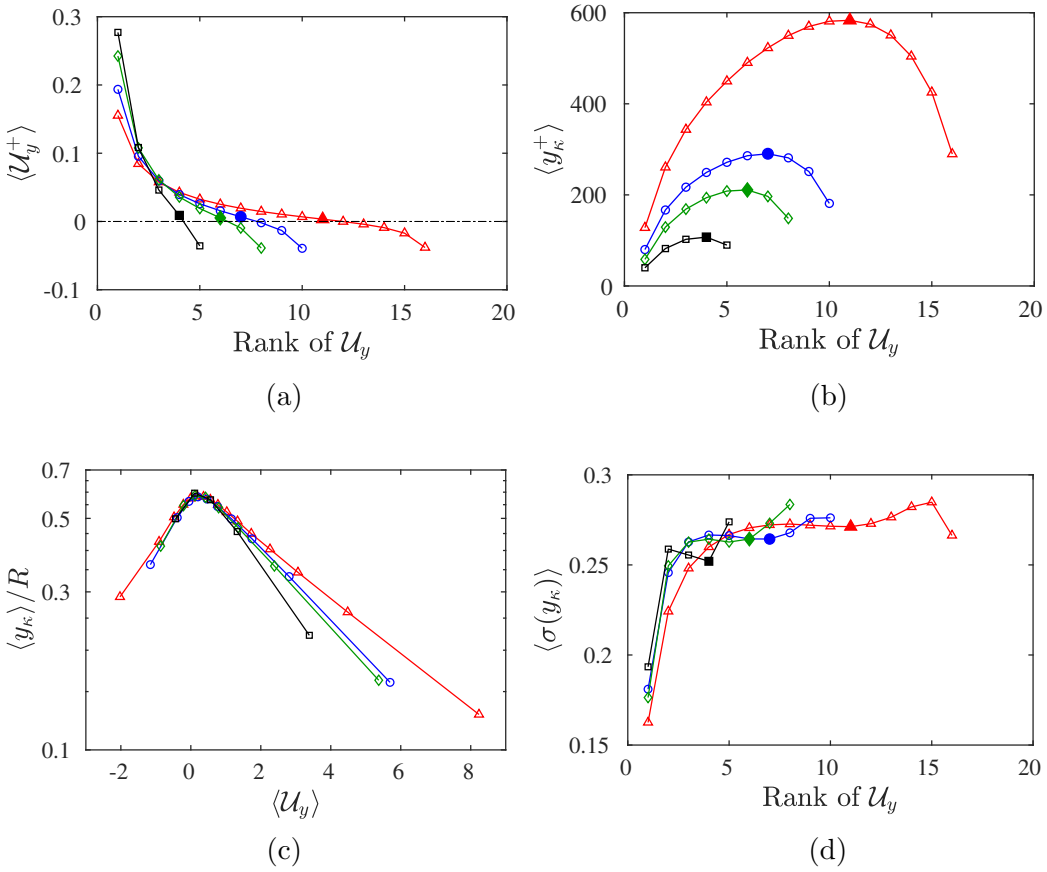

Figure 4.39: (a) Local maximum shear $\mathcal{U}_y$ at the peaks on $\partial u/\partial y$, (b) Wall-normal location of the peaks, y_κ in wall units, (c) $\langle y_\kappa \rangle$ against $\langle \mathcal{U}_y \rangle$ and (d) standard deviation of y_κ, $\sigma(y_\kappa)$; averaged within each shear-strength group R^s based on the ranking of $\mathcal{U}_y$. The colours and symbols for different Reynolds numbers follow figure 4.38(a). The solid symbol at each Reynolds number is the lowest rank with $\mathcal{U}_y$ remaining positive in (a).

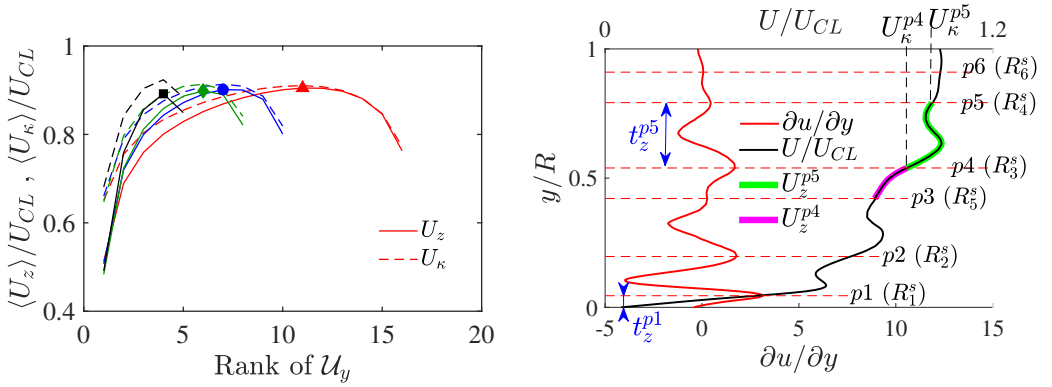

Figure 4.40: (a) Zonal mean velocity U_z (solid lines) and shear layer velocity U_κ (dashed lines), averaged within each shear-strength group R^s based on the ranking of $\mathcal{U}_y$. (d) Illustration of the definition of shear layer velocity U_κ at each $\partial u/\partial y$ peak and the zonal mean velocity U_z computed in the region between each $\partial u/\partial y$ peak and its adjacent peak closer to the wall.

strength becomes negative at a certain rank, which suggests that the majority of the shear layers in the groups with $\langle \mathcal{U}_y \rangle < 0$ are negative shears ($\partial u/\partial y < 0$). The lowest rank with positive $\langle \mathcal{U}_y \rangle$ is denoted as R^s_*, and is marked by solid symbols in figure 4.39 and figure 4.40. For Re_τ = 180, 360, 500 and 1000, R^s_* is R^s_4, R^s_6, R^s_7 and R^s_{11}, respectively. Figure 4.39(b) shows the average wall-normal location of the ISLs in each R^s group. The strongest shear layers in R^s_1 are located closest to the wall as expected. It is interesting to note that group R^s_* is located furthest from the wall for all Reynolds numbers. The ISLs in the groups ranked lower than R^s_* move closer to the wall as the rank increases, so that the stronger negative shear layers reside closer to the wall where the positive shear layers are also stronger. In figure 4.39(c), the group average wall-distance is plotted against the group average shear strength. The magnitude of shear strength $|\,\mathcal{U}_y\,|$ being stronger towards the wall is true for both the positive and negative shears. Figure 4.39(d) shows the standard deviation of the wall-distance fluctuation of the shear layers $\sigma(y_\kappa)$ in each R^s group. A high $\sigma(y_\kappa)$ indicates that the wall-normal location of the ISLs belonged to a R^s group varies largely. As the ISLs are grouped by the ranking of their shear strength here, a high $\sigma(y_\kappa)$ does not necessarily indicate large meandering of a continuous ISL but may simply represents the range of wall-distance that an ISL of a given shear strength tends to reside in. While $\sigma(y_\kappa)$ remains quite large for all other ranks, R^s_1 has a small $\sigma(y_\kappa)$, indicating the relative stability of the ISLs in group R^s_1. There

is a small increase in $\sigma(y_\kappa)$ for ranks larger than R^s_* (solid symbols) for all four Reynolds numbers, suggesting that the negative shear layers reside, on average, in a wider wall-normal span.

Figure 4.40 shows the group averages of the streamwise velocity at $\partial u/\partial y$ peaks, U_κ, and the zonal mean velocity U_z of the region bounded between a $\partial u/\partial y$ peak and its adjacent peak closer to the wall. For $p1$, its 'adjacent peak' is defined at the wall. The definitions of U_κ and U_z are illustrated in figure 4.40(b). U_z is equivalent to the modal velocity of the corresponding UMZ. U_κ is always higher than U_z as expected. The difference between U_κ and U_z is smaller at lower ranks of R^s groups, and is smaller at higher Reynolds numbers because the ISLs are more densely distributed at higher Reynolds numbers.

Conditional average velocities are computed across the ISLs as functions of the wall-normal distance from the interface, ξ. By remapping the ISLs in the wall-normal direction, the ISLs are positioned at $\xi = 0$. ξ is defined as positive in the direction towards the pipe centre and negative ξ is pointing towards the wall. Figure 4.41 shows the average streamwise velocity, streamwise fluctuation, and velocity gradient in a wall-normal extent of $\pm 0.1R$ around the ISLs in group R^s_1. The ISLs in this group are the strongest positive shear layers residing the closest to the wall on average. In figure 4.41(a), the shear layer velocity is subtracted from the streamwise velocity. At all Reynolds numbers, the streamwise velocity increases abruptly in the near-vicinity of the ISL. The velocity jumps are steeper around the ISLs at higher Reynolds numbers because the shear layers are thinner at higher Reynolds numbers (de Silva et al. (2017)). These velocity profiles at higher Reynolds numbers are very similar to de Silva et al. (2017) at $Re_\tau = 1200 - 14500$, suggesting that the coherent structures are increasingly similar when the Reynolds number is high. The sudden velocity jump is shown by the velocity gradient against ξ in figure 4.41(c,d). The peak of $\partial U/\partial \xi$ around $\xi \approx 0$ corresponds to the abrupt jump of U across the shear layer. In figure 4.41(c), as the Reynolds number increases, the velocity gradient peaks become higher and sharper for shear layers being stronger and thinner. However, in wall units, the velocity gradients in figure 4.41(d) show that the ISL thickness in group R^s_1 is similar at $\xi^+ = \pm 15$ for all four Reynolds numbers.

The streamwise velocity fluctuation $u^* = U - \langle U \rangle$, denoted with a '$*$' is computed in a different manner from the conventional Reynolds decomposition following Kwon et al. (2014) (their equation (5.2)). The total velocity is subtracted with the conditional averaged U in figure 4.41(a) instead of $\overline{U}$ to show the relative turbulent fluctuation in the frame of reference with respect to the ISLs. In figure 4.41(b),

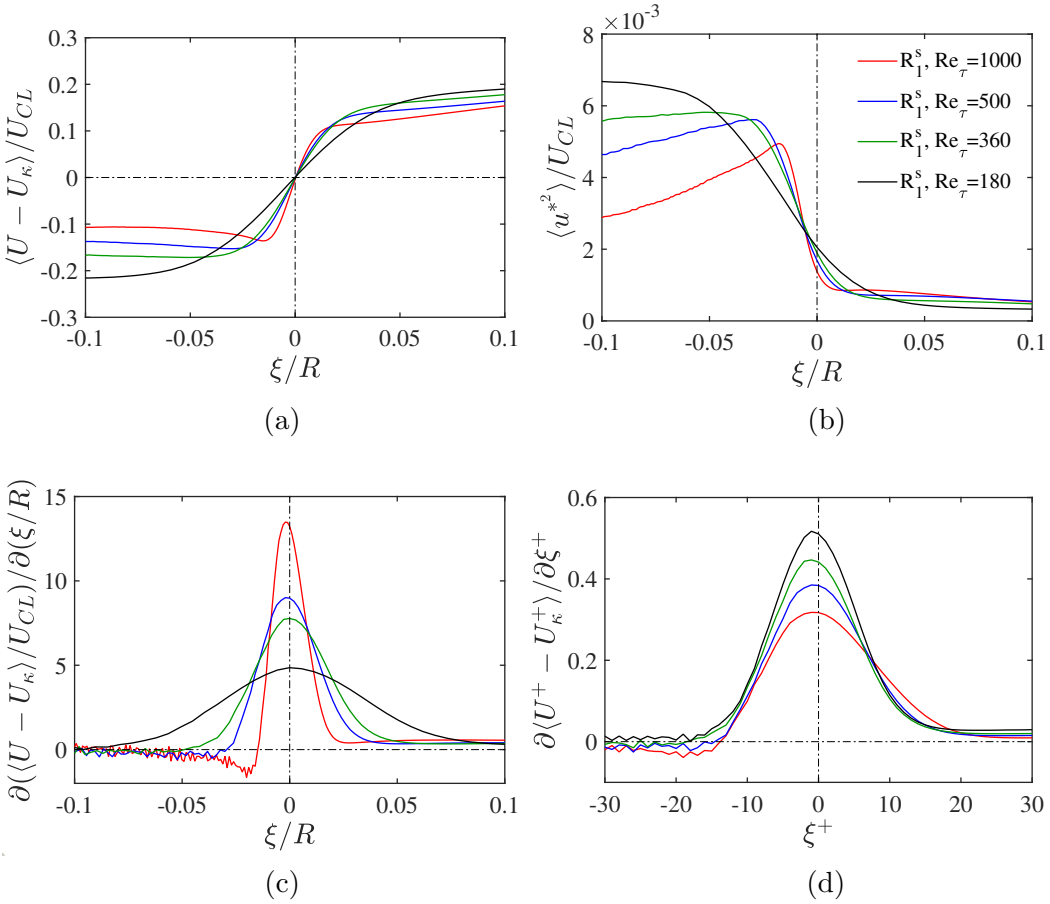

Figure 4.41: Conditional averages as functions of the distance to the internal shear layer at the $\partial u/\partial y$ peaks ξ for (a) streamwise velocity $U - U_\kappa$ where U_κ is the streamwise velocity at the shear layer, (b) streamwise fluctuation u^{*2} where $u^* = U - \langle U \rangle$, (c) velocity gradient of U in (a), $\partial U/\partial \xi$ and (d) $\partial U/\partial \xi$ in wall units for instantaneous internal shear layers in a shear-strength group R_1^s.

the streamwise velocity fluctuation decreases dramatically across the ISLs. The decline of u^{*2} is steeper at higher Reynolds numbers but the difference in velocity fluctuation between the two adjacent UMZs is larger at lower Reynolds numbers. Additionally, for $Re_\tau \geq 360$, u^{*2} shows an increase in the near-wall side ($\xi < 0$) of the ISL before a sudden decrease across the shear layer. This is due to the fact that the R_1^s shear layers at higher Reynolds numbers are located closer to the wall and can capture a sharp increase in $\overline{u^2}$ in the very-near-wall region. This has been observed by Chen et al. (2020) with the UMZ edges residing very close to the wall at $Re_\tau = 500$.

4.5.3 ISL properties as functions of wall-distance

In this section, group averages are computed for the wall-distance group, R^y, where ISLs are ranked by their wall-distance, y_κ. Figure 4.42(a) shows the average wall-distance of the shear layers in each wall-distance group. Group R_1^y has the shear layers closest to the wall and the inset shows that R_1^y is located closer to the wall at higher Reynolds numbers (de Silva et al. (2017)). The skewness of the shear layer wall-distance fluctuation, $\langle \zeta(y_\kappa) \rangle$, is shown in figure 4.42(b). Please note that the skewness was computed with the group mean $\langle y_\kappa \rangle$. Positive ζ is defined as skewness towards larger y_κ, which represents large local ejections, while negative ζ represents large sweeps. The highest skewness towards ejection is exhibited by the most near-wall group R_1^y. The local ejections and sweeps are gradually balanced ($\zeta = 0$) when moving away from the wall, and stronger sweeps over ejections ($\zeta < 0$) are observed further away from the wall. The changeover from ejection-dominance (positive skewness) to sweep-dominance (negative skewness) when moving away from the wall towards the pipe centre is consistent with Chen et al. (2020). The maximum positive skewness, $\zeta(y_\kappa)_{max}$, at R_1^y and the minimum negative skewness, $\zeta(y_\kappa)_{min}$, at the last rank ($R_{N_\kappa}^y$) are summarised in table 4.3. $\zeta(y_\kappa)_{max}$ is always larger than $|\,\zeta(y_\kappa)_{min}\,|$ for all four Reynolds numbers. As the Reynolds number increases, both $\zeta(y_\kappa)_{max}$ and $|\,\zeta(y_\kappa)_{min}\,|$ increase. At $Re_\tau = 180$, $\zeta(y_\kappa)_{max}$ is over 60% stronger than $|\,\zeta(y_\kappa)_{min}\,|$, whereas it is only 30% stronger at $Re_\tau = 1000$. This suggests that the local dominance of large-scale sweep in the pipe centre becomes increasingly stronger at higher Reynolds numbers. The rank with $\zeta(y_\kappa) \approx 0$ which indicates a local balance between ejections and sweeps is highlighted in green in figure 4.42(a-c) from which the wall-normal location of local blowing-sweep balance, $y_{\zeta=0}$, in figure 4.42(c) is estimated. In figure 4.42(c), $y_{\zeta=0}$ fits to a linear relationship with the friction Reynolds number. This suggests that the location where the near-wall ejections and the large-scale sweeping balance with each other is linear to the friction

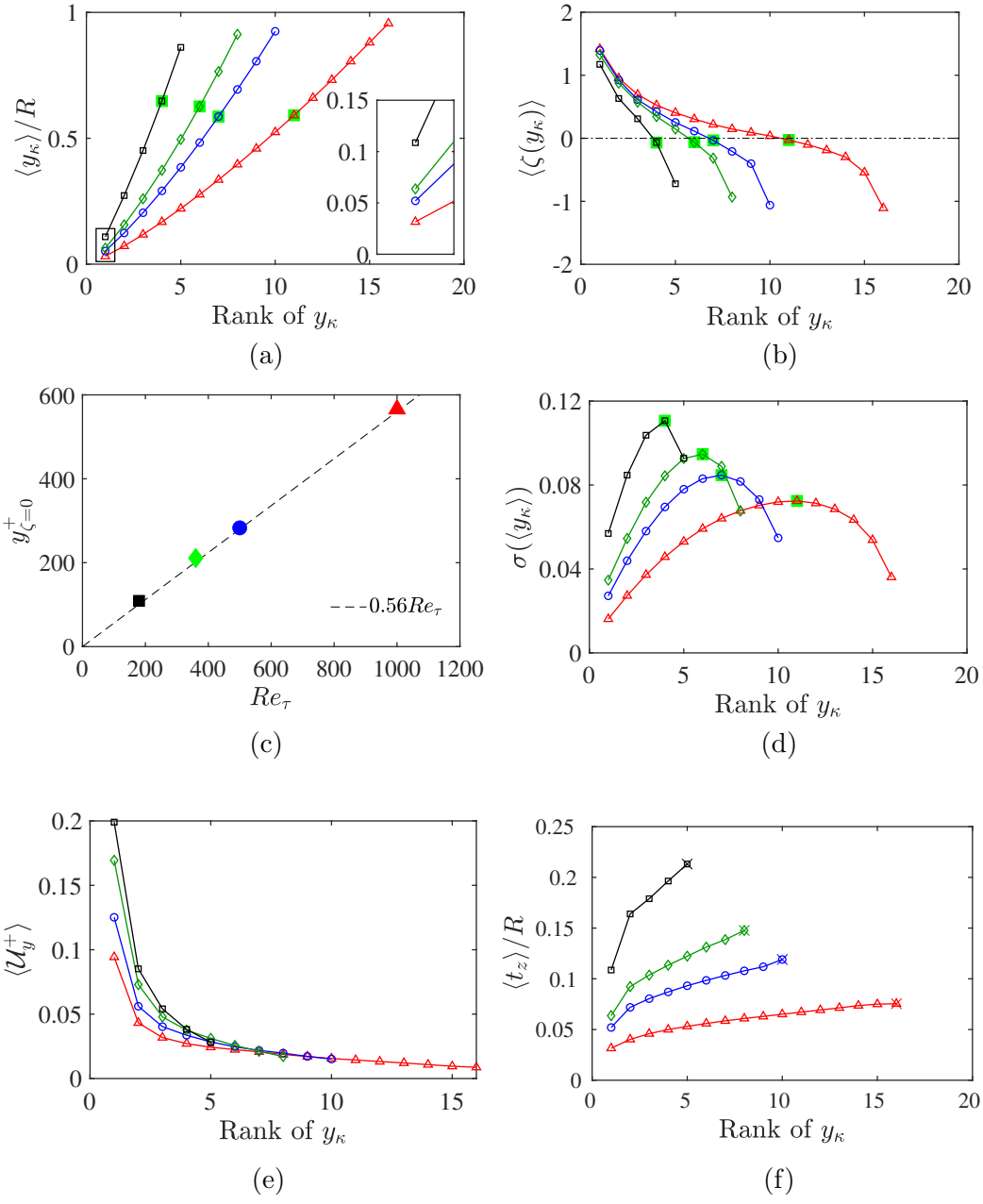

Figure 4.42: (a) Wall-normal location of the peaks on $\partial u/\partial y$, y_κ, (b) skewness of y_κ, $\zeta(y_\kappa)$, (d) standard deviation of y_κ fluctuation, $\sigma(y_\kappa)$, (e) local maximum shear $\mathcal{U}_y$ at the peaks on $\partial u/\partial y$ and (f) zone thickness t_z of the region between a $\partial u/\partial y$ peak and its adjacent peak closer to the wall; averaged within each wall-distance group R^y based on the ranking of y_κ. (c) The average wall-normal location for ISLs with wall-distance fluctuation balanced between ejections and sweeps, $y_{\zeta=0}$ estimated from figure 4.42(a,b) and listed in table 4.3. The symbol highlighted in green at each Reynolds number is the lowest rank with $\zeta(y_\kappa)$ remaining positive in (b). The colours and symbols for different Reynolds numbers follow figure 4.38(a).

Re_τ	$\zeta(y_\kappa)_{max}$	$\zeta(y_\kappa)_{min}$	$\zeta_{max}/(-\zeta_{min})$	$y_{\zeta=0}/R$	$y^+_{\zeta=0}$
180	1.17	-0.72	1.63	0.61	109
360	1.33	-0.93	1.43	0.59	211
500	1.39	-1.06	1.31	0.57	283
1000	1.42	-1.10	1.29	0.57	566

Table 4.3: The maximum skewness of y_κ fluctuation towards ejections, $\zeta(y_\kappa)_{max}$ and towards sweeps, $\zeta(y_\kappa)_{min}$ and the wall-normal location of balanced ejection and sweep ($\zeta(y_\kappa) = 0$), estimated from figure 4.42(a,b).

Reynolds number.

Figure 4.42(d) shows the standard deviation of y_κ in each R^y group. $\sigma(y_\kappa)$ is lower at higher Reynolds numbers since there is a larger number of ISLs in the pipe with less free space to contort. $\sigma(y_\kappa)$ is at the lowest for ISLs closest to the wall and increases monotonically up to the ranks with $\zeta(y_\kappa) \approx 0$, highlighted in green. Beyond $y_{\zeta=0}$ towards the pipe centre, $\sigma(y_\kappa)$ decreases with increasingly stronger local sweeps over ejections. A large $\sigma(y_\kappa)$ indicates that the wall-normal location of the shear layers in a R^y group can vary in a larger wall-normal range. Figure 4.42(e) shows the group average shear strength of the shear layers ranked by their wall-distance. By comparing to the group average $\mathcal{U}_y$ of the shear layers ranked by $\mathcal{U}_y$ (figure 4.39(a)), the shear strength is always positive. This matches with the results in figure 4.39(a) in which the stronger negative shears on average, reside closer to the wall accompanied by positive shears with comparable strength. In a wall-distance group, the relatively rare negative shears are compensated by the positive shears for $\langle \mathcal{U}_y \rangle > 0$. Figure 4.42(f) shows the average distance t_z from a shear layer peak to its adjacent shear layer towards the wall. This is equivalent to the thickness of the adjacent UMZ. The definition of t_z is illustrated in figure 4.40(b) for peaks $p1$ and $p5$. As the number of ISL increases with the Reynolds number, the ISLs are more densely distributed at higher Reynolds numbers (de Silva et al. (2016); Fan et al. (2019)) and also move closer to each other to compensate the new ISLs developed from the near-wall region (Laskari et al. (2018)). This is equivalent to the UMZs demarcated by the ISLs being thinner at higher Reynolds numbers. $\langle t_z \rangle$ increases monotonically from the wall towards the pipe centre, consistent with the hierarchical distribution of UMZ found in the TBL (de Silva et al. (2016, 2017)) and pipe (Chen et al. (2020)).

4.5.4 Three-dimensional structural organisation of ISL

The $3D$ flow fields around the ISLs are computed by volumetric conditional averaging to investigate the large-scale coherent structures around the ISLs. In this section, similar to Gul et al. (2020), only the ISLs in a near-wall region with $0.15 \leq y_\kappa/R \leq 0.2$ are considered. Figures 4.43 and 4.44 show the flow structures at Re_τ = 180 and 1000, respectively. Only the ISLs with shear strength $\mathcal{U}_y > 1.5\langle\mathcal{U}_y\rangle$ are sampled following Gul et al. (2020). $\langle\mathcal{U}_y\rangle$ is the mean shear strength in the selected region which is positive, hence the conditional averaged results are around a positive ISL. Results computed from all ISLs without conditional sampling on $\mathcal{U}_y$ are qualitatively similar, albeit much weaker, to the conditional sampling results.

Figures 4.43(a) and (b) show the iso-surfaces of the streamwise and wall-normal velocity fluctuations and the azimuthal and streamwise vorticities around the average ISL. The location of the ISL in the streamwise and the azimuthal direction is denoted similar to y_κ in the wall-normal direction as x_κ and θ_κ, respectively. The streamwise distance $x - x_\kappa$ from the ISL at $(x_\kappa, \theta_\kappa, y_\kappa)$ is defined as positive in the downstream of the ISL. In figure 4.43(a), the streamwise high- and low-speed structures and their $2D$ projections are displayed in red and blue, respectively. The wall-normal velocity fluctuations (v) in yellow and green indicate regions of sweep ($v < 0$) and ejection ($v > 0$), respectively. The contours of u, v and ω_x on the cross-stream plane at the ISL (the dashed plane in figure 4.43(a,b)) are shown in figure 4.43(c-f). The positive ISLs are bounded between a high-speed streak above and a very strong low-speed streak beneath the shear layer in the wall-normal direction. There is a streamwise elongated prograde azimuthal vortex attached at the bottom of the high-speed streak around the ISL. The low-speed streak is accompanied by another pair of strong high-speed streaks on both sides, which form a triangle of high-speed pathways around the low-speed streak and the ISL. The regions of strong sweep ($v < 0$) also show a triangle distribution surrounding the strong ejection region around the ISL as shown in figure 4.43(f). The top sweep region above the ISL is removed from figure 4.43(a) for a clearer view of all the other structures beneath it. The strong ejection region centred at θ_κ is associated with a pair of counter-rotating streamwise vortices on the sides of the ISL, pumping low-speed fluid from the wall towards the ISL. The organisation of the coherent structures around the ISL is consistent with Gul et al. (2020). Figure 4.44 shows the iso-surfaces and contours of u, v, ω_x and ω_θ at thresholds halved from the Re_τ = 180 case in figure 4.43. A similar organisation of coherent structures around a positive ISL is observed at Re_τ = 1000. The difference is that the pair of high-speed streaks on the sides of the low-speed streak beneath the ISL at Re_τ = 180 disappeared in the figure because they

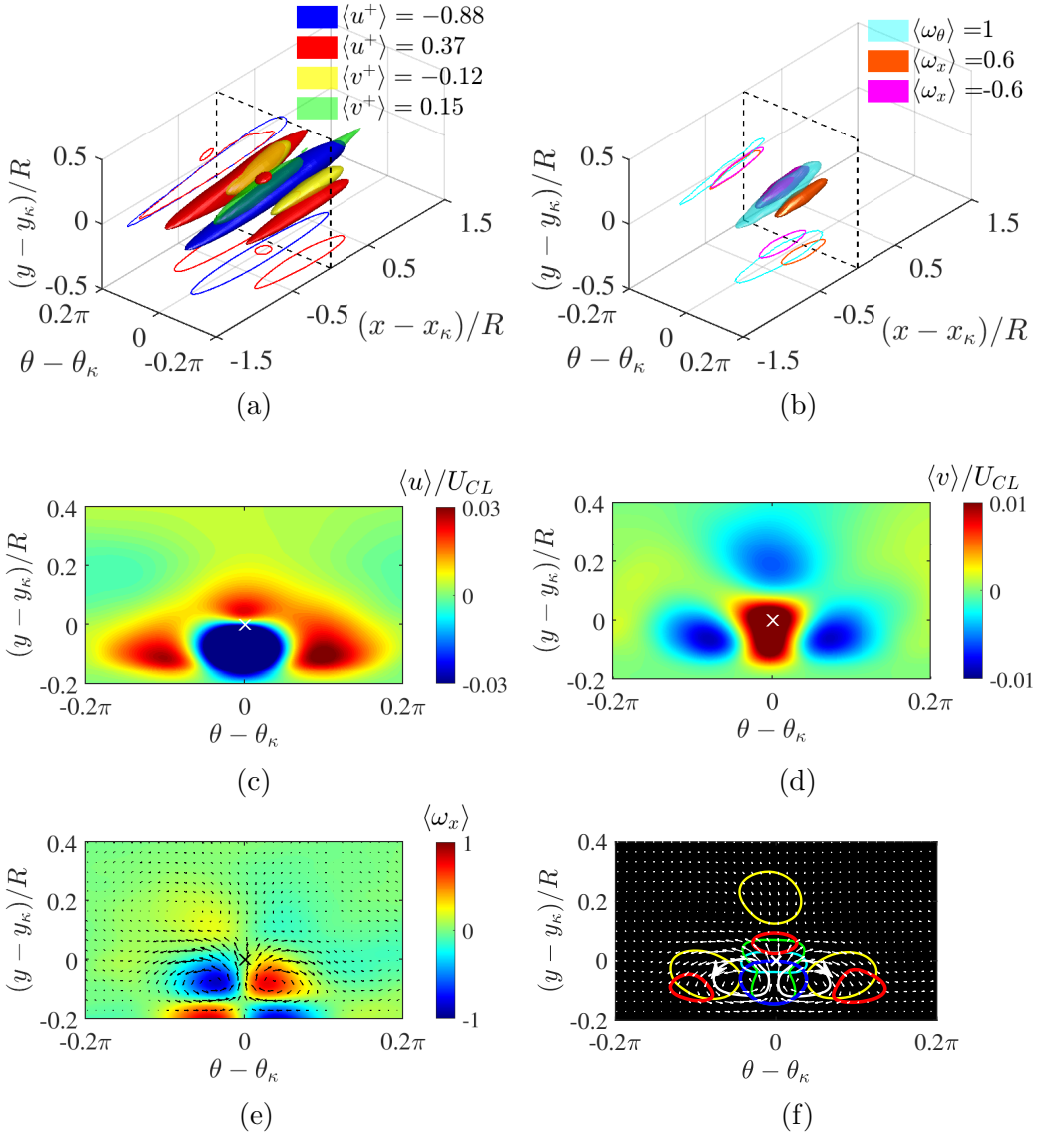

Figure 4.43: Iso-surfaces of (a) the streamwise and wall-normal velocity fluctuations, u and v and (b) the streamwise and azimuthal vorticity, ω_x and ω_θ at Re_τ = 180. The iso-surfaces are plotted in a conditional averaged $3D$ field around the locations with peaked shear in which $x-x_\kappa < 0$ is the upstream of the peaked shear. Contours of (c) u, (d) v and (e) ω_x are plotted on the cross-stream plane at the ISL (dashed plane in (a,b)). (f) shows the contours of u, v and ω_x at the same thresholds and colours as in (a,b) where the arrows on the white contours of $\mid \omega_x \mid$ indicate the swirling direction. Only the shear layers within y/R = 0.15 – 0.2 with $\mathcal{U}_y > 1.5$ times the mean $\mathcal{U}_y$ of ISLs in this region are considered.

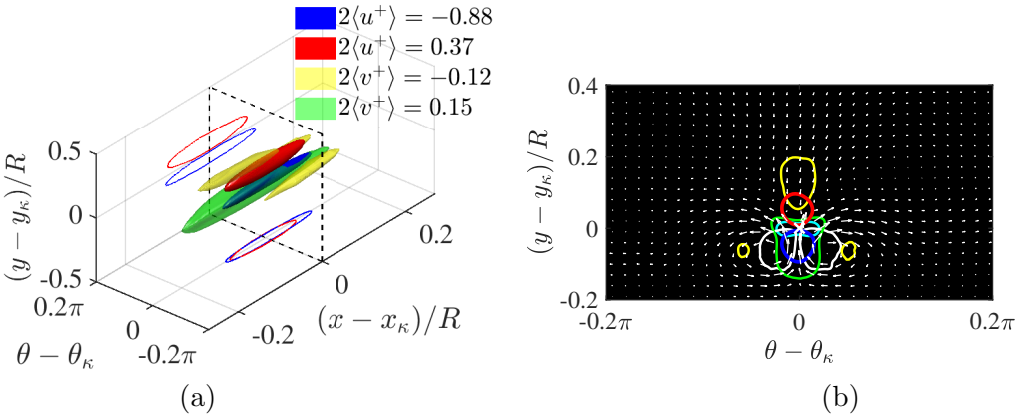

Figure 4.44: (a) Iso-surfaces of the streamwise and wall-normal velocity fluctuations, u and v at $Re_\tau = 1000$ similar to figure 4.43(a). (b) Contours of u, v, ω_x and ω_θ at the same thresholds and colours as in figure 4.43(a). Only the shear layers within $y/R = 0.15 - 0.2$ with $\mathcal{U}_y > 1.5$ times the mean $\mathcal{U}_y$ of ISLs in this region are considered.

are significantly weakened. The high-speed streak on the top of the ISL becomes much stronger at $Re_\tau = 1000$. This high-speed streak is also significantly more elongated in the streamwise direction at $Re_\tau = 1000$, shown by its $2D$ projections. Comparing figure 4.43(f) and figure 4.44(b), the strong sweep region above the ISL becomes significantly larger than the sweep regions on the sides of the ISL at higher Reynolds numbers.

To investigate the negative shear layers, conditional averaged $3D$ fields are computed around the ISLs with $\mathcal{U}_y < 0$. The layout of figure 4.45 is similar to figure 4.43. The results show that an average negative ISL is formed with a opposite structural organisation compared with the positive shears. Around a negative shear layer, the high- and low-speed streaks, the sweeps and ejections are exchanged in position; the negative ISL and the strong sweeping at the ISL are surrounded by triangles of low-momentum pathways and ejections. The region of strong prograde vorticity below the high-speed streak in Fig. 4.43(f) is shifted away from the ISL towards the wall with the high-speed streak. The swirling direction of the vortex pair on the sides of the ISL is also reversed which results in a strong sweeping region around the ISL. The reversed flow mechanism around the positive and the negative shear layers is shown in a schematic drawing in Fig. 4.46(a). The positive shear layer is ejected to a bulge shape and the negative shear layers is at the valley due to the sweeping at the ISL.

The thickness of the ISLs is measured by the width of the $\partial u/\partial y$ peaks, p_w of which definition is illustrated in Fig. 4.46(b). The width of a $\partial u/\partial y$ peak is

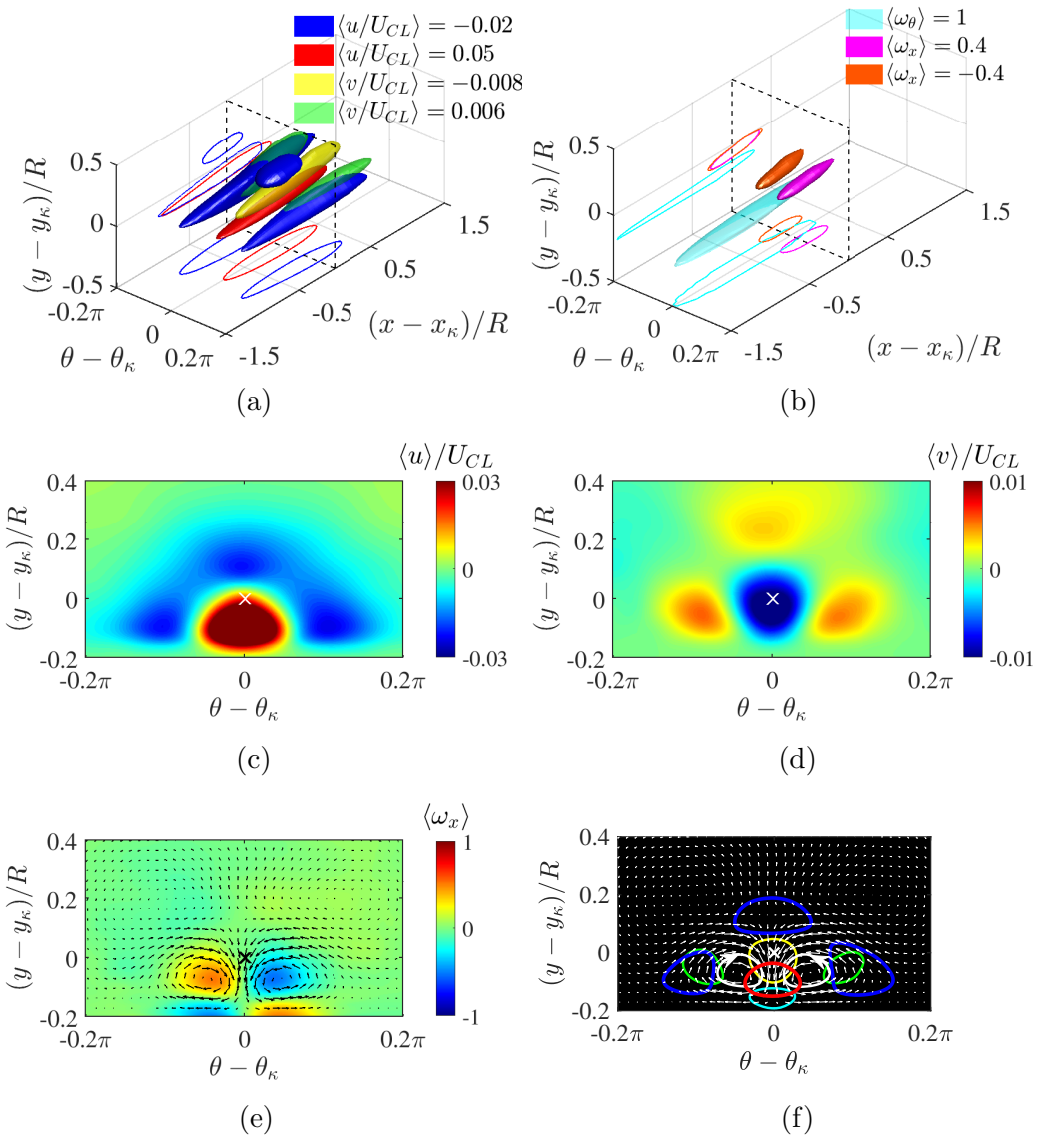

Figure 4.45: Iso-surface and contours of u, v, ω_x and ω_θ in the $3D$ conditional average field around the negative ISLs, arranged similar to figure 4.43. Only the negative shear layers ($\mathcal{U}_y < 0$) within $y/R = 0.15 - 0.2$ are considered.

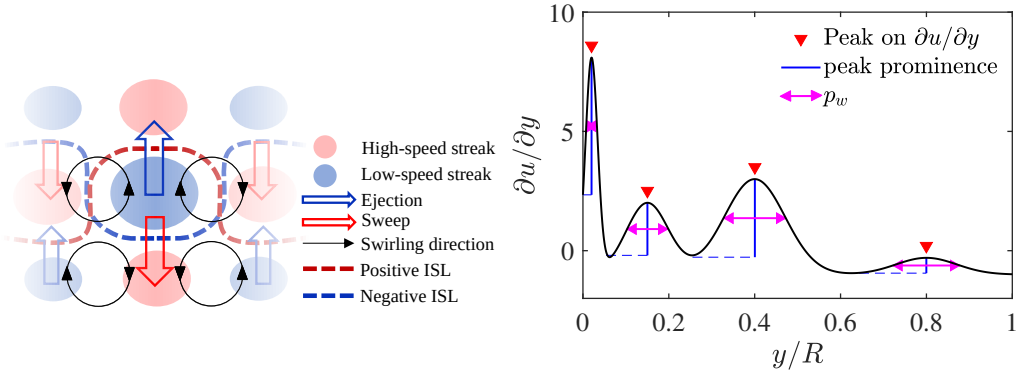

(a) (b)

Figure 4.46: (a) Schematic cross-stream structure organisation around a positive and a negative internal shear layer. (b) Illustration for the definition of the prominence and width p_w at the half-prominence of $\partial u/\partial y$ peaks.

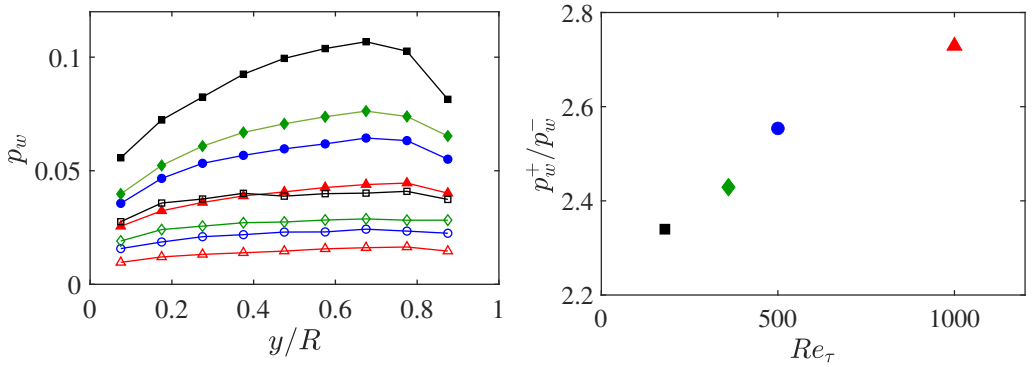

(a) (b)

Figure 4.47: (a) Average width p_w of $\partial u/\partial y$ peaks at the peaks' half prominence against the wall-distance, for positive shears (solid symbols) and negative shears (empty symbols). (b) The average ratio of p_w of the positive shear layers to p_w of the negative shear layers.

measured at the middle of the peak's prominence which is defined from the peak to its nearest local minimum towards the wall. p_w is similar to the UMZ interface thickness estimated as $\Delta U/\mathcal{U}_y$ at the interface in Kwon et al. (2014) which represent the abruptness of the streamwise velocity jump across the shear layer. Fig. 4.47(a) shows p_w as functions of the wall-distance for ISLs averaged in regions with an increment of $0.1R$ from y/R = 0.05 to 0.95, computed for the positive and negative shears separately. The shear layers are always thinner at higher Reynolds numbers naturally because the number of ISL increases with Reynolds number. The positive ISLs increase in thickness with increasing wall-distance until reaching close to the centreline where p_w starts to decrease. The wall-normal location for positive ISLs being the thickest on average is approximately at y/R = 0.7. The negative shear layers at all wall-distance are significantly thinner than the positive shear layer at all Reynolds numbers. The average ratio of the positive shear layer thickness to negative shear layers in Fig. 4.47(b) shows that the negative shear layers are more than two times thinner than the positive shears on average, and is increasingly thinner at higher Reynolds numbers.

4.6 Summary

In this chapter, the large-scale coherent structure, the quiescent core, the uniform-momentum zones (UMZ) and the internal shear layers (ISL) in turbulent pipe flow were investigated for four Reynolds numbers, Re_τ = 180, 360, 500 and 1000. The UMZs and ISLs were identified using three PDF-based methods in table 2.2: double-PDF, constrained peak detection and kernel density estimation; and a new ISL-based method which direct seek for locally peaked shears without any ad-hoc filter. The number of UMZs and ISLs in the flow fluctuates increasingly with Reynolds number. The average number of UMZs increases with Reynolds number and shows an excellent fitting to $0.1Re_\tau^{0.74}$. The UMZs identified by the four different method showed consistent characteristics. The characteristics are also qualitatively similar to the UMZs reported for the channels and TBL: the UMZs and the ISLs demarcating them form a hierarchical distribution, being thinner when nearer the wall; the step-like velocity jump and concentrated azimuthal/spanwise vortices at the ISL were observed in conditional average results. The conditional averaged results also suggest that the flows in the pipe are quantitatively more similar to the channel than to TBL.

The contortion of the continuous ISLs, i.e., UMZ interfaces manifests of the high- and low-momentum streaks of the streamwise velocity fluctuation. The faster-travelling UMZs away from the wall is representative for the LSMs while the UMZs in the near-wall region captures the small-scale velocity fluctuation of the near-wall cycle. The level of ISL contortion in the wall-normal direction increases with increasing wall-distance in both $2D$ (the streamwise and spanwise directions) and $3D$. The $2D$ meandering of the UMZ interface in the azimuthal direction is found to be always more intense than in the streamwise direction.

The skewness between the bulges and the valleys on the $3D$ UMZ interface manifests the local imbalance between upward ejections of low-speed fluids and downward sweeps of high-speed fluids. Near the wall, the interface is significantly biased to the bulges, matching the asymmetry of the large-scale modulation on the near-wall activities reported by Agostini and Leschziner (2014). When the interface departs away from the wall, the asymmetry decreases to a local balance between ejections and sweeps. The UMZs distant from the wall, travelling faster than the centreline velocity even show opposite asymmetry for locally more amplified sweeps over ejections. The wall-normal location of the local balance between ejections and sweeps, i.e., minimum interface skewness showed no clear Reynolds number dependence, located at $y/\delta \approx 0.55 - 0.6$ at all four Reynolds numbers. The fourth-order

kurtosis of the fluctuating interface wall-normal location are computed separately for the bulge and the valley part of the UMZ interfaces. The small-scale near-wall ejections can achieve twice spikier than the sweeps. This becomes the opposite in the centre half of the pipe where the sweeps are found spikier than the ejections. The biased skewness and kurtosis between ejections and sweeps show the difference between the large-scale and the small-scale structures.

There exists a non-negligible amount of negative shear layers in the flow with adverse velocity gradients ($\partial u/\partial y < 0$). The shear strength of both the positive and the negative shear layers increases towards the wall. The $3D$ coherent structures around the ISLs in the near-wall region is obtained via volumetric conditional averaging. A positive shear layer is located between a high-speed streak above and a strong low-speed streak beneath the shear layer on average. The low-speed streak is associated with a pair of counter-rotating streamwise vortices which results in a large region of strong ejection of low-speed fluid around the ISL. Additionally, there is concentrated azimuthal rotation elongated in the azimuthal direction below the high-speed streak around the shear layer. The structure distribution is reversed around the average negative shear layer. The high- and low-speed streaks, and the ejections and sweeps are exchanged in position. The elongated azimuthal swirling at the bottom of the high-speed streak shifts away from the shear layer. The swirling direction of the vortex pair are reversed so that the negative shear layer is surrounded by a large sweep region. With the same wall-distance, the average thickness of the positive shear layers is significantly larger than the negative shear layers and the positive shear layers are increasingly thicker than the negative shear layers on average when Reynolds number increases.

Chapter 5

DNS of non-Newtonian turbulent pipe flow

This chapter investigates shear-thinning non-Newtonian fluids flow in the pipe at a low Reynolds number, $Re_\tau \approx 180$. The DNS shares the same computational set-up of the Newtonian pipe flow at $Re_\tau = 180$ in table 3.1. For incompressible non-Newtonian fluids with variable viscosity μ and $\nabla \cdot \mathbf{u} = 0$, the viscous force, $\nabla \cdot \boldsymbol{\tau}$ in the momentum equation is solved as

$$\nabla \cdot \boldsymbol{\tau} = \frac{\partial \tau_{ij}}{\partial x_j} = \frac{\partial}{\partial x_j}\left(\mu\left(\frac{\partial u_i}{\partial x_j} + \frac{\partial u_j}{\partial x_i}\right)\right). \tag{5.1}$$

5.1 Modelling of shear-thinning fluids

The shear-thinning behaviour of the fluid is modelled by the power-law rheology in equation (5.2) where μ is the apparent viscosity, K is the flow consistency, n is the power-law index and $\dot{\gamma}$ in equation (5.3) is the shear rate. When $n = 1$, the fluid is Newtonian; $n < 1$ indicates shear-thinning and $n > 1$ indicates shear-thickening.

$$\mu = K\dot{\gamma}^{n-1} \tag{5.2}$$

$$\dot{\gamma} = \sqrt{2S_{ij}S_{ij}} \tag{5.3}$$

With variable viscosity, the flow cannot be characterised by a constant Reynolds number. In the simulation, a generalised Reynolds number in equation (5.4) is

n	Re_τ	Re_g
0.5	180	5339
0.69	185	5501
0.75	186	5514

Table 5.1: DNS parameters of present non-Newtonian pipe flow using the power-law rheology model.

applied to the near-wall region.

$$Re_g = \frac{\rho U_b D}{\mu_w} \tag{5.4}$$

$$\mu_w = K^{1/n} \frac{\tau_w}{\tau_w^{1/n}} \tag{5.5}$$

The iterative procedure of the simulation is illustrated in figure 5.1. By setting the near-wall Reynolds number Re_g, the bulk mean velocity U_b, the wall shear stress τ_w, the near-wall viscosity μ_w in equation (5.5), the axial pressure gradient dp/dx and K are updated at each time-step to maintain the flow at Re_g. Table 5.1 shows the parameters of the three power-law shear-thinning cases with $n = 0.5, 0.69, 0.75$. These three power-law indices were also used in Rudman et al. (2004). The data of the Newtonian pipe flow ($n = 1$) at $Re_\tau = 180$ is also investigated with the non-Newtonian cases for comparison.

5.2 Turbulent statistics and flow structure

5.2.1 The mean flow statistics

Figure 5.2 shows the inner-scaled mean velocity profile of U. All three non-Newtonian cases show good agreement to the DNS results by Rudman et al. (2004) using the same rheology model. The results generally agree with Bogue and Metzner (1963) which showed that the deviation of turbulent profiles of non-Newtonian fluids from Newtonian fluids with an inverse proportion to n. In the viscous sublayer, all the mean velocity profiles obey $U^+ = y^+$ as expected since the near-wall Reynolds number is maintained throughout the simulation. The non-Newtonian mean velocity profiles only start to show difference from the Newtonian case above $y^+ > 20$. As n decreases, the profiles of U further deviate from the Newtonian case. For the most shear-thinning case of $n = 0.5$, U is developing to a parabola laminar profile because the flow is no longer fully turbulent, which will be discussed in the later results.

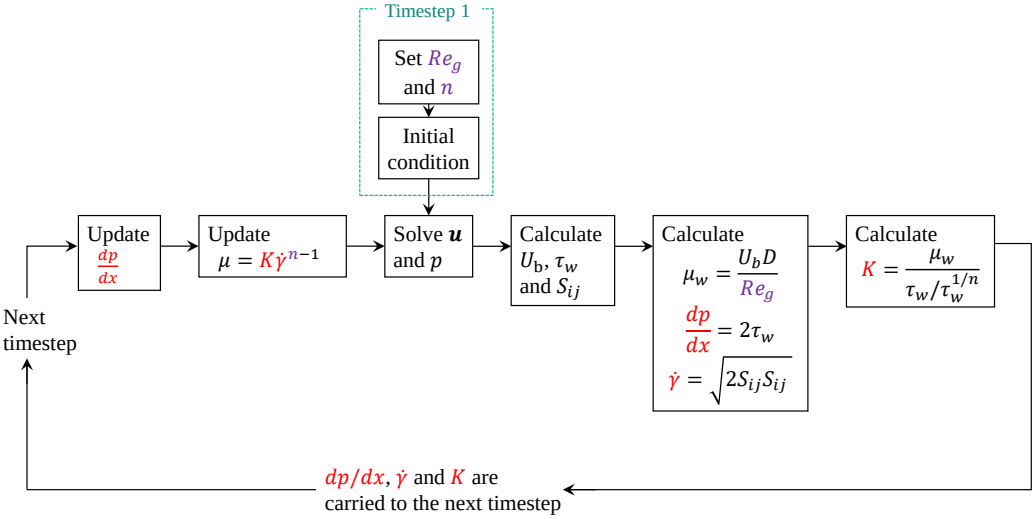

Figure 5.1: DNS iteration procedure for maintaining generalised Reynolds number Re_g near the wall in non-Newtonian fluids.

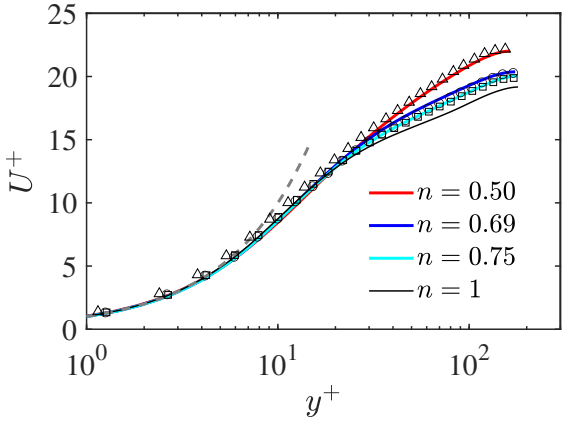

Figure 5.2: Mean velocity profiles $\overline{U}$ of the present pipe flow at power-law index n = 0.5, 0.69, 0.75 and 1 (Newtonian). Symbols are the corresponding results by Rudman et al. (2004) as listed in table 2.5: '△', n = 0.5; '○', n = 0.69; '□', n = 0.75.

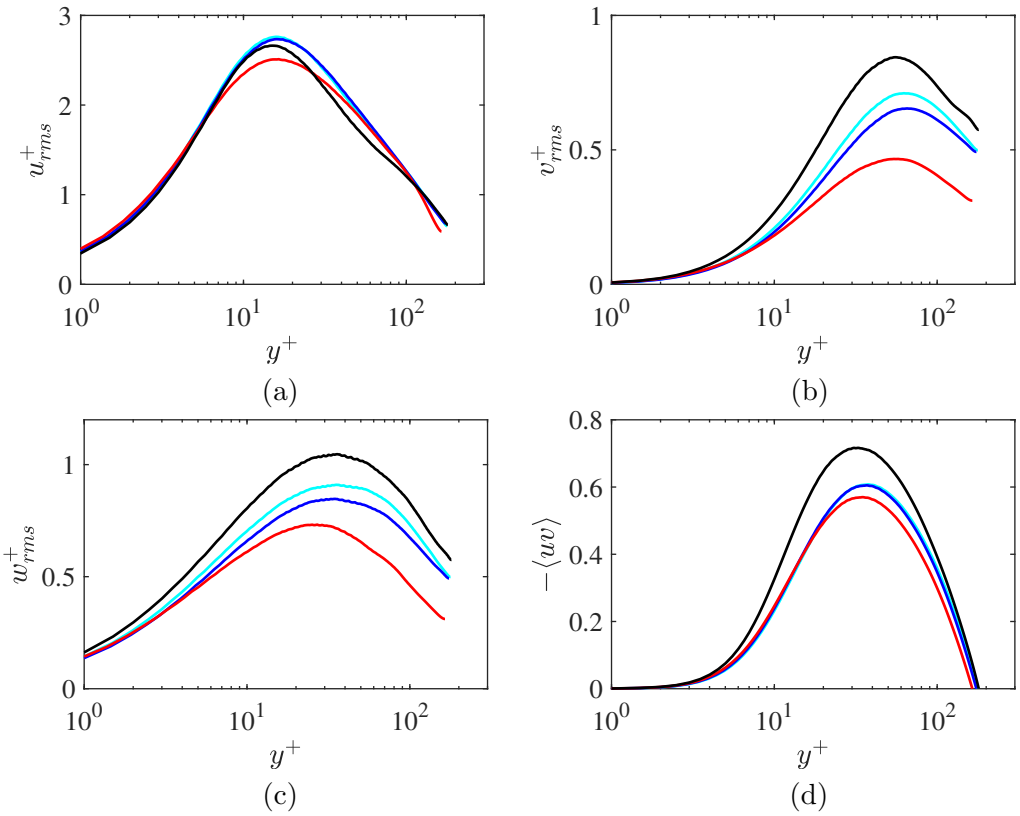

Figure 5.3: Root-mean-square of (a) the streamwise fluctuation u, (b) the wall-normal fluctuation v and (c) the azimuthal fluctuation w. (d) The mean Reynolds shear stress $-uv$. The legend follows figure 5.2.

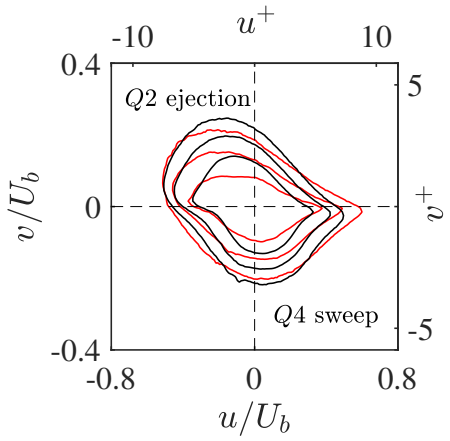

Figure 5.4: Joint PDF of the velocity fluctuations for the Newtonian ($n = 1$, black) and non-Newtonian fluid ($n = 0.5$, red) on the $u - v$ plane with quadrant turbulence structure classification.

Figure 5.3 shows the inner-scaled root-mean-square (RMS) velocities and Reynolds shear stress, $-uv$ of the four cases. The RMS velocities of different cases show more substantial discrepancies in the wall-normal and azimuthal directions. In figures 5.3(b) and (c), the peaks of v_{rms} and w_{rms} decrease with smaller n. The lowering of off-axis fluctuation as the flow becomes more shear-thinning has been reported by Pinho and Whitelaw (1990); Nouri et al. (1993); Escudier and Presti (1996); Draad et al. (1998); Rudman et al. (2004) and Gavrilov and Rudyak (2016). The two relatively less shear-thinning cases of n = 0.75 and 0.69 are statistically very similar especially for u_{rms} and $-\overline{uv}$. The streamwise RMS velocity of the non-Newtonian cases can exceed the non-Newtonian case, even the most non-Newtonian case (n = 0.5) has u_{rms} marginally higher than the n = 1 case for $y^+ > 30$, matching the observations by Peixinho et al. (2005) and Rudman et al. (2004). Mathematical explanation for the excess in u_{rms} is that as the flow becomes more shear-thinning, the streamwise fluctuation u has a larger standard deviation, i.e., the occurrence of extreme outliers in u increases. For further investigation, figure 5.4 shows the joint PDF of the streamwise and wall-normal velocity fluctuations, u and v for the Newtonian and the most non-Newtonian (n = 0.5) case. The quadrants categorize the Reynolds stress activities as labelled in figure 5.4 based on the sign of u and v (Wallace et al. (1972); Lu and Willmarth (1973)). The PDF indicates strong $Q2$ ejection and $Q4$ sweep events with positive contribution to Reynolds shear stress than the $Q1$ inward and $Q3$ outward motions which contribute negative Reynolds shear stress (Lozano-Durán et al. (2012)). The contours of the non-Newtonian case are stretched along v = 0 towards $u >> 0$, so the range of u is larger and the range of v is smaller as n decreases. The increase in the extremely large streamwise fluctuations is accompanied with lowered wall-normal fluctuations, which correspond to the results in figure 5.3 and explains the marginal excess in the streamwise RMS velocity in non-Newtonian fluids.

The results so far suggest that the non-Newtonian flows have some high-speed streamwise surge with local acceleration which may be more clearly observed in the contours of u. Figure 5.5 shows the wall-parallel contours of u at y/R = 0.1, roughly where the u_{rms} peaks are located. The top contour of the Newtonian fluid shows a fully-developed turbulence with the signature near-wall streaks of high- and low-momentum pathways in a homogeneous distribution. As n decreases, the streaks become flatter, longer and wider. These turbulent structures become less homogeneous, weaken and even disappear in some regions. At n = 0.69, there are regions (circled regions) where the flow is clearly on the verge of local laminarisation and can hardly be fully-developed. Such local laminarisation is more obvious in the

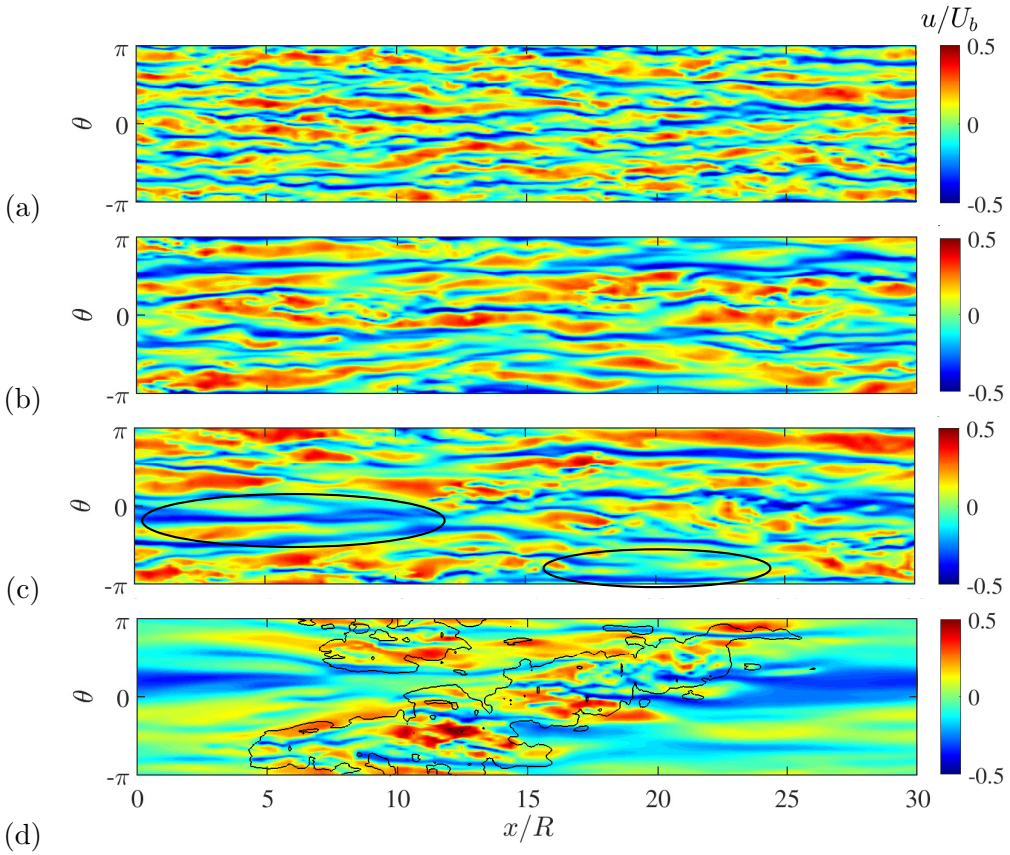

Figure 5.5: Contours of the streamwise velocity fluctuation u on a streamwise-azimuthal plane at a fixed wall distance of $y = 0.1$ for flows with power-law index (a) $n = 1$ (Newtonian), (b) $n = 0.75$, (c) $n = 0.69$ and (d) $n = 0.5$.

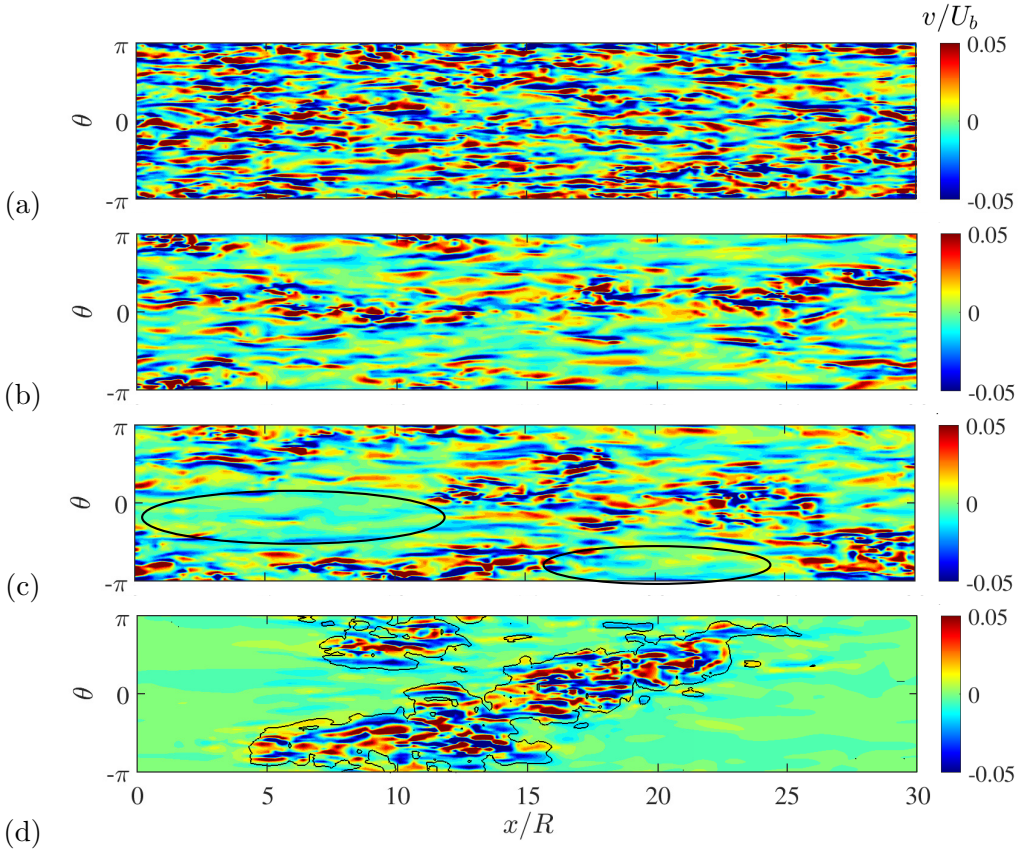

Figure 5.6: Contours of the wall-normal velocity fluctuation v on a streamwise-azimuthal plane at a fixed wall distance of $y = 0.1$ for flows with power-law index (a) $n = 1$ (Newtonian), (b) $n = 0.75$, (c) $n = 0.69$ and (d) $n = 0.5$.

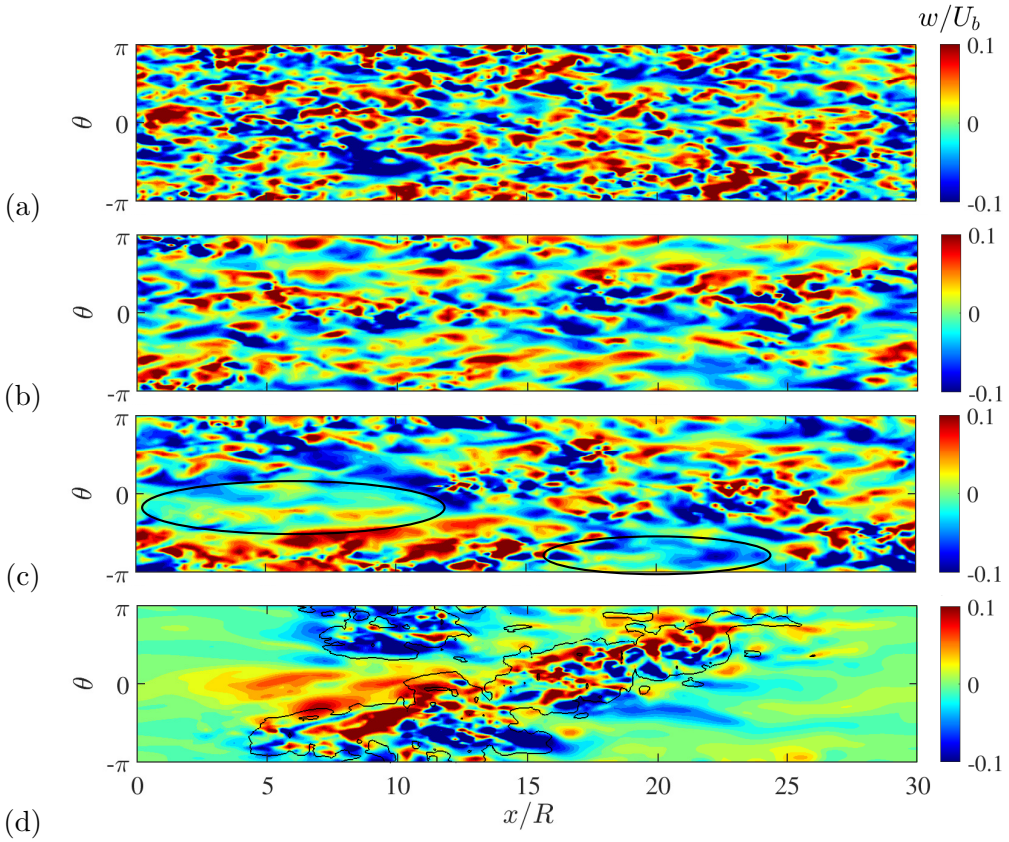

Figure 5.7: Contours of the azimuthal velocity fluctuation w on a streamwise-azimuthal plane at a fixed wall distance of $y = 0.1$ for flows with power-law index (a) $n = 1$ (Newtonian), (b) $n = 0.75$, (c) $n = 0.69$ and (d) $n = 0.5$.

contours of the off-axis fluctuations in figures 5.6 and 5.7. In these regions, the off-axis fluctuations are critically lowered, particularly for the wall-normal fluctuation v, so that the three-dimensional nature of turbulent activities is vanishing. The velocity fluctuations in these regions may be more appropriate to be characterised by the pre-transition laminar fluctuations by Mayle and Schulz (1997) which were found almost all contained in the streamwise component, rather than fully $3D$ turbulent fluctuations.

The bottom contours in figures 5.5, 5.6 and 5.7 for case $n = 0.5$ show a fundamental difference from the other non-Newtonian cases. The flow is spatially inhomogeneous which is an important feature of turbulent transition (Tuckerman et al. (2020)). The flow is already intermittent, showing features of turbulent spots which are indicative of transitional flow (Wygnanski and Champagne (1973); Hof et al. (2005)). The outline of the turbulent spot approximately extracted from the off-axis fluctuation using v in figure 5.6 is mapped on the streamwise fluctuation contour in figure 5.5(d), and there is a clear strong low-speed streak in the upstream and downstream of the turbulent spot. This feature (also found to be presence in other snapshots) resembles the wavy instability in the early stage of turbulent transition which was observed as transient unstable travelling waves in front of the trailing laminar/turbulent interface of the turbulent slugs. These laminarising regions in the non-Newtonian cases are referred as pseudo-laminar region in the later part of this study.

Cross-stream contours of the instantaneous streamwise velocity U and its derivative $\partial U/\partial y$, the streamwise fluctuation u, and Q in equation 2.6 are plotted for the $n = 0.5$ case in figure 5.8, using the same snapshot as in figures 5.5-5.7. Three streamwise locations were selected: $x = 0$ where the flow is very quiescent, $x/R = 10$ where the flow is intensively turbulent and $x/R = 20$ for a mixture of both. The difference between the pseudo-laminar region and the turbulent region is very distinguishable; the pseudo-laminar flow at $x = 0$ shows remarkably uniform U and $\partial U/\partial y$ in the azimuthal direction and hardly shows any intense vortical structures in Q. In the contours of Q at $x/R = 10$ and 20, the majority of the strong vortical structures are confined near the wall while the flow is rather quiescent in the pipe core where viscosity is higher for shear-thinning fluids. The results in general, agree with that transition is delayed in shear-thinning fluids (Pinho and Whitelaw (1990); Draad et al. (1998)). The $n = 0.5$ case was intentionally run for a very long time compared to the other cases and it was found that the flow was never fully-developed or fully laminarised.

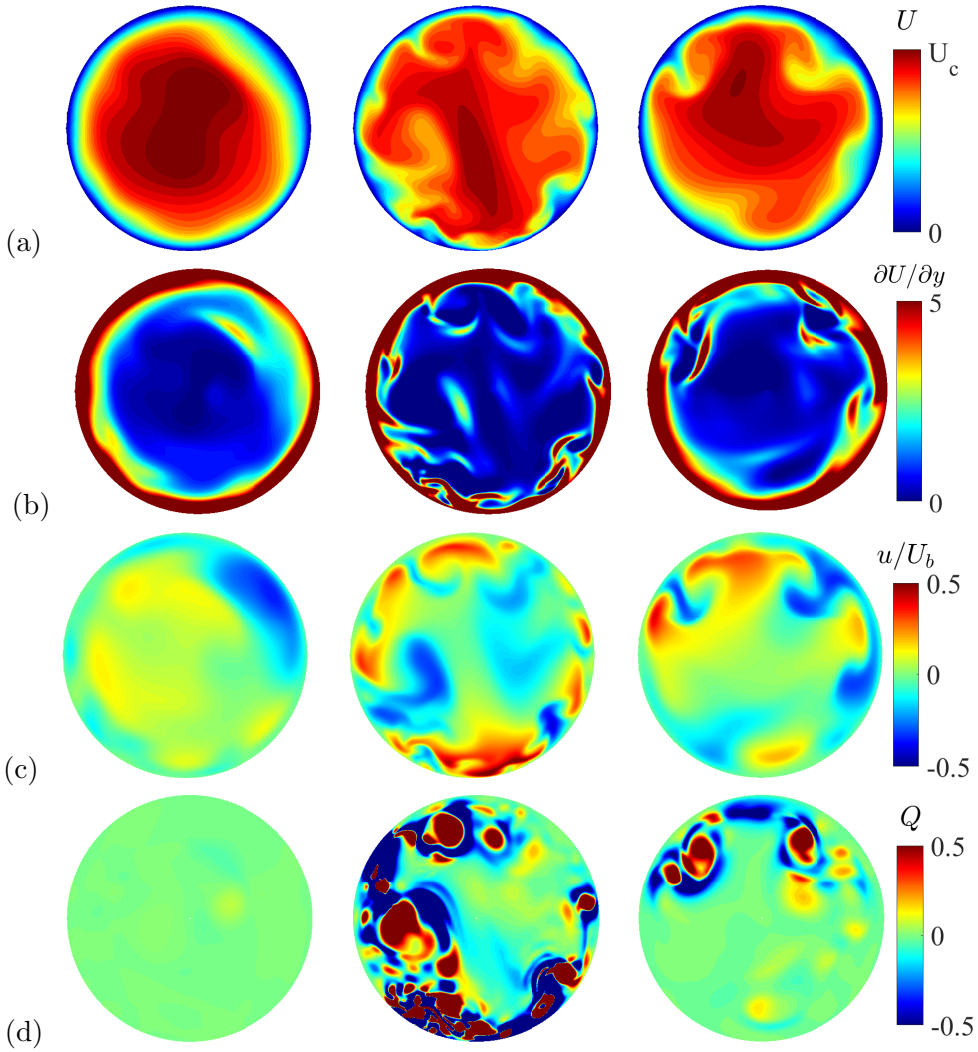

Figure 5.8: Cross-stream contours of (a) the streamwise velocity U, (b) the velocity gradient $\partial U/\partial y$, (c) the streamwise fluctuation u and (d) scaler Q as in equation (2.6) for the non-Newtonian case of $n = 0.5$. The contours are plotted at three streamwise location: $x = 0$, 10 and 20. Each contour corresponds to the colour axis on its right-hand side.

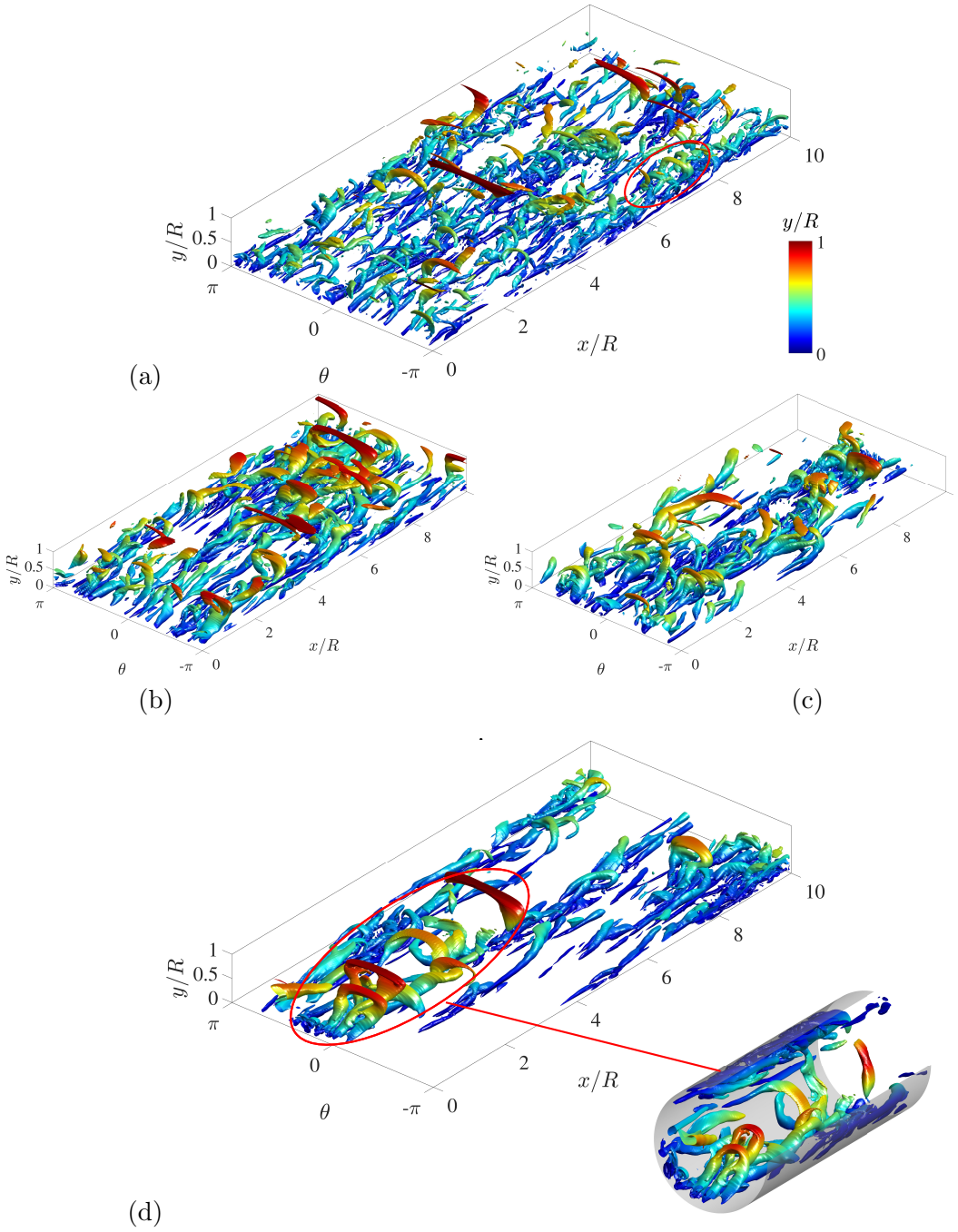

Figure 5.9: Iso-surfaces of Q in 1/3 of the streamwise pipe domain for flows with power-law index (a) $n = 1$, (b) $n = 0.75$, (c) $n = 0.69$ and (d) $n = 0.5$. The threshold used is $Q = 0.5$ for the non-Newtonian cases in (b-c) and $Q = 2$ for the Newtonian case in (a). Case $n = 0.5$ is additionally shown with the wrapped view in the pipe.

5.2.2 Hairpin vortices in non-Newtonian fluids

Figure 5.9 shows the $3D$ tube- or worm-like vortical structures in the pipe using the Q-criterion. The iso-surfaces of Q in equation (2.6) represent regions with local excess of swirling over straining. The structures are coloured by their wall-normal elevation, so that one can observe the blue small-scale near-wall structures and the red large-scale structures away from the wall. The difference in the turbulence structures between Newtonian and non-Newtonian fluids reported in the literature is apparent. Since the turbulent structures are weakened and two- or even one-dimensionalised as n decreases, it is expected that the Q-space is increasingly filled by regions absent of vortical structures.

In the Newtonian case, as it has been suggested by many studies of wall-bounded flows (Theodorsen (1952); Kline et al. (1967); Townsend (1976); Head and Bandyopadhyay (1981)), the near-wall quasi-streamwise vortices are inclined and attached to the wall, forming trains of eddies. Zhou et al. (1999) and Adrian et al. (2000) reported that these vortices, known as the horse-shoe or hairpin vortices, travel in packets in which the leading vortices regenerate new hairpins downstream. However, in reality, these vortical structures and their packets can rarely sustain the idealised quasi-streamwise symmetry due to the complex multi-scale interactions. Figure 5.9(a) indeed shows that these quasi-streamwise vortices are predominantly asymmetric in a cane-like form in the Newtonian fluid. The most intact hairpin-form structures (highlighted in figure 5.9(a)) are confined relatively near the wall, whereas in the outer region where large scales dominate, the vortex loops are shattered and becomes very irregular. Once the large-scale turbulent motions away from the wall gradually vanish in the shear-thinning fluids, the vortical structures instantly show a very different profile. At $n = 0.75$, majority of the vortex loops are preserved in the outer region and the overall structural organisation is remarkably less scattered. However, there is no clearly identifiable separate packets at $n \geq 0.69$. In figure 5.9(d) for the most shear-thinning case of $n = 0.5$, there is a clear packet of four intact and highly symmetric vortex loops, streamwise aligned, exceedingly well-preserved to resemble the model of an ideal vortex packet with streamwise size growth by Adrian et al. (2000). We believe that the wholeness of the packet is because of that it is unobstructed due to that the pseudo-laminar regions near the packet have no strong turbulence structures for structure interaction. The observations in figure 5.9 are the opposite to Zhen et al. (2013) who suggested that the delay in turbulence transition in shear-thinning fluids flow in the channel was caused by the breaking down and weakening of hairpin vortices.

5.2.3 Streamwise streaks spacing

It is also observed from figures 5.5 and 5.9 that the streamwise streaks are wider and the vortex tubes are thicker in the shear-thinning fluids. For Newtonian fluids, the average spacing is approximately 100 wall units between two neighbouring high- or low-momentum streaks (Kim et al. (1987)). Figure 5.10(a) shows the spanwise two-point correlation of the streamwise velocity near the wall at $y^+ = 10$,

$$R_{uu} = \frac{\sum_{i=1}^{N-k}(u_i - \overline{u})(u_{i+k} - \overline{u})}{\sum_{i=1}^{N}(u_i - \overline{u})^2}, \tag{5.6}$$

where N is the signal length and k is the lag. The separation between adjacent high- or low-speed streaks, λ_θ are estimated by the distance between the two minima of R_{uu} at the sides of $R\theta = 0$. For the $n = 0.69$ and $n = 0.5$ case, as the organised structures become less dominant, R_{uu} is 'corrupted' by the large regions of pseudo-laminar flow and decreased population of streaks. Thus, instead of the minimum of R_{uu}, λ_θ for case $n = 0.69$ and $n = 0.5$ is estimated by the distance between the nearest local minima of R_{uu} on the sides of $R\theta = 0$.

The average streak spacing is plotted as a function of the wall-distance up to half of the pipe radius in figure 5.10(b). The streak spacing increases with the distance from the wall. Results of the Newtonian case are in accordance with the experimental results by Smith and Metzler (1983) and the DNS results by Kim et al. (1987). In the viscous sublayer, λ_θ is almost equal for $n = 0.69$ and $n = 0.75$ and gradually differentiate from the buffer layer to the outer region. The $n = 0.5$ case is distinguished with a larger streak spacing throughout the viscous wall region to the outer region, which again, indicates the fundamental difference between the $n = 0.5$ case and the other two shear-thinning cases. As the flow becomes more shear-thinning, the near-wall streaks have azimuthal spacing increase as reported by Singh et al. (2017).

5.3 Topology of non-Newtonian pipe flow

The joint PDFs of the velocity-gradient tensor (VGT) invariants in the $Q - R$, $Q_\omega - Q_s$, $Q_s - R_s$ and $Q_\omega - R_\omega$ space are computed for the whole domain and in separate regions: the viscous sublayer ($y^+ \leq 5$), the buffer layer ($5 < y^+ < 30$) and the outer region ($y^+ > 50$). For flows at such a low Reynolds number, strictly there is no logarithmic region as the mean velocity profiles (figure 5.2) do not converge to the log law (Moser et al. (1999); Ahn et al. (2013)), and is even more so for the shear-thinning cases. Therefore, the three defined regions may only provide an

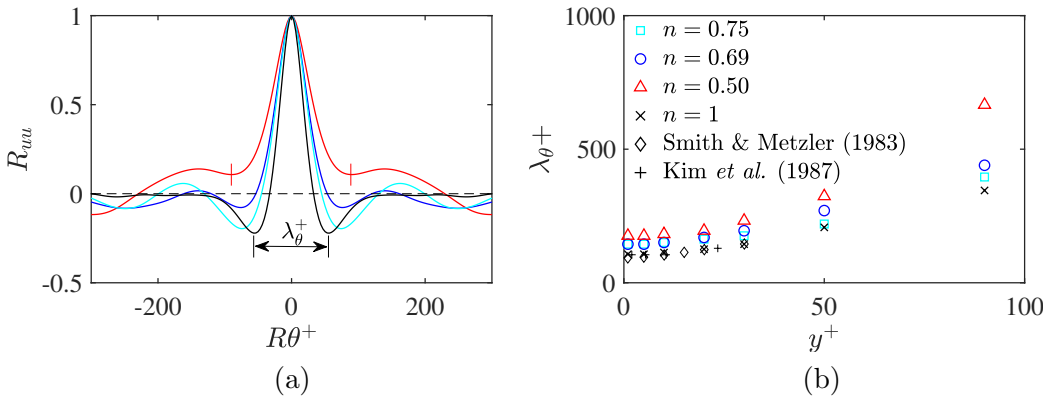

Figure 5.10: (a) Spanwise two-point correlation of the streamwise velocity at $y^+ = 10$. (b) The mean spanwise spacing of the streamwise streaks, estimated from (a). The colours for different case of n follow figure 5.2. The legend follows figure 5.2.

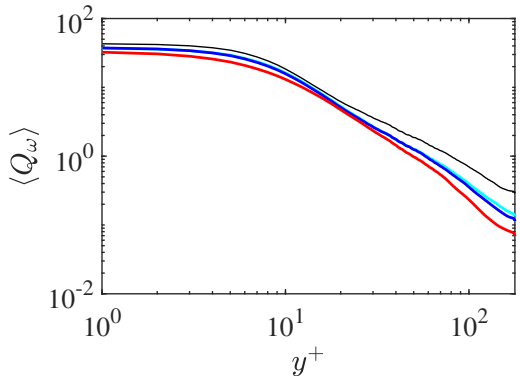

Figure 5.11: Profiles of mean Q_ω at different power-law indices, n. The legend follows figure 5.2.

approximate classification. The mean Q_ω as a function of wall-distance is shown in figure 5.11, and the invariants are normalised by the mean Q_ω in the region where the PDF is computed. The contours range in three decades at 10^{-1}, 10^{-2} and 10^{-3} except in the viscous sublayer where 10^1, 10^0 and 10^{-1} are plotted for smoother contours. The physical meanings of the joint PDF distributions are in figure 2.7.

The $Q - R$ distribution in figure 5.12(a) for the whole pipe domain shows a well-defined 'tear drop' shape, contracted in sector I and enlarged in sector II. Such distribution indicates a preference of vortex stretching over vortex compression (figure 2.7(a)). The 'tear drop' shape with a tail extending along $D = 0$ towards $R >> 0$ indicates an anti-correlation between Q and R so that when $Q > 0$, it is more likely for $R < 0$ and vice versa. That is in regions where enstrophy dominates

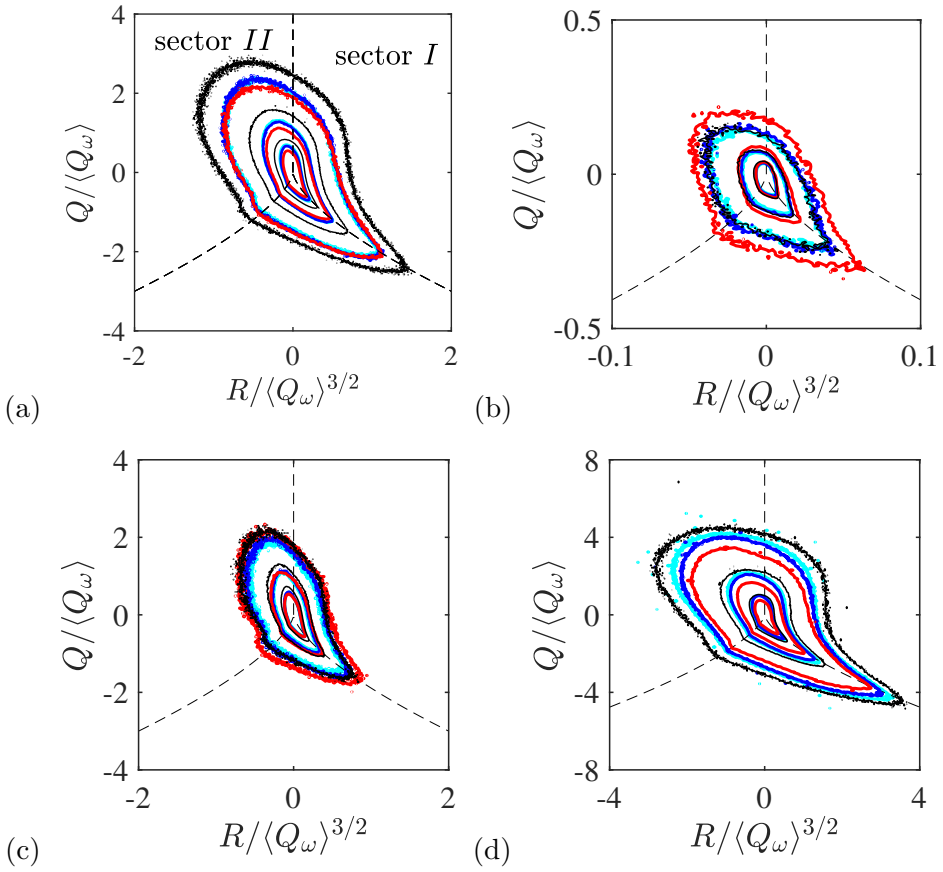

Figure 5.12: Contours of joint PDFs between Q and R in (a) the whole pipe domain, (b) the viscous sublayer, (c) the buffer layer and (d) the outer region. The contours are plotted at 10^{-1}, 10^{-2} and 10^{-3} in (a,c,d) and 10^{1}, 10^{0} and 10^{-1} in (b). The legend for the four different power-law indices follows figure 5.2.

($Q >> 0$), vortex stretching is predominant over vortex compression; in regions dominated by dissipation ($Q << 0$), the flow is predominantly concentrated with sheet-like over tube-like structures (da Silva and Pereira (2008)). By comparing the joint PDF of the whole domain and the separate regions, the 'tear drop' shape of the $Q-R$ joint PDFs for the whole pipe is predominantly due to the outer region turbulence. It should be noted that the joint PDFs are computed from each point of a uniform cylindrical grid which is comparable to the other wall-bounded flows (TBL and channel) once unwrapped, but in physical space, this means that the sampling in the pipe centre is weighted higher. In figures 5.12(b-d), the anti-correlation is gradually developed when moving away from the wall, the tail is more well-defined away from the wall. In the viscous sublayer, the Vieillefosse tail is less apparent and the 'tear drop' shape is in a transitional state (Gomes-Fernandes et al. (2014)), i.e., the anti-correlation of Q and R is less explicit. In the buffer layer, the 'tear drop' shape is clearer in a sense that the preference for vortex stretching (sector II) over vortex compression (sector I) is much more pronounced than in the viscous sublayer. In the outer region, the tail of $Q-R$ anti-correlation becomes more unambiguous for the preference on sheet-like structures. The above observations apply to all four fluids at varying degrees of shear-thinning. The evolution of the $Q-R$ distribution from the wall to the centreline of the pipe is qualitatively similar to the results of channel flows by Blackburn et al. (1996).

Comparing the $Q-R$ distributions for different fluids, in the viscous sublayer, the contours of case $n = 0.75$ and $n = 0.69$ almost coincide with the Newtonian case, despite that the flow already showed noticeably difference in the turbulent structures and regions of significantly weakened off-axis turbulent motions. The sustain of the universality of the 'tear drop'-shaped $Q-R$ distribution in inhomogeneous flows was also reported by Buxton et al. (2017) in the near-field of cylinder wakes. The contours of case $n = 0.5$ show an increase in the normalised magnitude of the invariants while the early form of the 'tear drop' shaped is preserved despite the large absence of turbulent structures.

The effect of the wall is more apparent in the joint PDFs of Q_ω and $-Q_s$. The unique spike along the 45° in wall-bounded flows is entirely due to the presence of the wall. In the extreme vicinity of the wall, $\partial U/\partial y$ and $\partial W/\partial y$ are the only two non-zero terms of the VGT (Blackburn et al. (1996)) so that

$$S_{ij} = \begin{bmatrix} 0 & \frac{\partial U}{\partial y} & 0 \\ \frac{\partial U}{\partial y} & 0 & \frac{\partial W}{\partial y} \\ 0 & \frac{\partial W}{\partial y} & 0 \end{bmatrix}, \Omega_{ij} = \begin{bmatrix} 0 & -\frac{\partial U}{\partial y} & 0 \\ \frac{\partial U}{\partial y} & 0 & \frac{\partial W}{\partial y} \\ 0 & -\frac{\partial W}{\partial y} & 0 \end{bmatrix} \tag{5.7}$$

and hence $Q_\omega = -Q_s = (\partial U^2/\partial^2 y + \partial W^2/\partial^2 y)/4$ and $R_s = R_\omega = 0$. This leads to the results in figure 5.13(b) in which the joint PDF is nearly aligned on the diagonal line of $Q_\omega = -Q_s$ as an indicator for vortex sheet structures (figure 2.7(b)). The influence of the wall decreases towards the outer region yet it can extend well beyond the buffer region; in fact, the clam-shaped distribution observed in free shear flows (Soria et al. (1994); Buxton et al. (2017)) are not obtained, and there is a visible residual of $Q_\omega = -Q_s$ even for the Newtonian case in figure 5.13(d). The $Q_\omega - Q_s$ joint PDFs show a slight preference towards predominant dissipation over enstrophy in the viscous sublayer (clearer in the zoomed view in figure 5.13(b)) whereas in the buffer layer and outer region, the contours extend along the Q_ω axis for locally higher enstrophy. Comparing the contours of different cases, the effect of the wall, i.e., the spike along $Q_\omega = -Q_s$ can survive further away from the wall as the flow becomes more shear-thinning, which is contrary to the initial guess since turbulent energy is toned down near the wall as n decreases. This is perhaps because that turbulent structures originated from the wall can survive in an attached form (Townsend (1976)) and extend higher away from the wall (discussion of figure 5.9).

The influence of the wall is similarly manifested by the joint PDFs of the strain-rate tensor invariants, Q_s and R_s in figure 5.14. The $Q_s - R_s$ distribution was found to be tilted towards $R_s > 0$ in a broom shape in many fully-developed homogeneous turbulence. For the whole pipe domain, the preference for sheet-like structures over tube-like structures (as labelled on the diagram) is only adequate and is a lot less explicit than the strong preference along $R_s = 0$. The extension along $R_s = 0$ is unique for wall-bounded flows (equation (5.7)). In figure 5.14(b), the almost vertical distribution for very high dissipation ($-Q_s >> 0$) along $R_s = 0$ indicates that the local flow is highly $2D$. Similar to the $Q_\omega - Q_s$ maps, the influence of the wall, i.e., the high dissipation and local two-dimensionalisation persist further towards the pipe centre for the non-Newtonian fluids. In the outer region, the contours of case $n = 0.75$ and $n = 0.69$ show no extension along $R_s = 0$ and converge to the Newtonian case whereas case $n = 0.5$ still shows residual of the highly $2D$ near-wall dissipation.

Figure 5.15 shows the joint PDFs of the invariants of the rotation tensor, Q_ω and R_ω. The $-R_\omega < 0$ and the $-R_\omega > 0$ side corresponds to vortex compressing and vortex stretching, respectively (figure 2.7(c)). The $Q_\omega - R_\omega$ distribution appears in a triangular shape, indicating larger range of vortex deformation in regions of lower enstrophy. The spike along $R_\omega = 0$ due to the presence of the wall gradually diminishes when moving away from the wall. Apart from the viscous sublayer,

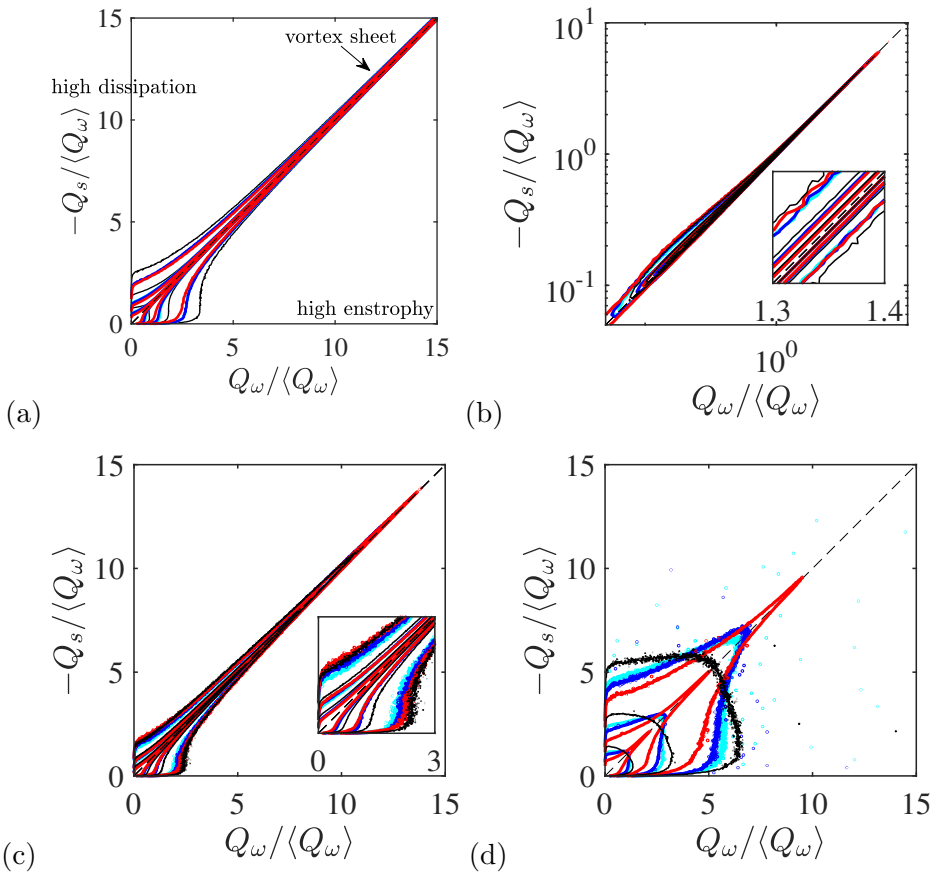

Figure 5.13: Contours of joint PDFs between Q_s and Q_ω, arranged similarly as in figure 5.12.

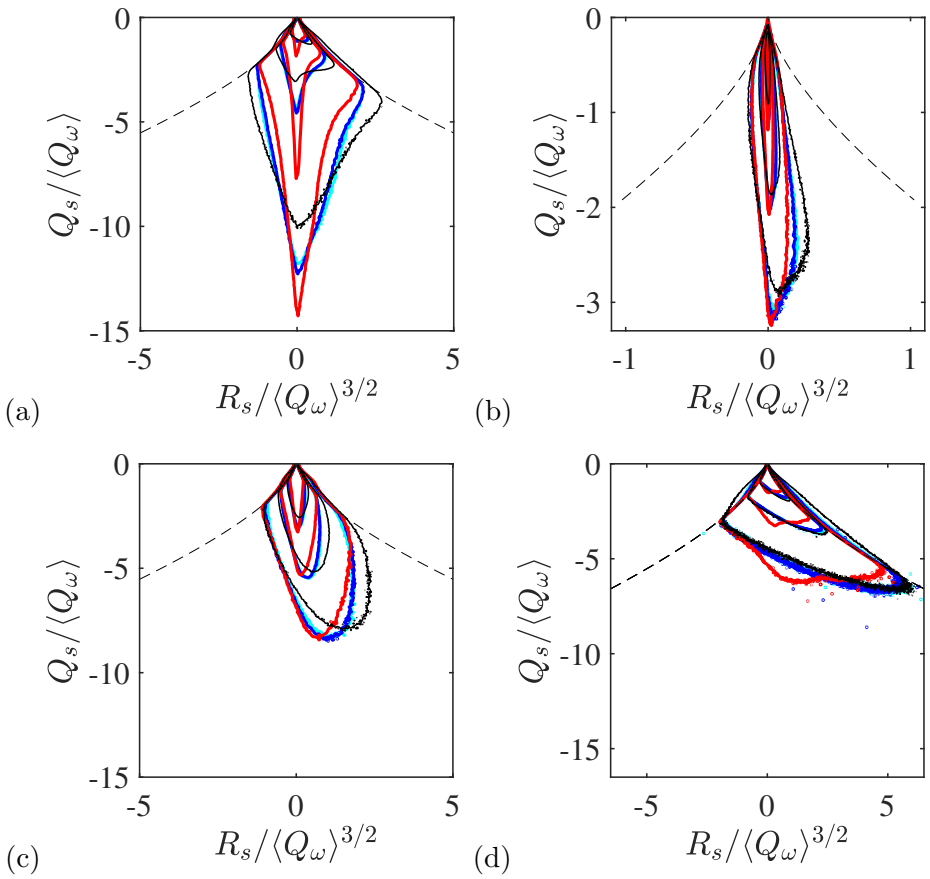

Figure 5.14: Contours of joint PDFs between Q_s and R_s, arranged similarly as in figure 5.12.

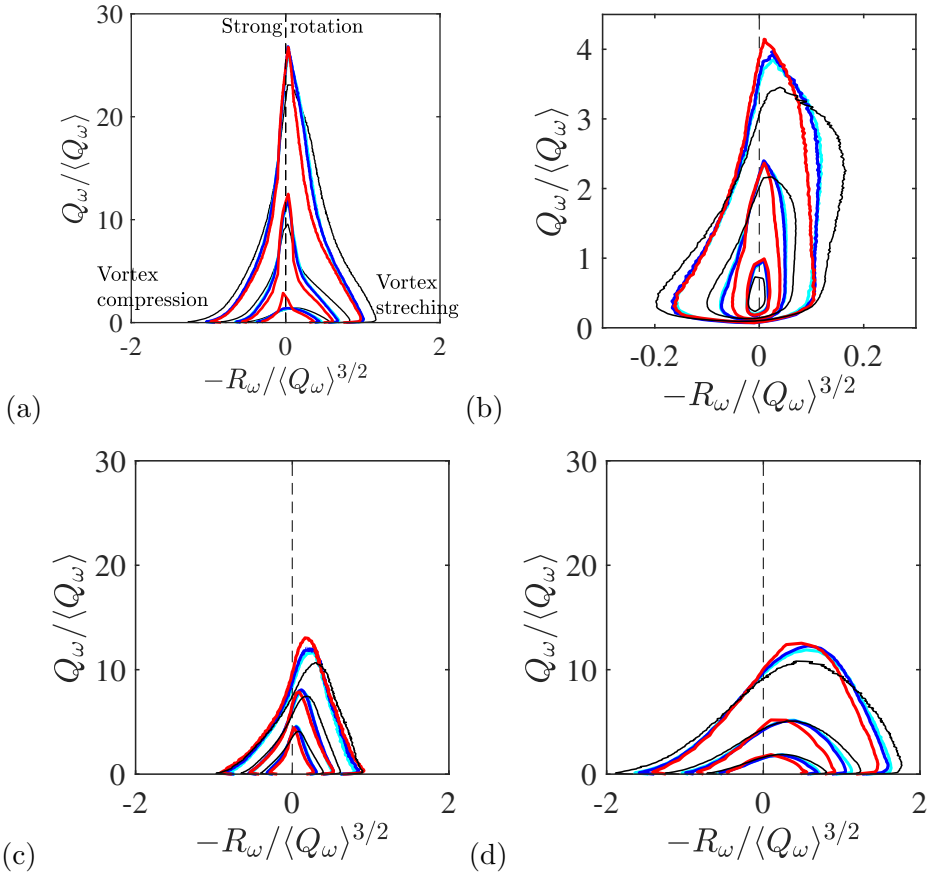

Figure 5.15: Contours of joint PDFs between Q_ω and R_ω, arranged similarly as in figure 5.12.

there is a clear preference of vortex stretching over vortex compression, particularly in the outer region. In the viscous sublayer, for the Newtonian case and all non-Newtonian cases, the joint PDFs show a slight bias towards vortex compression at very low enstrophy while the preference for vortex stretching takes over as Q_ω increases. In addition, the viscous sublayer exhibits the most apparent difference in the contours between the Newtonian and non-Newtonian cases; the preference of vortex compression at low Q_ω and the opposite preference of vortex stretching at high Q_ω is more pronounced in the Newtonian fluid.

5.4 Turbulent spots

While all three non-Newtonian cases are not fully-developed, the $n = 0.5$ case showed the least homogeneity where one may assume that it is already transitional. The results in section 5.2 showed that there is a large portion of the flow with significantly lowered off-axis fluctuations, i.e., the pseudo-laminar regions. The regions remaining highly turbulent ensembles the turbulent slugs in transitional flow. The recent study by Cerbus et al. (2020) confirmed Wygnanski and Champagne (1973) with further evidence that flow in the turbulent slugs surrounded by laminar flow during turbulent transition is statistically identical to fully-developed turbulence.

The turbulent regions and the pseudo-laminar regions are separated by a threshold of the wall-normal fluctuation $\mid v \mid = 0.5 v_{rms}$ which self-adjusts with the wall-distance. The wall-normal component is chosen because it weakened the first when a flow region laminarise, so that putting a threshold on v guarantees that the turbulent regions have sufficiently $3D$ turbulent fluctuations. Figure 5.16 shows the contour of v at three different wall-distance, $y^+ = 5$, $y^+ = 30$ and $y/R = 0.5$. The turbulent regions enclosed by the black solid contour of $\mid v/v_{rms} \mid = 0.5$ are separated from the pseudo-laminar regions. The threshold affects how strictly a turbulent region is defined, yet the threshold has a very low sensitivity on differentiating the pseudo-laminar region and the turbulent region because the difference in the turbulent level between the pseudo-laminar region and the turbulent region is so large. In figure 5.16(a), the contours of $\mid v/v_{rms} \mid = 0.2 \sim 0.8$ can all accurately recognise the turbulent regions. It is also worth mentioning that this method does not suggest 100% of turbulent region for the fully-developed Newtonian flow.

In the following part, the terminology 'pseudo-laminar region' refers to regions with $\mid v/v_{rms} \mid < 0.5$. Figure 5.17(a) shows the average fraction of the turbulent region and the pseudo-laminar region, $\mathcal{V}_T$ and $\mathcal{V}_L$ in the whole pipe volume, $\mathcal{V} = 30\pi R^3$ as functions of wall-distance. As a reference, the Newtonian case ($n = 1$)

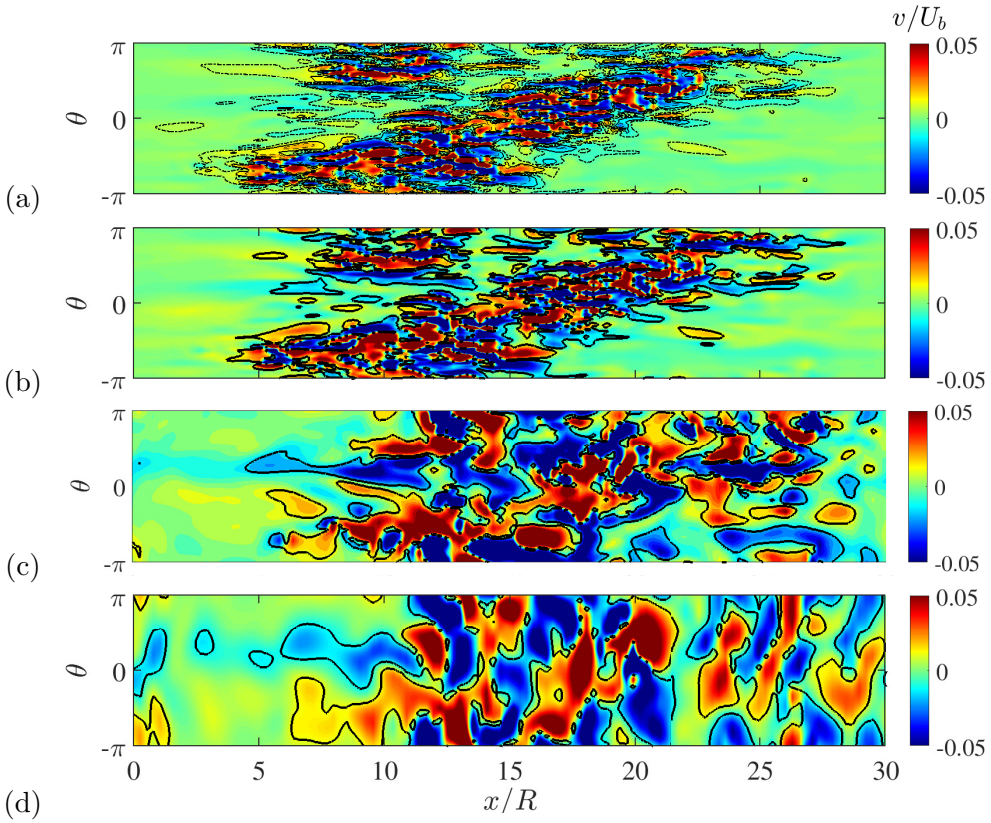

Figure 5.16: Contours of the wall-normal velocity fluctuation v at a fixed wall distance of (a) y^+ = 5, (b) y^+ = 30, (c) y/R = 0.5 and (d) y/R = 0.8 for flows with power-law index n = 0.5. The black lines are the contours of $\mid v/v_{rms} \mid$= 0.2 ($-\cdot-$), 0.5 (——) and 0.8 ($-\,-\,-$).

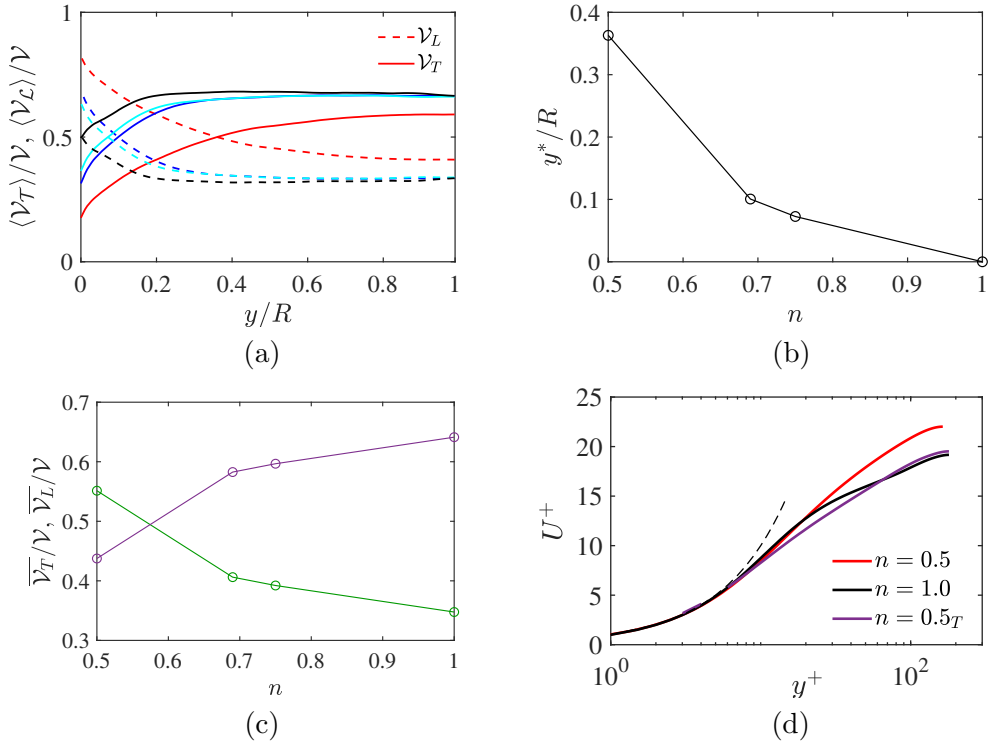

Figure 5.17: (a) Fraction of the turbulent volume and pseudo-laminar volume, $\mathcal{V}_T$ and $\mathcal{V}_L$ to the total pipe domain as functions to the wall-distance. (b) The location of $\langle \mathcal{V}_L \rangle = \langle \mathcal{V}_T \rangle$ in (a). (c) The average turbulent and pseudo-laminar volume in the whole pipe. (d) The mean velocity profile of the turbulent region.

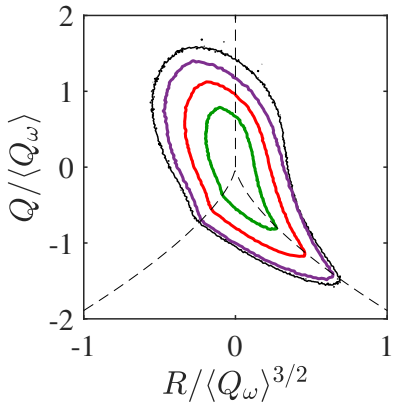

Figure 5.18: Joint PDFs of $Q-R$ for the turbulent region (purple) and the pseudo-laminar region (green) of case $n = 0.5$, overlaid with the PDFs of the whole domain of case $n = 0.5$ (red) and the Newtonian case (black). The contours are at 10^{-2}.

never has $\mathcal{V}_L > \mathcal{V}_T$ and is roughly $1:1$ at the wall for this particular threshold used. For all cases, most of the variations in $\mathcal{V}_T$ and $\mathcal{V}_L$ take place in the near-wall half of the pipe. All three non-Newtonian fluids have $\mathcal{V}_L$ exceeding $\mathcal{V}_T$ at a point when approaching towards the wall. The location of $\langle \mathcal{V}_T \rangle = \langle \mathcal{V}_L \rangle$, y^* is plotted in figure 5.17(b); y^* increases as n decreases, hence the near-wall region where pseudo-laminar flow can balance with the turbulent flow becomes thicker as the flow becomes more shear-thinning, and is much thicker at $n = 0.5$ where y^* increases more rapidly with decreasing n. Figure 5.17(c) shows the global average $\mathcal{V}_T$ and $\mathcal{V}_L$. For the Newtonian case, there is 35% of the pipe counted into the pseudo-laminar region. As n decreases, the turbulent volume decreases and the pseudo-laminar volume increases steadily, matching the visualisations in section 5.2. $\overline{\mathcal{V}_T}$ and $\overline{\mathcal{V}_L}$ exhibit a jump at $n = 0.5$, the fraction of pseudo-laminar flow increases rapidly at $n = 0.5$. The results are consistent with section 5.2 in which the case $n = 0.5$ exhibits a fundamental difference from the other two shear-thinning case. It seems sensible to conclude that the power-law shear-thinning fluid has somehow a yielding behaviour between $n = 0.5$ and $n = 0.69$, the flow experiences intensified non-Newtonian effect for n lower than such a threshold of n.

The mean velocity profile from the turbulent region only is plotted in figure 5.17(d) (purple). Comparing to $\overline{U}$ of $n = 0.5$, the profile of $n = 0.5_T$ is significantly lowered above the viscous sublayer, and the centreline velocity is much closer to the fully-developed Newtonian flow. However, the turbulent profile (buffer layer and log-law behaviour) cannot be obtained and may require a more sophisticated veloc-

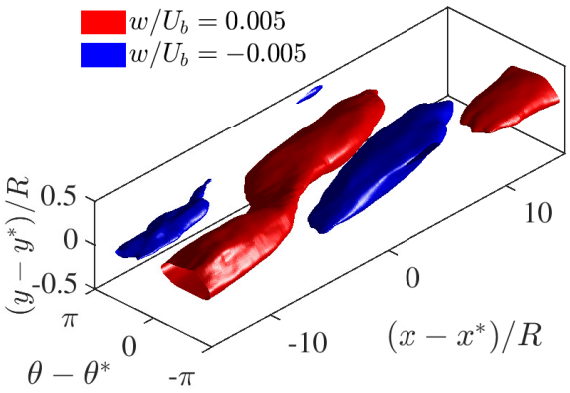

Figure 5.19: Iso-surface of the azimuthal fluctuation, w in the conditional averaged $3D$ fields around the locations with $\mid v/v_{rms} \mid > 0.5$ at $y^+ = 5$. The locations with $\pm v/v_{rms} > 0.5$ in the turbulent region are indicated by (x^*, y^*, θ^*). Negative $x - x^*$ indicates the upstream locations of the turbulent regions.

ity decomposition. The joint PDFs of the VGT invariants are plotted separately for the pseudo-laminar region and the turbulent region in figure 5.18. After the separation, the turbulent region has the $Q - R$ distribution similar to the fully-developed homogeneous Newtonian flow. Although the magnitude of the Q and R decreased significantly in the pseudo-laminar region, the 'tear drop' shape is surprisingly pronounced despite that the flow in the pseudo-laminar region are laminarising.

5.5 Large-scale motions

To investigate the large-scale coherent motions associated with the turbulent spots, conditional averaged streamwise and azimuthal velocity fluctuations, u and w are computed around turbulent regions at different wall-normal locations. The volumetric conditional averaged fields are centred at the points with $\mid v/v_{rms} \mid > 0.5$, denoted as x_i^* so that the location (x^*, y^*, θ^*) represents the turbulent spots, and $x - x^* < 0$ indicates the upstream locations of the turbulent spots.

Figure 5.19 shows the $3D$ iso-surface of w in the conditional averaged field centring turbulent regions near the wall at $y^+ \approx 5$. The $2D$ contours of u and w at $y^* = 0$ in the same conditional average velocity field are shown in figures 5.20(a,c). In figure 5.20(a), the large-scale streamwise acceleration around the turbulent spot is revealed. This supports the findings in section 5.2 where the streamwise acceleration at the leading and trailing edge of the turbulent spot were used to explain the increase of streamwise fluctuation in the non-Newtonian fluids (discussion of figures

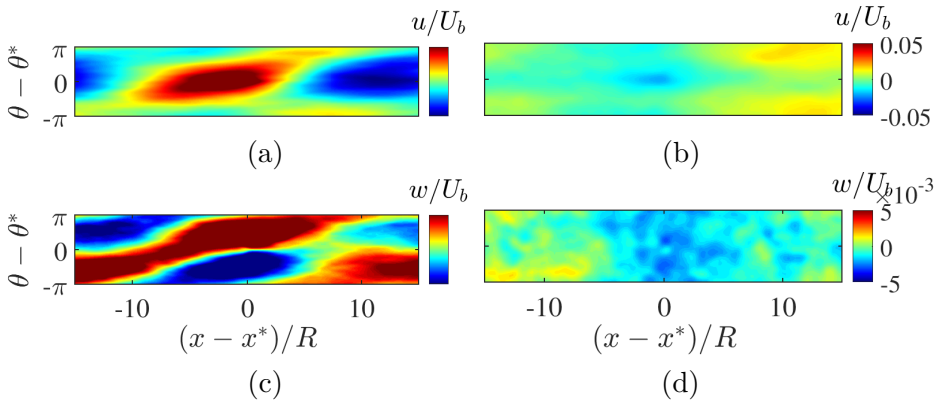

Figure 5.20: (a,b) the streamwise fluctuation, u and (c,d) the azimuthal fluctuation, w in the conditional averaged fields around locations with $\mid v/v_{rms} \mid > 0.5$ at (a,c) $y^+ = 5$ and (b,d) $y/R = 0.5$.

5.3, 5.4 and 5.5). In figure 5.19 and figure 5.20(c), the azimuthal velocity clearly shows a large-scale wavy instability which is typically found in turbulent transition. The coherent motions suggested by these conditional averaged results and the observations in section 5.2 support each other. Figure 5.20(b,d) shows the contours of u and w in the $3D$ conditional average field around turbulent spots away from the wall at $y/R \approx 0.5$. The large-scale streamwise acceleration around the turbulent spot and the wavy instability around the turbulent spots are not observed away from the wall. In fact, the large-scale coherent structures of u and v are found to be only persisting up to $y^+ = 30$, which indicates that the streamwise acceleration and spanwise wavy instability are large-scale phenomenon only existing in the near-wall region of shear-thinning wall-bounded flows.

Proper orthogonal decomposition (POD) in section 3.3 is applied to the azimuthal velocity fluctuation field. Although POD is unsatisfactory in decomposing complex multi-scaled turbulent flows (Baj et al. (2015)), it can be used to extract large energy-containing coherent structures in the flow (Buxton et al. (2017)), for this case, the large-scale instability around the turbulent spots. The POD modes ϕ_i are ranked by their kinetic energy content in a descending order. Figure 5.21 shows the relative kinetic energy content in each of the first 100 modes which contribute approximately 77.5% of the total kinetic energy of all resolved POD modes for case $n = 0.5$. The energy is much more concentrated in the higher ranked modes in a more shear-thinning fluid because of the growing dominance of large-scale coherent motions and reduction of small-scale random turbulent motions. For case $n = 0.5$, the first two modes contain a significant portion ($\approx 9\%$) of the total kinetic energy

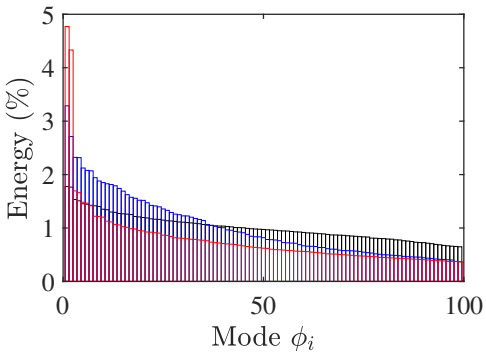

Figure 5.21: Relative kinetic energy content in the POD modes of the azimuthal velocity w for case $n = 0.5$, $n = 0.69$ and $n = 1$ (Newtonian).

which are associated to the large-scale wavy structures in figures 5.20 and 5.19.

Figure 5.22 shows the most energy-containing mode ϕ_1 of the most shear-thinning and the Newtonian cases. Mode ϕ_1 has the largest-scaled structures compared to all other modes which are not shown for brevity. The difference in the scale of structures in ϕ_1 is enormous. The patterns of ϕ_1 in figure 5.22(a) resembles the conditional averaged field of w around the near-wall turbulent spots with large-scale wavy structures. Such organised structures are absence in the fully-developed non-Newtonian flow which is filled by homogeneous small-scale structures. The reconstructed instantaneous field of w using the first m POD modes is denoted as $\mathcal{P}_m[w^\phi]$. Wall-parallel contours at $y/R = 0.1$ of fields $\mathcal{P}_2[w^\phi]$, $\mathcal{P}_{10}[w^\phi]$ and $\mathcal{P}_{50}[w^\phi]$ for case $n = 0.5$ and $n = 1$ are shown in figure 5.23. The contours in the left column for case $n = 0.5$ reconstruct the snapshot shown in figure 5.7(d). $\mathcal{P}_2[w^\phi]$ is mainly constructed with the large-scale wavy structures, where the original field of w is still unclear. The field of w is gradually resembled as more modes are used for reconstruction, $\mathcal{P}_{50}[w^\phi]$ is very similar to the targeting original field in figure 5.23(g). In the right-hand side contours of the fully-developed Newtonian flow case, the original field of w in figure 5.23(h) is also sufficiently resembled by $\mathcal{P}_50[w^\phi]$ using the first 50 modes in figure 5.23(f). These reconstructed fields of the Newtonian fluid are much more homogeneous compared to case $n = 0.5$ and show no such large-scale modes as expected.

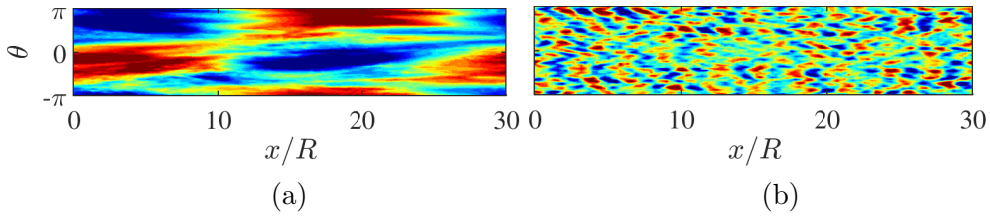

Figure 5.22: The first POD mode, ϕ_1 of the azimuthal velocity w for case (a) $n = 0.5$ and (b) $n = 1$. homogeneous small block-like structure v.s. large-scale wavy structure

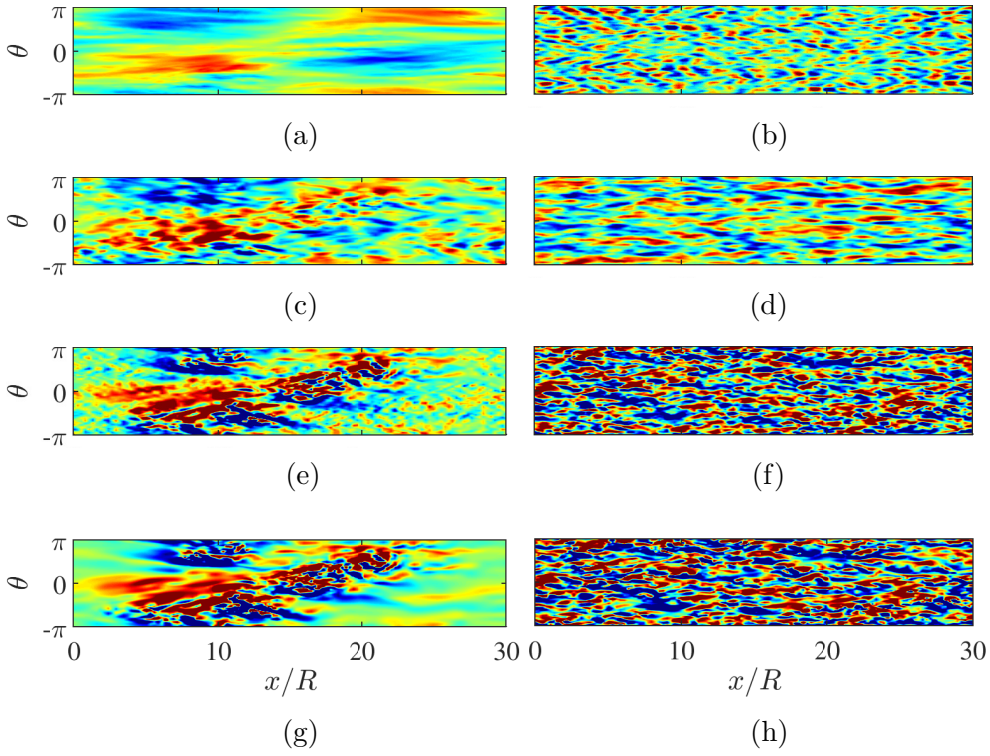

Figure 5.23: Wall-parallel contours at $y/R = 0.1$ in the reconstructed field of the azimuthal velocity w, using POD modes (a,b) $\phi_1 - \phi_2$, (c,d) $\phi_1 - \phi_{10}$, (e,f) $\phi_1 - \phi_{50}$. The original field being reconstructed is in (g) for case $n = 0.5$ (left column) and (h) for case $n = 1$ (right column).

5.6 Summary

In this chapter, an increasingly shear-thinning pipe flow modelled by the power-law rheology at $Re_\tau = 180$ is investigated by means of DNS. Three power-law indices ($n < 1$) were examined. The first part of this chapter focuses on confirming the classical shear-thinning behaviours in turbulent flows reported in the literature. As the flow becomes more shear-thinning, the flow is less homogeneous and shows regions of local laminarisation. In these regions, the off-axis fluctuations are critically lowered, particularly in the wall-normal direction. As n decreases, the turbulent region reduces and the pseudo-laminar region increases. At $n = 0.5$, the flow is already transitional, showing turbulent spots and large regions of pre-transition laminar fluctuations. While the off-axis fluctuations are significantly weakened, the root-mean-square streamwise fluctuation is marginally higher than the Newtonian fluid. By extending the existing analyses on shear-thinning wall turbulence, we found that this is due to the streamwise acceleration in the upstream and downstream of the turbulent spots, which is revealed via conditional averaging around the turbulent spots. Near the wall, the turbulent spots experience strong cross-flow instability. The streaks of streamwise low- and high-momentum pathways are wider in the non-Newtonian fluids, the spanwise streak spacing λ_θ increases with decreasing n. As n decreases, the vortical structures, i.e., hairpin vortex packets become more intact and organised, which is the opposite to Zhen et al. (2013).

The flow topology was interpreted from the joint PDFs of the invariants of the velocity-gradient tensor, the strain-rate tensor and the rotation tensor. These joint PDFs have not been represented before for Newtonian or non-Newtonian pipe flow using DNS data. The PDF distributions of the Newtonian case of the pipe are qualitatively similar to the channel (Blackburn et al. (1996)). The preference of vortex stretching over vortex compression, and predominant sheet-like structures over tube-like structures are more pronounced in the outer region where the flow is closer to free shear flows. The classical 'tear drop'-shaped $Q - R$ joint PDF distribution is obtained in the most inhomogeneous shear-thinning fluid, even in the pseudo-laminar regions. Hence, the universality of the $Q - R$ 'tear drop' shape is not only for fully-developed turbulence.

Chapter 6

Conclusions

The present study investigated turbulent pipe flows of Newtonian and non-Newtonian fluids by means of direct numerical simulations (DNS). The coherent structures, large-scale motions (LSM) and near-wall bursting were investigated regarding to their structural organisation, temporal evolution, topological evolution, and interplay. The DNS was carried out at four Reynolds numbers, Re_τ = 180, 360, 500 and 1000 for the Newtonian fluids. Non-Newtonian fluids at $Re_\tau \approx 180$ with three different levels of shear-thinning were modelled by the power-law rheology.

The first part of this work investigated the uniform-momentum zones (UMZ) and internal shear layers (ISL) in the pipe. Four UMZ and ISL identification methods were used and compared in order to address the sensitivity of UMZ characteristics reported by studies using different methods. Qualitatively consistent results on the UMZ and ISL characteristics were produced by using different identification methods, and similar characteristics reported for the turbulent boundary layers and channel flows were confirmed in the present pipe flow. The flows were demarcated by more UMZs which were thinner at higher Reynolds numbers. The wall-normal distribution of the UMZs showed that the UMZs were more densely populated nearer the wall, which formed a hierarchical distribution of UMZs in wall-bounded flows. The hierarchical scaling of UMZs and UMZ interfaces, being thinner nearer the wall is consistent with the hierarchy of multi-scaled eddies in Townsend's attached eddy hypothesis. Conditional averages as functions of the wall-normal distance from the UMZ interfaces showed that velocity jumps sharply when passing UMZ interfaces and stays relatively uniform inside each zone. This resembles a step-like instantaneous velocity profile in wall-bounded flows. Across the interface, there were also

a rapid decrease of the streamwise turbulent intensity and azimuthal/spanwise vorticity induced by the local high shear.

The UMZ interfaces showed large wall-normal meanderings and are contorted three-dimensionally, manifesting the streaky features of local ejection and sweep events around the interfaces. The level of the UMZ interface contortion, i.e., interface tortuosity was quantified in both $2D$ and $3D$. The interface contortion in both $2D$ and $3D$ is intensified with increasing wall-distance. The interface contortion was found to be more intense in the azimuthal direction than the streamwise direction on average. The interface contortion is a result of the persistent attachment between UMZ interfaces to nearby vortical structures at a desired strength. The UMZ interfaces evolve with the spanwise vortices clustered along the interfaces.

The UMZ interfaces residing away from the wall are representative of the LSMs whereas the UMZ interfaces in the near-wall region can capture the small-scale velocity fluctuation of the near-wall cycle. The third-order skewness between bulges and valleys on the $3D$ UMZ interfaces showed that the large-scale modulation on the near-wall activities is asymmetric to ejections over sweeps. The skewness of the variation of the interface wall-normal location manifests the local imbalance between ejections and sweeps. Near the wall, the velocity fluctuations are biased to significantly stronger ejection events. When departing away from the wall, this asymmetry between ejection and sweep structures gradually restored to a point of locally balanced ejections and sweeps. The location of this change-over from local ejection-dominance to local sweep-dominance showed very weak Reynolds number dependence, roughly $R/2$ away from the wall for all four Reynolds numbers investigated. Further away from the wall, there is a inverse asymmetry of local predominance of stronger sweeps than ejections. The fourth-order kurtosis of the ejections and sweep part of the UMZ interfaces showed an inverse structural organisation in the pipe. Near the wall where the structures are in small scales, the ejections are much spikier than the sweeps; away from the wall where large scales dominate, the ejections become flatter and the large-scale sweeps become very pointy.

The second part of this study investigated the flow statistics and the structure evolution in an increasingly shear-thinning fluids. Three power-law indices were examined. As the flow became shear-thinning, the flow was less homogeneous and started to show regions of local laminarisation. In the pseudo-laminar regions, the off-axis fluctuations were critically lowered, particularly in the wall-normal direction. When the flow became more shear-thinning, the flow was indicatively transitional,

showing turbulent spots surrounded by pre-transition laminar fluctuations. While the off-axis fluctuations were significantly weakened in the non-Newtonian flows, the streamwise fluctuation was found marginally higher than the Newtonian flows due to the streamwise acceleration in the upstream and downstream of the turbulent spots. Near the wall, the turbulent spots experienced strong cross-flow instability. The signature turbulence structure in wall-bounded flows, i.e., the streaks of streamwise low- and high-momentum pathways were wider and flatter as the flow became more shear-thinning, and their spanwise spacing became larger. In the shear-thinning fluids, the quasi-streamwise (hairpin) vortices were remarkably more intact and organised.

The topological flow structures were interpreted from the joint PDF of the velocity-gradient tensor (VGT) invariants. For both the Newtonian and non-Newtonian fluids, the preference of vortex stretching over vortex compression, and predominant sheet-like structures over tube-like structures were more pronounced in the outer region where the flow is closer to free shear flows. The classical $Q-R$ 'tear drop' distribution was obtained in the most inhomogeneous shear-thinning case, and even in the separated pseudo-laminar regions. Therefore, the universality of the $Q-R$ 'tear drop' is evidently not only for fully-developed turbulence. The presence of the wall resulted in a highly $2D$ flow topology in the viscous wall region, shown by the joint PDFs of the invariants of the strain-rate and rotation tensors. The influence of the wall gradually diminished when moving away from the wall, yet it can survive beyond the buffer layer in both Newtonian and non-Newtonian fluids. The wall effects can penetrate further into the outer region in shear-thinning flows, possibly due to that the turbulence structures originated from the wall can and extend well beyond the near-wall region while remaining attached to the wall in non-Newtonian shear-thinning fluids.

Bibliography

H. Abe, H. Kawamura, and Y. Matsuo. Direct numerical simulation of a fully developed turbulent channel flow with respect to the Reynolds number dependence. *ASME: Journal of Fluids Engineering*, 123(2):382–393, 2001.

R. Adrian, C. Meinhart, and C. D. Tompkins. Vortex organisation in the outer region of the turbulent boundary layer. *Journal of Fluid Mechanics*, 422:1–54, 2000.

R. J. Adrian. Hairpin vortex organization in wall turbulence. *Physics of Fluids*, 19 (4):041301, 2007.

L. Agostini and M. A. Leschziner. On the influence of outer large-scale structures on near-wall turbulence in channel flow. *Physics of Fluids*, 26:075107, 2014.

L. Agostini and M. A. Leschziner. Predicting the response of small-scale near-wall turbulence to large-scale outer motions. *Physics of Fluids*, 28:015107, 2016.

J. Ahn, J. H. Lee, S. J. Jang, and H. J. Sung. Direct numerical simulations of fully developed turbulent pipe flows for $Re_\tau = 180$, 544 and 934. *International Journal of Heat and Fluid Flow*, 44:222–228, 2013.

J. Ahn, J. H. Lee, J. Lee, J. Kang, and H. J. Sung. Direct numerical simulations of a $30R$ long turbulent pipe flow at $Re_\tau = 3008$. *Physics of Fluids*, 27(6):065110, 2015.

J. Ahn, J. Lee, and H. J. Sung. Contribution of large-scale motions to the Reynolds shear stress in turbulent pipe flows. *International Journal of Heat and Fluid Flow*, 66(6):209–216, 2017.

K. Akselvoll and P. Moin. An efficient method for temporal integration of the Navier-Stokes equations in confined axisymmetric geometries. *Journal of Computational Physics*, 125(2):454–463, 1996.

R. A. Antonia and J. Kim. Low-Reynolds-number effects on near-wall turbulence. *Journal of Fluid Mechanics*, 276:61–80, 1994.

R. A. Antonia, M. Teitel, J. Kim, and L. W. B. Browne. Low-Reynolds-number effects in a fully developed turbulent channel flow. *Journal of Fluid Mechanics*, 236:579–605, 1992.

W. J. Baars, N. Hutchins, and I. Marusic. Reynolds number trend of hierarchies and scale interactions in turbulent boundary layers. *Philosophical Transactions of the Royal Society A*, 375(20160077), 2017.

P. Baj, P. J. K. Bruce, and O. R. H. Buxton. The triple decomposition of a fluctuating velocity field in a multiscale flow. *Physics of Fluids*, 27(7):074104, 2015.

H. P. Bakewell and J. L. Lumley. Viscous sublayer and adjacent wall region in turbulent pipe flow. *Physics of Fluids*, 10:1880–1889, 1967.

J. R. Baltzer, R. J. Adrian, and X. Wu. Structure organization of large and very large scales in turbulent pipe flow simulation. *Journal of Fluid Mechanics*, 720: 236–279, 2013.

J. C. C. Bautista, A. Ebadi, C. M. White, G. P. Chini, and J. C. Klewicki. A uniform momentum zone-vortical fissure model of the turbulent boundary layer. *Journal of Fluid Mechanics*, 858:609–633, 2019.

A. Benslimane, K. Bekkour, P. Francǫis, and H. Bechir. Laminar and turbulent pipe flow of bentonite suspensions. *Journal of Petroleum Science and Engineering*, 139: 85–93, 2016.

G. Berkooz, P. Holmes, and J. L. Lumley. The proper orthogonal decomposition in the analysis of turbulent flows. *Annual Review of Fluid Mechanics*, 25(1):539–575, 1993.

M. Bernardini, S. Pirozzoli, and P. Orlandi. Velocity statistics in turbulent channel flow up to $Re_\tau = 4000$. *Journal of Fluid Mechanics*, 742:171–191, 2014.

D. Biswas, D. M. Casey, D. C. Crowder, D. A. Steinman, Y. H. Yun, and F. Loth. Characterization of transition to turbulence for blood in a straight pipe under steady flow conditions. *Journal of Biomechanical Engineering*, 138:071001–1, 2016.

H. M. Blackburn, N. N. Mansour, and B. J. Cantwell. Topology of fine-scale motions in turbulent channel flow. *Journal of Fluid Mechanics*, 310:269–292, 1996.

R. F. Blackwelder and H. Eckelmann. Streamwise vortices associated with the bursting phenomenon. *Journal of Fluid Mechanics*, 94(part 3):577–594, 1979.

D. C. Bogue and A. B. Metzner. Velocity profiles in turbulent pipe flow - Newtonian and non-Newtonian fluids. *Industrial and Engineering Chemistry Fundamentals*, 2:143, 1963.

A-J. Buchner, A. Lozano-Durán, V. Kitsios, C. Atkinson, and J. Soria. Local topology via the invariants of the velocity gradient tensor within vortex clusters and intense Reynolds stress structures in turbulent channel flow. *J. Phys.: Conf. Ser.*, 708:012005, 2016.

M. H. Buschmann, T. Indinger, and M. Gad-el-Hak. Near-wall behavior of turbulent wall-bounded flows. *International Journal of Heat and Fluid Flow*, 30:993–1006, 2009.

O. R. H. Buxton, M. Breda, and X. Chen. Invariants of the velocity-gradient tensor in a spatially developing inhomogeneous turbulent flow. *Journal of Fluid Mechanics*, 817:1–20, 2017.

B. J. Cantwell. Organized motion in turbulent flow. *Annual Review of Fluid Mechanics*, 13:457–515, 1981.

B. J. Cantwell. On the behavior of velocity gradient tensor invariants in direct numerical simulations of turbulence. *Physics of Fluids A*, 5(8):2008–2013, 1993.

R. T. Cerbus, J. Skakibara, G. Gioia, and P. Chakraborty. The turbulent flow in a slug: a re-examination. *Journal of Fluid Mechanics*, 883:A13, 2020.

X. Chen, Y. M. Chung, and M. Wan. The quiescent core of turbulent pipe flow. In *UK Turbulence Consortium*, 2018.

X. Chen, Y. M. Chung, and M. Wan. Uniform momentum zones in a turbulent pipe flow. In *UK Turbulence Consortium*, 2019a.

X. Chen, Y. M. Chung, and M. Wan. The quiescent core of turbulent pipe flow. In *Proceedings of the Eleventh International Symposium on Turbulent and Shear Flow Phenomena*, 2019b. URL "http://www.tsfp-conference.org/proceedings/2019/127.pdf".

X. Chen, Y. M. Chung, and M. Wan. Uniform-momentum zones in a turbulent pipe flow. *Journal of Fluid Mechanics*, 884:A25, 2020.

X. Chen, Y. M. Chung, and M. Wan. The uniform-momentum zones and internal shear layers in turbulent pipe flows at Reynolds numbers up to Re_τ = 1000. *International Journal of Heat and Fluid Flow*, 90:108817, 2021.

C. Chin, A. S. H. Ooi, I. Marusic, and H. M. Blackburn. The influence of pipe length on turbulence statistics computed from direct numerical simulation data. *Physics of Fluids*, 22(11):115107, 2010.

C. Chin, J. P. Monty, and A. Ooi. Reynolds number effects in DNS of pipe flow and comparison with channels and boundary layers. *International Journal of Heat and Fluid Flow*, 45:33–40, 2014.

M. S. Chong, A. E. Perry, and B. J. Cantwell. A general classification of three-dimensional flow fields. *Physics of Fluids A*, 2(5):765–777, 1990.

D. Chung and B. J. McKeon. Large-eddy simulation of large-scale structures in long channel flow. *Journal of Fluid Mechanics*, 661:341–364, 2010.

C. B. da Silva and C. F. Pereira. Invariants of the velocity-gradient, rate-of-strain, and rate-of-rotation tensors across the turbulent/nonturbulent interface in jets. *Physics of Fluids*, 20:055101, 2008.

C. M. de Silva, N. Hutchins, and I. Marusic. Uniform momentum zones in turbulent boundary layers. *Journal of Fluid Mechanics*, 786:309–331, 2016.

C. M. de Silva, J. Philip, N. Hutchins, and I. Marusic. Interfaces of uniform momentum zones in turbulent boundary layers. *Journal of Fluid Mechanics*, 820: 451–478, 2017.

J. C. del Álamo and J. Jiménez. Spectra of the very large anisotropic scales in turbulent channels. *Physics of Fluids*, 15(6):L41–L44, 2003.

J. C. del Álamo, J. Jiménez, P. Zandonade, and R. D. Moser. Scaling of the energy spectra of turbulent channels. *Journal of Fluid Mechanics*, 500:135–144, 2004.

A. A. Draad, G. D. C. Kuiken, and F. T. M. Nieuwstadt. Laminar-turbulent transition in pipe flow for Newtonian and non-Newtonian fluids. *Journal of Fluid Mechanics*, 377:267–312, 1998.

S. Dunstan. *DNS of convective rotational turbulence in the pipe, concentric pipe and jet.* PhD thesis, School of Engineering, University of Warwick, UK, May 2020.

J. G. M. Eggels, F. Unger, M. H. Weiss, J. Westerweel, R. J. Adrian, R. Friedrich, and F. T. M. Nieuwstadt. Fully-developed turbulent pipe-flow: A comparison between direct numerical simulation and experiment. *Journal of Fluid Mechanics*, 268:175–209, 1994.

J. Eisma, J. Westerweel, G. Ooms, and G. E. Elsinga. Interfaces and internal layers in a turbulent boundary layer. *Physics of Fluids*, 27:055103, 2015.

G. K. El Khoury, P. Schlatter, A. Noorani, P. F. Fischer, G. Brethouwer, and A. V. Johansson. Direct numerical simulation of turbulent pipe flow at moderately high Reynolds numbers. *Flow, Turbulence and Combustion*, 91(3):475–495, 2013.

M. P. Escudier and F. Presti. Pipe flow of a thixotropic liquid. *Journal of Non-Newtonian Fluid Mechanics*, 62:291–306, 1996.

M. P. Escudier, F. Presti, and S. Smith. Drag reduction in the turbulent pipe flow of polymers. *Journal of Non-Newtonian Fluid Mechanics*, 81:197–213, 1999.

M. P. Escudier, R. J. Poole, F. Presti, C. Dales, C. Nouar, C. Desaubry, L. Graham, and L. Pullum. Observations of asymmetrical flow behaviour in transitional pipe flow of yield-stress and other shear-thinning liquids. *Journal of Non-Newtonian Fluid Mechanics*, 127:143–155, 2005.

M. P. Escudier, S. Rosa, and R. J. Poole. Asymmetry in transitional pipe flow of drag-reducing polymer solutions. *Journal of Non-Newtonian Fluid Mechanics*, 161:19–29, 2009.

A. Esmael and C. Nouar. Transitional flow of a yield-stress fluid in a pipe: Evidence of a robust coherent structure. *Physical Review E*, 77:057302, 2008.

A. Esmael, C. Nouar, A. Lefèvre, and N. Nabouya. Transitional flow of a non-Newtonian fluid in a pipe: Experimental evidence of weak turbulence induced by shear-thinning behavior. *Physics of Fluids*, 22:101701, 2010.

R. E. Falco. Coherent motions in the outer region of turbulent boundary layers. *Physics of Fluids*, 20:124132, 1977.

D. Fan, J. Xu, M. X. Yao, and J.-P. Hickey. On the detection of internal interfacial layers in turbulent flows. *Journal of Fluid Mechanics*, 872:198–217, 2019.

P. F. Fischer, J. W. Lottes, and S. G. Kerkemeier. nek5000 Web page, 2008. http://nek5000.mcs.anl.gov.

J. M. Fitz-Gerald. Non-Newtonian secretion flow in tubes. *Journal of Fluid Mechanics*, 66:529–539, 1974.

B. Ganapathisubramani, E. K. Longmire, and I. Marusic. Characteristics of vortex packets in turbulent boundary layers. *Journal of Fluid Mechanics*, 478:35–46, 2003.

A. A. Gavrilov and V. Ya. Rudyak. Direct numerical simulation of the turbulent flows of power-law fluids in a circular pipe. *Thermophysics and Aeromechanics*, 23(4):473–486, 2016.

A. A. Gavrilov and V. Ya. Rudyak. Direct numerical simulation of the turbulent energy balance and the shear stresses in power-law fluid flows in pipes. *Fluid Dynamics*, 52(3):363–374, 2017.

B. Gomes-Fernandes, B. Ganapathisubramani, and J. C. Vassilicos. Evolution of the velocity-gradient tensor in a spatially developing turbulent flow. *Journal of Fluid Mechanics*, 756:252–292, 2014.

M. Guala, S. E. Hommema, and R. J. Adrian. Large-scale and very-large-scale motions in turbulent pipe flow. *Journal of Fluid Mechanics*, 554:521–542, 2006.

M. Gul, G. E. Elsinga, and J. Westerweel. Internal shear layers and edges of uniform momentum zones in a turbulent pipe flow. *Journal of Fluid Mechanics*, 901:A10–1, 2020.

M. R. Head and P. Bandyopadhyay. New aspects of turbulent boundary-layer structure. *Journal of Fluid Mechanics*, 107:297–337, 1981.

M. Heisel, de Silva C. M., N. Hutchins, Marusic I., and M. Guala. On the mixing length eddies and logarithmic mean velocity profile in wall turbulence. *Journal of Fluid Mechanics*, 887:R1, 2020.

L. H. O. Hellström and A. J. Smits. The energetic motions in turbulent pipe flow. *Physics of Fluids*, 26(12):125102, 2014.

J. O. Hinze. *Turbulence*. McGraw-Hill Series in Mechanical Engineering, 1975.

B. Hof, C. W. H. van Doorne, J. Westerweel, and F. T. M. Nieuwstadt. Turbulence regeneration in pipe flow at moderate Reynolds numbers. *Physical Review Letters*, 95:214502, 2005.

S. Hoyas and J. Jiménez. Scaling of the velocity fluctuations in turbulent channels up to $Re_\tau = 2003$. *Physics of Fluids*, 18(1):011702, 2006.

J. C. R. Hunt and J. F. Morrison. Eddy structure in turbulent boundary layers. *European Journal of Mechanics B/Fluids*, 19:673–694, 2000.

N. Hutchins and I. Marusic. Large-scale influences in near-wall turbulence. *Philosophical Transactions of the Royal Society A*, 365:647–664, 2007a.

N. Hutchins and I. Marusic. Evidence of very long meandering features in the logarithmic region of turbulent boundary layers. *Journal of Fluid Mechanics*, 579:1–28, 2007b.

N. Hutchins, T. B. Nickels, I. Marusic, and M. S. Chong. Hot-wire spatial resolution issues in wall-bounded turbulence. *Journal of Fluid Mechanics*, 635:103–136, 2009.

Y. Hwang. Statistical structure of self-sustaining attached eddies in turbulent channel flow. *Journal of Fluid Mechanics*, 767:254–289, 2015.

S. J. Illingworth, J. P. Monty, and I. Marusic. Estimating large-scale structures in wall turbulence using linear models. *Journal of Fluid Mechanics*, 842:146–162, 2018.

K. Iwamoto, Y. Suzuki, and N. Kasagi. Reynolds number effect on wall turbulence: Toward effective feedback control. *International Journal of Heat and Fluid Flow*, 23(5):678–689, 2002.

J. Jiménez. The largest scales of turbulent flows. Annual research briefs, CTR, Stanford University, 1998.

J. Jiménez. Cascades in wall-bounded turbulence. *Annual Review of Fluid Mechanics*, 44:27–45, 2012.

J. Jiménez and A. Pinelli. The autonomous cycle of near-wall turbulence. *Journal of Fluid Mechanics*, 389:335–359, 1999.

J. Jiménez, J. C. del Álamo, and O. Flores. The large-scale dynamics of near-wall turbulence. *Journal of Fluid Mechanics*, 505:179–199, 2004.

J. Jiménez, S. Hoyas, M. P. Simens, and Y. Mizuno. Turbulent boundary layers and channels at moderate Reynolds number. *Journal of Fluid Mechanics*, 657: 335–360, 2010.

S. Y. Jung and Y. M. Chung. Large-eddy simulations of accelerated turbulent flow in a circular pipe. *International Journal of Heat and Fluid Flow*, 33(1):1–8, 2012.

K. S. Kankanwadi and O. R. H. Buxton. Turbulent entrainment into a cylinder wake from a turbulent background. *Journal of Fluid Mechanics*, 905:A35, 2020.

Kevin, J. Monty, and N. Hutchins. The meandering behaviour of large-scale structures in turbulent boundary layers. *Journal of Fluid Mechanics*, 865:R1, 2019.

J. Kim, P. Moin, and R. Moser. Turbulence statistics in fully developed channel flow at low Reynolds number. *Journal of Fluid Mechanics*, 177:133–166, 1987.

K. C. Kim and R. J. Adrian. Very large-scale motion in the outer layer. *Physics of Fluids*, 11(2):417422, 1999.

J. Klewicki, C. Chin, H. M. Blackburn, A. Ooi, and I. Marusic. Reynolds number dependence, scaling and dynamics of turbulent boundary layers. *ASME: Journal of Fluids Engineering*, 24:045107, 2010.

S. J. Kline, W. C. Reynolds, F. A. Schraub, and P. W. Runstadler. The structure of turbulent boundary layers. *Journal of Fluid Mechanics*, 30(4):741–773, 1967.

Y. Kwon. *The quiescent core of turbulent channel and pipe flows*. PhD thesis, University of Melbourne, 2016.

Y. S. Kwon, J. Philip, C. M. de Silva, N. Hutchins, and J. P. Monty. The quiescent core of turbulent channel flow. *Journal of Fluid Mechanics*, 751:228–254, 2014.

A. Laskari, R. de Kat, R. J. Hearst, and B. Ganapathisubramani. Time evolution of uniform momentum zones in a turbulent boundary layer. *Journal of Fluid Mechanics*, 842:554–590, 2018.

J. H. Lee and H. J. Sung. Very-large-scale motions in a turbulent boundary layer. *Journal of Fluid Mechanics*, 673:80–120, 2011.

M. Lee and R. D. Moser. Direct numerical simulation of turbulent channel flow up to $Re_\tau \approx 5200$. *Journal of Fluid Mechanics*, 774:395–415, 2015.

M. Lee and R. D. Moser. Extreme-scale motions in turbulent plane Couette flows. *Journal of Fluid Mechanics*, 842:128–145, 2018.

Z. Liu, R. J. Adrian, and T. J. Hanratty. Large-scale modes of turbulent channel flow: transport and structure. *Journal of Fluid Mechanics*, 448:53–80, 2001.

P. Loulou, R. D. Moser, N. N. Mansour, and B. J. Cantwell. Direct numerical simulation of incompressible pipe flow using a b-spline spectral method. *NASA Technical Memorandum*, page 110436, 1997.

A. Lozano-Durán and J. Jiménez. Effect of the computational domain on direct simulations of turbulent channels up to Re_τ = 4200. *Physics of Fluids*, 26(1): 011702, 2014.

A. Lozano-Durán, O. Flores, and J. Jiménez. The three-dimensional structure of momentum transfer in turbulent channels. *Journal of Fluid Mechanics*, 694:100–130, 2012.

S. S. Lu and W. W. Willmarth. Measurements of the structure of the Reynolds stress in a turbulent boundary layer. *Journal of Fluid Mechanics*, 60:481–511, 1973.

Y. Maday and A. T. Patera. Spectral element methods for the Navier-Stokes equations. *State of the Art Surveys in Computational Mechanics ASME*, pages 71–143, 1989.

I. Marusic. On the role of large-scale structures in wall turbulence. *Physics of Fluids*, 13(3):735–743, 2001.

I. Marusic and N. Hutchins. Study of the log-layer structure in wall turbulence over a very large range of Reynolds number. *Flow, Turbulence and Combustion*, 81: 115–130, 2008.

I. Marusic and J. P. Monty. Attached eddy model of wall turbulence. *Annual Review of Fluid Mechanics*, 51:49–74, 2019.

I. Marusic, R. Mathis, and N. Hutchins. High Reynolds number effects in wall turbulence. *International Journal of Heat and Fluid Flow*, 31(3):418–428, 2010.

R. Mathis, N. Hutchins, and I. Marusic. Large-scale amplitude modulation of the small-scale structures in turbulent boundary layer. *Journal of Fluid Mechanics*, 628:311–337, 2009a.

R. Mathis, J. P. Monty, N. Hutchins, and I. Marusic. Comparison of large-scale amplitude modulation in turbulent boundary layers, pipes, and channel flows. *Physics of Fluids*, 21(11):111703, 2009b.

R Mayle and A. Schulz. The path to predicting bypass transition. *ASME: Journal of Turbomachinery*, 119:405–411, 1997.

B. J. McKeon and A. S. Sharma. A critical-layer framework for turbulent pipe flow. *Journal of Fluid Mechanics*, 658:336–382, 2010.

C. D. Meinhart and R. J. Adrian. On the existence of uniform momentum zones in a turbulent boundary layer. *Physics of Fluids*, 694(7):694–696, 1995.

M. M. Metzger and J. C. Klewicki. A comparative study of near-wall turbulence in high and low Reynolds number boundary layers. *Physics of Fluids*, 13(3):692701, 2001.

S. L. Mitchell and T. G. Myers. The laminar-turbulent transition of yield stress fluids in large pipes. In *Mathematics in Industry Study Group*, January, University of Witwatersrand, 2007.

P. Moin and K. Mahesh. Direct numerical simulation: A tool in turbulence research. *Annual Review of Fluid Mechanics*, 30:539–578, 1998.

J. P. Monty, J.A. Stewart, R. C. Williams, and M. S. Chong. Large-scale features in turbulent pipe and channel flows. *Journal of Fluid Mechanics*, 589:147–156, 2007.

J. P. Monty, N. Hutchins, H. C. H. Ng, I. Marusic, and M. S. Chong. A comparison of turbulent pipe, channel and boundary layer flows. *Journal of Fluid Mechanics*, 632:431–442, 2009.

J. F. Morrison, B. J. McKeon, W. Jiang, and A. J. Smits. Scaling of the streamwise velocity component in turbulent pipe flow. *Journal of Fluid Mechanics*, 508:99–131, 2004.

R. Moser, J. Kim, and N. Mansour. Direct numerical simulation of turbulent channel flow up to $Re_\tau = 590$. *Physics of Fluids*, 11(4):943–945, 1999.

H. Nakagawa and I. Nezu. Structure of space-time correlations of bursting phenomena in an open-channel flow. *Journal of Fluid Mechanics*, 104:1–43, 1981.

J. M. Nouri, H. Umur, and J. H. Whitelaw. Flow of Newtonian and non-Newtonian fluids in concentric and eccentric annuli. *Journal of Fluid Mechanics*, 253:617–641, 1993.

R. L. Panton. Overview of the self-sustaining mechanisms of wall turbulence. *Progress in Aerospace Science*, 37:341–383, 2001.

J. Peixinho, C. Nouar, C. Desaubry, and Théron B. Laminar transitional and turbulent flow of yield stress fluid in a pipe. *Journal of Non-Newtonian Fluid Mechanics*, 128:172–184, 2005.

A. E. Perry and M. S. Chong. On the mechanism of wall turbulence. *Journal of Fluid Mechanics*, 119:173–217, 1982.

F. T. Pinho and J. H. Whitelaw. Flow of non-Newtonian fluids in a pipe. *Journal of Non-Newtonian Fluid Mechanics*, 34:129–144, 1990.

P. J. A. Priyadarshana, J. C. Klewicki, S. Treat, and J. F. Foss. Statistical structure of turbulent-boundary-layer velocity vorticity products at high and low Reynolds numbers. *Journal of Fluid Mechanics*, 570:136–139, 2007.

K. N. Rao, R. Narasimha, and M. A. B Narayanan. The bursting phenomenon in a turbulent boundary layer. *Journal of Fluid Mechanics*, 48(part 2):339–352, 1971.

S. K. Robinson. Coherent motions in the turbulent boundary layer. *Annual Review of Fluid Mechanics*, 23:601–639, 1991.

M. Rudman, H. M. Blackburn, L. J. Graham, and L. Pullum. Weakly turbulent pipe flow of a power law fluid. In *14th Australasian Fluid Mechanics Conference*, Adelaide, Australia, 2001.

M. Rudman, H. M. Blackburn, L. J. W. Graham, and L. Pullum. Turbulent pipe flow of shear-thinning fluids. *Journal of Non-Newtonian Fluid Mechanics*, 118: 33–48, 2004.

T. Saxton-Fox and B. J. McKeon. Coherent structures, uniform momentum zones and the streamwise energy spectrum in wall-bounded turbulent flows. *Journal of Fluid Mechanics*, 826:R6. doi:10.1017/jfm.2017.493, 2017.

P. Schlatter, R. Örlü, Q. Li, G. Brethouwer, J. H. M. Fransson, A. V. Johansson, P. H. Alfredsson, and D. S. Henningson. Turbulent boundary layers up to Re_θ = 2500 studied through simulation and experiment. *Physics of Fluids*, 21:051702, 2009.

P. Schlatter, Q. Li, G. Brethouwer, A. V. Johansson, and D. S. Henningson. Simulations of spatially evolving turbulent boundary layers up to re_θ = 4300. *International Journal of Heat and Fluid Flow*, 31:251–261, 2010.

J. Sillero, J. Jiménez, and R. D. Moser. One-point statistics for turbulent wall-bounded flows at Reynolds numbers up to $\delta^+ \approx 2000$. *Physics of Fluids*, 25: 105102, 2013.

J. Singh, M. Rudman, and H. M. Blackburn. The influence of shear-dependent rheology on turbulent pipe flow. *Journal of Fluid Mechanics*, 822:848–879, 2017.

C. R. Smith and S. P. Metzler. The characteristics of low-speed streaks in the near-wall region of a turbulent boundary layer. *Journal of Fluid Mechanics*, 129:27–54, 1983.

A. J. Smits, B. J. McKeon, and I. Marusic. High-Reynolds number wall turbulence. *Annual Review of Fluid Mechanics*, 43:353–375, 2011.

J. Soria, R. Sondergaard, B. J. Cantwell, M. S. Chong, and A. E. Perry. A study of the fine-scale motions of incompressible time-developing mixing layers. *Physics of Fluids*, 6(2):871–884, 1994.

P. R. Spalart. Direct simulation of a turbulent boundary layer up to $Re_\theta = 1410$. *Journal of Fluid Mechanics*, 187:61–98, 1988.

T. Theodorsen. Mechanism of turbulence. In *Proc. Second Midwestern Conference on Fluid Mechanics, Mar. 17-19*, pages Ohio state University, Columbus, Ohio., 1952.

C. D. Tomkins and R. J. Adrian. Spanwise structure and scale growth in turbulent boundary layer. *Journal of Fluid Mechanics*, 490:37–74, 2003.

A. A. Townsend. The structure of the turbulent boundary layer. *Math. Proc. Camb. Philos. Soc.*, 47:375–395, 1951.

A. A. Townsend. *The Structure of Turbulent Shear Flow*. Cambridge University Press, 2nd edition, 1976.

A. Tsinober. *An Informal Conceptual Introduction to Turbulence*. Springer, 2nd edition, 2009.

L. S. Tuckerman, M. Chantry, and D. Barkley. Patterns in wall-bounded shear flows. *Annual Review of Fluid Mechanics*, 52:343–67, 2020.

P. Vieillefosse. Local interaction between vorticity and shear in a perfect incompressible fluid. *J. Phys. (Paris)*, 43(6):837–842, 1982.

C. Wagner, T. J. Huttl, and R. Friedrich. Low-Reynolds-number effects derived from direct numerical simulations of turbulent pipe flow. *Computers and Fluids*, 30(5):581–590, 2001.

J. M. Wallace, H. Eckelman, and R. S. Brodkey. The wall region in turbulent shear flow. *Journal of Fluid Mechanics*, 54:39–48, 1972.

G. Wang, X. Zheng, and J. Tao. Very large scale motions and $pm10$ concentration in a high-Re boundary layer. *Physics of Fluids*, 29:061701, 2017.

Z. Wang. *A numerical investigation of unsteady turbulence in straight and curved pipes*. PhD thesis, School of Engineering, University of Warwick, UK, September 2017.

Z. Wang, R. Orlu, P. Schlatter, and Y. M. Chung. Direct numerical simulation of a turbulent 90 degrees bend pipe flow. *International Journal of Heat and Fluid Flow*, 73:199–208, 2018.

C. E. Wark and H. M. Nagib. Experimental investigation of coherent structures in turbulent boundary layers. *Journal of Fluid Mechanics*, 230:183–208, 1991.

C. Wen. *The transition to asymmetry in pipe flow of shear-thinning fluids*. PhD thesis, University of Liverpool, September 2016.

X. Wu and P. Moin. A direct numerical simulation study on the mean velocity characteristics in turbulent pipe flow. *Journal of Fluid Mechanics*, 608:81–112, 2008.

X. Wu, J. R. Baltzer, and R. J. Adrian. Direct numerical simulation of a $30R$ long turbulent pipe flow at $R^+ = 685$: large- and very-large-scale motions. *Journal of Fluid Mechanics*, 698:235–281, 2012.

Z. Wu, C. Atkinson, and J. Soria. The three-dimensional structures in turbulent Couette-Poiseuille flows on the verge of separation. In *Turbulence and Shear Flow Phenomena -11*, Southampton, UK, 2019.

I. J. Wygnanski and F. H. Champagne. On transition in a pipe. part 1. the origin of puffs and slugs and the flow in a turbulent slug. *Journal of Fluid Mechanics*, 59(part 2):281–335, 1973.

Y. Yamamoto and Y. Tsuji. Numerical evidence of logarithmic regions in channel flow at $Re_\tau = 8000$. *Physical Review Fluids*, 3:012602, 2018.

J. Yang, J. Hwang, and H. J. Sung. Structural organization of the quiescent core region in a turbulent channel flow. *International Journal of Heat and Fluid Flow*, 27:055103, 2016.

J. Yang, J. Hwang, and H. J. Sung. Influence of low- and high-speed structures on the quiescent core region in a turbulent pipe flow. Proceedings of the Tenth International Symposium on Turbulent and Shear Flow Phenomena, 2017. URL "http://tsfp10.org/TSFP10_program/2/330.pdf".

M. Yoon, J. Hwang, J. Lee, H. J. Sung, and J. Kim. Large-scale motions in a turbulent channel flow with the slip boundary condition. *International Journal of Heat and Fluid Flow*, 61:96–107, 2016.

N. Zhen, R. A. Handler, Q. Zhang, and C. Oeth. Evolution of a hairpin vortex in a shear-thinning fluid governed by a power-law model. *Physics of Fluids*, 25: 101703, 2013.

J. Zhou, R. J. Adrian, S. Balachandar, and T. M. Kendall. Mechanisms for generating coherent packets of hairpin vortices in channel flow. *Journal of Fluid Mechanics*, 387:353–396, 1999.